

**Hard and Tough Electrodeposited Aluminum-Manganese Alloys  
with Tailored Nanostructures**

by

Shiyun Ruan

S.B., Materials Science and Engineering (2005)  
S.B., Mechanical Engineering (2005)

University of California, Berkeley

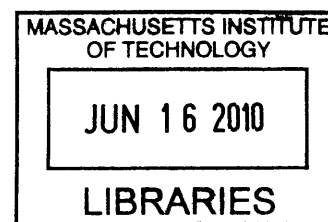
Submitted to the Department of Materials Science and Engineering  
in Partial Fulfillment of the Requirements for the Degree of  
Doctor of Philosophy in Materials Science and Engineering

at the

Massachusetts Institute of Technology

June 2010

**ARCHIVES**



© 2010 Massachusetts Institute of Technology  
All rights reserved

Signature of Author .....

Department of Materials Science and Engineering  
May 18, 2010

Certified by .....

Christopher Schuh  
Danae and Vasilios Salapatras Associate Professor of Metallurgy  
Thesis Supervisor

Accepted by .....

Christine Ortiz  
Chair, Departmental Committee on Graduate Students

# **Hard and Tough Electrodeposited Aluminum-Manganese Alloys with Tailored Nanostructures**

by

Shiyun Ruan

Submitted to the Department of Materials Science and Engineering on  
May 18, 2010 in Partial Fulfillment of the Requirements for the Degree of  
Doctor of Philosophy in Materials Science and Engineering

## **Abstract**

Tailoring the nanostructure of electrodeposited Al-Mn films to achieve high hardness and toughness is the overarching goal of this thesis. Binary Al-Mn alloys are electrodeposited using a conventional current waveform in a chloroaluminate electrolyte at ambient temperature. It is found that alloys with low Mn contents comprise micrometer-sized FCC grains. At intermediate Mn contents, the FCC grain size decreases abruptly to the nanometer regime upon the appearance of a secondary amorphous phase. In these dual-phase alloys, the phases are distributed in a characteristic domain-network structure. At high Mn contents, an amorphous phase that contains pre-existing nanoquasicrystalline nuclei dominates. Leveraging the effects of surface kinetics at the electrode on the alloy microstructure, a reverse-pulse current waveform is designed to tailor the grain size and phase distribution of the electrodeposits; single phase FCC alloys with nanocrystalline grains, as well as dual-phase alloys with homogeneous phase distribution are synthesized. Solute distributions in these alloys are investigated using atom probe tomography. Implanted Ga ions are used as chemical markers for the amorphous phase; this method permits more robust phase identification and measurement of their compositions. Whereas uniform Mn distributions are observed in the single phase alloys, Mn is found to weakly partition into amorphous phase of the dual-phase alloy by ~2 at.%. Micro-indentation of the reverse-pulsed alloys and the guided bend tests reveal high hardness and toughness that are comparable to steels. High hardness is attributed to a combination of solid-solution strengthening effects and structural refinement; high toughness of the nanostructured alloys arises from the activation of both grain boundary- and dislocation-mediated deformation mechanisms; malleability of the amorphous alloys stems from the simultaneous operation of multiple shear bands during deformation. An unprecedented combination of high hardness, toughness and lightweight is thus achieved in our electrodeposited Al-Mn alloys.

Thesis Supervisor: Christopher Schuh

Title: Danae and Vasilios Salapatias Associate Professor of Metallurgy

# Table of Contents

Acknowledgements .....	5
List of Figures .....	6
List of Tables .....	13
1. Introduction.....	15
1.1. Electrodeposition of aluminum alloys .....	17
1.1.1. Selection of alloy system.....	18
1.1.2. Electrodeposition of Al-Mn at elevated temperatures .....	18
1.1.3. Film deposition at low temperatures.....	21
1.2. Pulsed electrodeposition .....	22
1.3. Problem statement .....	24
1.4. Structure of thesis .....	25
2. Electrodeposited Al-Mn alloys with microcrystalline, nanocrystalline, amorphous and nano-quasicrystalline structures.....	26
2.1. Experimental procedures.....	26
2.2. Results.....	30
2.2.1. SEM—Surface Morphology.....	30
2.2.2. XRD—Phase identification and characteristics .....	31
2.2.3. TEM—Phase distribution and structure.....	33
2.2.4. STEM—Phase composition .....	37
2.2.5. DSC--Structure of the amorphous phase.....	39
2.2.6. Nanoindentation—hardness .....	41
2.2.7. Guided bend test—ductility.....	42
2.3. Discussion .....	43
2.3.1. Phase composition .....	44
2.3.2. Amorphous phase character .....	45
2.3.3. Structure-composition relationship.....	47
2.3.4. Hardness of the deposits.....	49
2.3.5. Ductility of nanostructured and amorphous alloys .....	50
2.4. Conclusions .....	50
3. Tailoring the grain size and phase distribution of electrodeposited Al-Mn alloys to achieve high hardness and toughness.....	52
3.1. Experimental procedures.....	53
3.2. Microstructure characterization.....	54
3.2.1. Alloy composition.....	54
3.2.2. Phase content .....	55
3.2.3. Grain size and phase distribution.....	57
3.3. Mechanical properties.....	60
3.3.1. Micro-hardness .....	60
3.3.2. Tensile ductility .....	61
3.3.3. Fractography.....	62
3.3.4. Post-mortem TEM .....	64
3.3.5. Hardness vs. toughness .....	67
3.4. Conclusions .....	68

4. An atom probe investigation of weak solute partitioning in nanocrystalline and amorphous phases of Al-Mn.....	70
4.1. APT studies on nanostructured and amorphous alloys.....	70
4.1. Experimental procedures.....	72
4.2. Composition and structure of the deposits.....	73
4.3. APT analysis of Mn distribution.....	76
4.4. Enhancing APT phase contrast with Ga markers.....	81
4.5. Conclusions.....	90
5. Conclusions.....	92
6. Directions for Further Research.....	94
Appendix A. Kinetic Monte Carlo simulations of nanocrystalline film deposition.....	96
A.1. Introduction.....	96
A.2. Model.....	98
A.2. Steady-state microstructure.....	103
A.3. Surface morphology.....	107
A.4. Bulk nanostructure of the deposits.....	110
A.4.1. Vacancy incorporation.....	111
A.4.2. Grain nucleation mechanism.....	112
A.4.3. Factors controlling grain dimensions.....	115
A.4.4. Vacancy-grain boundary interactions.....	119
A.4.5. Grain size vs. shape.....	120
A.5. Conclusions.....	121
Appendix B. Effects of current pulses on the ductility of electrodeposited Al alloys ....	123
B.1. Effects of pulse current density, $i_2$ .....	123
B.2. Effects of pulse duration, $t_2$ .....	126
B.3. Ternary alloy electrodeposited at non-ambient temperature.....	128
B.4. Conclusions.....	130
References.....	131



## Acknowledgements

I gratefully acknowledge my thesis committee members, Professor Carl V. Thompson and Professor Silvija Gradečak for their time and insightful comments. I would like to thank the senior Schuh group members, including Vee, Megan, Alan, Andy, Ying, Corinne, Jay, Jeremy, David, Koichi, Ken and Oliver for inspiring and motivating me to do good science. I am also thankful to the current group members for the many pleasant interactions. I am especially grateful to Dr. Yong Zhang, Dr. Scott Speakman, Ms. Elisabeth Shaw and Mr. Donald Galler for their patience and help with the TEM, XRD, AES and SEM. All the experiments in this thesis research would not have been possible without the help, support and patience of the ISN staff—Dr. Steven Kooi, Mr. William DiNatale and Mr. Philipp Schmidt-Ullrich.

Even though they are 9,500 miles away, my family and god-family members have been extremely supportive and loving, so thank you! It would be impossible to imagine graduate school without my great friends—Jeremy, Jack, Fan, Michelle, Yoda, Angelina, Amy, Nancy, Karen, Audra, Zan and Erin. Thank you for the great times and for bringing so much cheer into my life.

I would also like to thank my bubbly and lively officemates—Markus, Jon, Sophie and Joy for making it a real pleasure to work during the weekdays and weekends. I am extremely grateful to my closest friends, who have been helping me survive the last and most arduous part of this journey: Steve, who inspires me with his calmness and positive outlook, Bill, for his thoughtfulness and daily dose of craziness and laughter, Donna, whose sensitivity, generosity and homemade lunches remain unrivaled, Michelle, whose kindness and understanding deeply touch my heart, Yoda, who has been standing by me through the many ups and downs of graduate school, Nancy, the best roommate I have ever had, Angelina, for being very thoughtful, sensitive and wise, and Jeremy, who has always been there for me since Day One of our friendship.

Finally, I would like to thank my advisor, Professor Christopher A. Schuh for his infinite (not a typo!) patience and guidance. Not only has he taught me how to approach seemingly ridiculous science problems and inspired me with his intelligence and competence, but he has also encouraged me to dream big, guided me to find my career path and taught me a lot about life—when life hands you lemons, make lemonade.

## List of Figures

- Figure 1.1: Ashby plot showing hardness vs. tensile elongation at fracture of nanocrystalline, amorphous and commercial Al alloys, as well as structural steels [1-4].
- Figure 1.2: A schematic summarizing the different phases that have been electrodeposited at different temperatures as a function of Mn content in prior studies [69].
- Figure 1.3: Microstructures of films deposited at different temperatures at a fixed deposition rate [85]. Only the top 1000 layers are shown.
- Figure 1.4: Schematic of four types of electrodeposition current waveforms, where cathodic current is defined as positive. Waveform (a) illustrates constant current density. Waveforms (b)-(d) contain many cycles. Each cycle, in turn, comprises pulses; and each pulse has its defined pulse duration, e.g.  $t_1$ , and pulse current density, e.g.  $i_1$ . In this illustration, each waveform contains only one unique cycle that repeats itself. Waveform (b) is characterized by a cycle that contains two cathodic pulses. The cycle in waveform (c) contains one cathodic pulse and one “off-time” pulse. The cycle in waveform (d) contains one cathodic pulse, and one anodic pulse.
- Figure 2.1: SEM images of as-deposited Al-Mn alloys with global Mn content as shown in the lower-left corner of each panel. Note the transition from faceted features in images (a)-(d) to rounded nodules in images (e)-(h).
- Figure 2.2: X-ray diffractograms of as-deposited Al-Mn alloys, the compositions of which are shown at the right. Locations of the FCC Al(Mn) reflections are shown at the top. Note also the emergence of a broad amorphous halo at  $\sim 42^\circ 2\theta$  for compositions above 8.2 at%.
- Figure 2.3: Lattice parameter of the FCC phase, as calculated from peak positions in the X-ray diffractograms of Figure 2.2. Also shown for comparison are data obtained for Al-Mn alloys electrodeposited at 150 °C by Grushko and Stafford in ref. [61], and for melt-spun alloys by Schaefer et al in ref. [109].
- Figure 2.4: Bright-field TEM images and electron diffraction patterns of as-deposited alloys with global Mn content as shown in the lower-left corner of each panel. Note the transition from micron-size grains in image (a) to nanocrystalline grains in images (b)-(e). Note also that images (b)-(e) show  $\sim 20$ -50 nm convex domains surrounded by a matrix or network structure.

- Figure 2.5: Electron diffraction patterns of two-phase alloys with global Mn content labeled in each panel. Peak positions of the sharp reflections are indexed to be consistent with FCC Al(Mn), as shown in panel (a). Note that the relative intensity of the broad halo, whose peak position is located between the (111) and (200) reflections, increases as the global Mn content increases.
- Figure 2.6: HRTEM image of an 8.2 at.% Mn alloy, showing the “matrix” or “network” region between two large grains that are labeled ‘A’. This region comprises small ~4 nm crystallites (some of which are circled and labeled ‘B’) embedded in an amorphous-like field (labeled ‘C’).
- Figure 2.7: HRTEM images of a 9.2 at.% Mn alloy, showing domains and the surrounding network structure in (a), where the domains are outlined in bold and labeled ‘D’, and appear featureless. A higher magnification image of the surrounding network region, taken from the region denoted by dotted lines in (a), is shown in (b). The network region comprises mainly small crystallites (labeled ‘E’).
- Figure 2.8: STEM results comparing local compositions of domain and network regions of the two-phase alloys, along with a dashed line showing the expected composition for a homogeneous alloy. The amorphous phase is located in the network regions for the 8.2 at.% Mn alloy, but in the domain regions for alloys with higher Mn contents. Thus, Mn preferentially partitions to the amorphous phase for all these alloys.
- Figure 2.9: (a) A Scanning-mode DSC trace showing the two exothermic peaks observed when a 15.8 at.% Mn alloy was heated from 30 °C to 520 °C at 10 °C/min. Using the dotted lines as baselines, the enthalpies of the two transformation events were 900 J/mol and 2770 J/mol respectively. (b) The isothermal DSC output for a 15.8 at.% Mn alloy annealed at 310 °C for 55 minutes; the total heat evolved was 840 J/mol.
- Figure 2.10: X-ray diffractograms of 15.8 at.% Mn samples (a) in the as-deposited state, (b) after isothermal treatment at 310°C for 55 minutes and (c) after being heated from 30 °C to 520°C at 10 °C/min. For comparison, the top panel shows peak positions and relative intensities of icosahedral Al<sub>6</sub>Mn produced by rapid quenching in ref. [111], while the second panel shows those for orthorhombic Al<sub>6</sub>Mn in ref. [112].
- Figure 2.11: HRTEM image and electron diffraction pattern of a 15.8 at.% Mn alloy after isothermal annealing at 310°C for 55 minutes. As compared to the as-deposited condition, which was apparently amorphous (Figure 2.4(f)), this specimen exhibits small regions with clear lattice fringes. Some of the crystallites are outlined in bold; the average grain size is about 2 nm.

- Figure 2.12: Electron diffraction patterns of 15.8 at.% Mn alloys (a) in the as-deposited state and (b) after isothermal annealing at 310 °C for 55 minutes. Note the appearance of additional reflections in (b), which are indexed as consistent with the icosahedral phase. The arrows indicate the positions of the rings in each panel.
- Figure 2.13: (a) Plot summarizing the grain/crystal size measurements of the FCC solid solution phase as determined by various techniques. Phase compositions of the alloys are labeled at the top of the panel. (b) Plot of hardness vs. alloy composition; notice that the dramatic decrease in grain size at ~8.2 at.% Mn is accompanied by an increase in hardness by about a factor of 2.
- Figure 2.14: SEM images of the convex bent surfaces of the 8.2 at.%-Mn and 13.6 at.%-Mn alloys upon application of ~5% tensile strain are shown in (a)-(b) and (c)-(d), respectively. The relatively straight crack paths are characteristic of brittle fracture.
- Figure 3.1: Plot showing the effects of current waveform on alloy composition at different electrolyte compositions.
- Figure 3.2: X-ray diffractograms of as-deposited RP Al-Mn alloys, the compositions of which are shown at the right. Locations of the FCC Al(Mn) reflections are shown at the top. Note also the emergence of a broad amorphous halo at  $\sim 42^\circ 2\theta$  for compositions above 8.0 at%.
- Figure 3.3: Percent contribution of FCC peaks to the total integrated intensities observed in X-ray diffractograms, as shown in Figure 2.2 for the DC alloys and Figure 3.2 for the RP alloys.
- Figure 3.4: Bright-field TEM images and electron diffraction patterns of the RP alloys. Note the single phase nanocrystalline structures in (c)-(d). Images (e)-(g) shows that the two-phase alloys no longer comprise the domain-network structures observed in the DC alloys in Figure 2.4.
- Figure 3.5: (a) Average grain sizes of DC and RP alloys at different Mn compositions. Region shaded gray represents the composition range within which both the RP and DC alloys contain a single FCC phase. The grain size distribution of ~250 grains observed in the 8.2 at.%-Mn alloys are shown in (b) for the DC alloy and (c) for the RP alloy. Also shown in (c) is a lognormal distribution curve.
- Figure 3.6: SEM images of the entire bent surfaces of films that were subject to ~37% tensile strain are shown on the left column. Corresponding higher magnification images of the bent regions are presented on the right.

- Figure 3.7: SEM images of the fracture surfaces of films containing (a)-(b) 7.8, (c)-(d) 8.2 and (e)-(f) 13.8 at.-%-Mn. In images (a)-(d), the solid black lines demarcate the Al-Mn film and its copper substrate and the double-headed arrows are used to roughly approximate the film thickness in the trailing regions of the fracture.
- Figure 3.8: TEM image in (a) belongs to a region far from the bend; image (b) corresponds to a bent region where the applied tensile strain is ~37%. The corresponding grain size distributions are shown in (c) and (d), along with the lognormal distribution curves. The cumulative grain size distribution plots of both regions are illustrated in (e).
- Figure 3.9: TEM images of a 8.2 at.-%-Mn sample; image (a) belongs to a region far from the bend; image (b) corresponds to a bent region where the applied tensile strain is ~13%.
- Figure 3.10: Ashby plot showing (a) hardness and (b) specific hardness vs. tensile elongation at fracture of our electrodeposited Al-Mn alloys. Samples that did not exhibit any crack after the guided bend test are represented by solid red hexagons. The solid black arrows pointing to the right of these hexagons indicate that the ductility of these samples exceeds the values represented by the data points. Samples that failed, i.e. exhibited fissures or cracks of any length and width, are denoted by pentagons outlined in red. Also shown in this plot are the properties of commercial Al-based alloys, as well as structural steels.
- Figure 4.1: XRD patterns of the electrodeposited Al-Mn alloys are shown on the left column. The corresponding bright-field TEM images and electron diffraction patterns are shown on the right. The four rows respectively correspond to samples 1, 2, 3, and 4, from Table 4.1. Notice the transition from a single FCC phase to an amorphous phase as Mn content increases.
- Figure 4.2: Perspective views of a few representative APT specimens are shown on the left column with corresponding two-dimensional atom dot maps in the x-y plane on the right. These images are obtained from (a)-(b) sample 1A, (c)-(d) sample 2C and (e)-(f) sample 3E (see Table 4.1). The yellow dots represent Al atoms and the blue dots denote Mn atoms.
- Figure 4.3: Typical one-dimensional composition profiles of Mn in the APT specimens. The sampling volume was divided into 1.5 x 1.5 x 1.5 nm blocks to compute the local solute content. The thin horizontal line represents the average solute content; the thin dashed lines represent values that are two standard deviations away from the average composition. In all four samples, Mn distribution appears uniform.

- Figure 4.4: Autocorrelation functions of Mn content along the long axis of each sample, plotted as a function of wavelength,  $k$ . The sampling volume was divided into  $1.5 \times 1.5 \times 1.5$  nm blocks to compute the local solute content. The thick solid lines represent experimental results, whereas the thin dashed lines denote results obtained for compositionally randomized structures with the same atomic positions.
- Figure 4.5: Composition distributions of Mn based on binning the APT data into blocks containing 100 Al and Mn atoms. Experimental results are denoted by solid circles and the binomial distributions are represented by dashed lines. The coefficients of determination,  $R^2$ , are (a) 0.985, (b) 0.977, (c) 0.992 and (d) 0.992. Notice that in (b), there is a slight discrepancy between the experimental result and binomial curve, especially between 8 and 11 at.%-Mn (highlighted by an arrow).
- Figure 4.6: Perspective views of a few typical APT specimens are shown on the left column and the corresponding two-dimensional atom dot maps are shown on the right. These images are obtained from the same samples as those shown in Figure 4.2, i.e. (a)-(b) sample 1A, (c)-(d) sample 2C and (e)-(f) sample 3E. In addition to the Al (yellow dots) and Mn (blue dots) atoms already shown in Figure 4.2, the dot maps presented here also show the Ga atoms (red dots). Figures 4.6(c)-(d) show a strongly-partitioned Ga distribution.
- Figure 4.7: (a) Two-dimensional atom dot map of sample 2D, showing Ga atoms (red) preferentially occupying patches that surround domains that are relatively Ga-free; these domains are between  $\sim 15$  and  $\sim 40$  nm in diameter. Such a non-uniform Ga distribution is similar to that observed in Figure 4.6(d) for sample 2C. For these 9.2 at.%-Mn samples, a typical composition profile of Ga is shown in (b) and the autocorrelation function is shown in (c) with  $k$  the wavelength. The plots in (b) and (c) indicate strong Ga segregation at a wavelength of  $\sim 20$  nm.
- Figure 4.8: Composition distribution of Mn in the 9.2 at.% Mn sample; the experimental data are the same as those shown in Figure 4.5(b), as is the expected binomial distribution curve (dashed line). The two-phase binomial-binomial fit is represented by the thick solid line and its individual components are represented by thin solid lines. The coefficient of determination,  $R^2$ , of the binomial-binomial fit is 0.999, much higher than that of the single binomial (0.977).
- Figure 4.9: Composition profile of (a) Ga and (b) Mn along the long axis of the 9.2 at.%-Mn specimen (sample 2C). Regions containing Ga are shaded gray. Note that in these regions, the local Mn contents are  $>2$  at.% above the average composition (represented by the upper dashed line).

- Figure A.1: A schematic diagram of the close-packed lattice and coordinate system used to simulate film growth. Deposition occurs in  $-y$  direction. Light grey atoms belong to the process zone; dark grey atoms belong to the bulk. Atoms in the lowest columns are outlined in bold. The atom labeled ' $g_1$ ' is allowed to hop in directions indicated by solid arrows; dashed arrows represent forbidden hops. Atom ' $g_1$ ' can also switch its grain number to  $g_2$  or  $g_3$ . Interlayer transport of atom  $g_4$  occurs if it carries out two successive jumps, as indicated by the solid arrows. The first jump results in a net loss of one bond and brings the atom to an activated state.
- Figure A.2: Time evolution of (a) surface step height, (b) surface peak spacing and (c) vacancy content of films deposited at a rate of 0.252 when diffusion is restricted to the process zone. Average dimensions of the grains found in each layer of these films are shown in (d) and (e). Cumulative grain size distribution plots are shown in (f), where the dashed lines represent results obtained when bulk diffusion is permitted.
- Figure A.3: Microstructures of deposited films with fixed grain boundary energy of 0.48. Images (a)-(c) show films deposited at different temperatures at a fixed deposition rate of 0.252. Images (d)-(e) illustrate films grown at different deposition rates at a constant temperature of 0.65. Only the top 1000 layers are shown.
- Figure A.4: Microstructures of films with different grain boundary energies; these films are deposited at a temperature of 0.43 and deposition rate of 0.025. Only the top 1000 layers are shown.
- Figure A.5: Steady-state step height vs. deposition rate of films deposited at different temperatures and grain boundary energies.
- Figure A.6: Steady state step height vs. effective Schwoebel-type step edge barrier of films deposited at different temperatures. Also shown are data obtained from ref. [208].
- Figure A.7: Steady-state peak spacing vs. deposition rate of films deposited at different temperatures and grain boundary energies.
- Figure A.8: Steady state vacancy density vs. deposition rate of films deposited at different temperatures and grain boundary energies.
- Figure A.9: Snapshots of the film growth process at  $T^* = 0.43$ ,  $D_b^* = 0.051$  and  $E_{gb}^* = 0.48$ ; these images are taken at a time interval of 10 ML. Notice that grains nucleate preferentially on surface peaks (see solid blue ellipses in (a)-(f) and red ellipses in (c)-(e)). Grain growth in lateral direction appears limited by peak spacing (see red ellipses in (e)-(h)). Regions

enclosed in blue boxes in (a)-(h) illustrate grain boundary migration until the grain boundaries are pinned by voids.

Figure A.10: Snapshots of the film growth process at  $T^* = 0.78$ ,  $D_b^* = 0.126$  and  $E_{gb}^* = 0.48$ ; these images are taken at a time interval of 10 ML. The solid red ellipse in (b) shows a nucleus that eventually grows into a grain; this nucleus forms a triple point with nearby grains in (d). The dashed blue ellipse in (b) shows a nucleus that is eventually eliminated in (f). Regions enclosed in blue boxes in (g)-(h) illustrate grain boundary migration until the grain boundaries are pinned by voids.

Figure A.11: Average (a) grain minor and (b) grain major vs. deposition rate of films deposited at different temperatures and grain boundary energies.

Figure A.12: Relationship between peak spacing and grain minor of films deposited under various conditions. The dashed line represents a 1:1 relationship.

Figure A.13: Relationship between grain major and normalized switch rate of films deposited under various conditions.

Figure A.14: Relationship between grain aspect ratio and grain diameter of films deposited under various conditions.

Figure B.1: SEM images of bent surfaces of ~8 at.% Mn alloys produced by different waveforms. Images on the left column correspond to samples that were strained to ~37%. Images on the right correspond to samples that were bent strained to ~13% true strain.  $i_2$  decreases from +6 mA/cm<sup>2</sup> to -3.75 mA/cm<sup>2</sup> from the topmost to bottommost row.

Figure B.2: SEM images of bent surfaces of ~8 at.% Mn alloys produced by waveforms with different  $t_2$ . Images (a)-(d) correspond to samples that were strained to ~37%. Images (e)-(h) correspond to samples that were subject to a tensile strain of ~13%. The pulse duration  $t_2$  increases from 0 to 20 ms from the topmost to bottommost row.

Figure B.3: SEM images of bent surfaces of Al-Mn-Ti alloys produced by different waveforms. Samples were strained to ~37% in images (a)-(b); and ~8% in images (c)-(d).



## List of Tables

- Table 2.1: Summary of the various electrolytic compositions used in this study, and the deposits produced with them. The global Mn content is measured by EDX and is reported with error bars; the size of surface features is measured from SEM images; the area % of FCC peaks is calculated from the X-ray diffractograms; average grain size is reported from both XRD and TEM measurements; the extent of Mn enrichment in the amorphous phase, as determined by STEM, is reported according to the formula of Eq. (2-2).
- Table 3.1: Solute contents of the three RP alloys selected for mechanical testing are listed on the top row. Also shown are the phase composition, FCC grain size, micro-hardness and tensile elongation at fracture of each alloy.
- Table 4.1: A summary of the total number of atoms collected for each APT specimen, along with its APT and SEM/EDX alloy composition. Also shown are the grain sizes determined from XRD and TEM analysis.
- Table 4.2: Contingency table for blocks of atoms containing 100 Al atoms in the 9.2 at.%-Mn specimen. The chi-squared statistic for experimental deviation from randomness is 2259 and the corresponding value at the 0.001% significance level is 28.
- Table 4.3: Contingency table for blocks of atoms containing 100 Al atoms in the 10.2 at.%-Mn specimen. The chi-squared statistic for experimental deviation from randomness is 33 and the corresponding value at the 0.001% significance level is 28.
- Table 4.4: Contingency table for blocks of atoms containing 100 Al atoms in the 16.0 at.%-Mn specimen. The chi-squared statistic for experimental deviation from randomness is 26 and the corresponding value at the 0.001% significance level is 23.
- Table B.1: Pulse parameters of waveforms used to investigate the effects of  $i_2$ .
- Table B.2: Dimensions of cracks observed on strained surfaces of alloys containing ~8 at.% Mn after guided bend test, where applied tensile strains are ~37% and ~13%.
- Table B.3: Pulse parameters of waveforms used to investigate the effects of  $t_2$ .
- Table B.4: Dimensions of cracks observed on strained surfaces of alloys containing ~8 at.% Mn after guided bend test, where applied tensile strains are ~37% and ~13%.

- Table B.5: Composition of electrolytic bath used to electrodeposit Al-Mn-Ti alloys.
- Table B.6: Pulse parameters of waveforms used to electrodeposit Al-Mn-Ti alloys.
- Table B.7: Dimensions of cracks observed on strained surfaces of Al-Mn-Ti alloys containing ~8 at.% solute after guided bend test, where applied tensile strains are ~37% and ~8%.

# 1. Introduction

Lightweight alloys with high hardness and toughness are potentially valuable in structural, aerospace and flexible armor applications, due to their high strength-to-weight ratio and ability to dissipate impact energy by plastic deformation. While most commercial Al alloys exhibit high ductility, as shown in Figure 1.1, their hardness do not suffice for most structural applications, where a minimum hardness of 3 GPa is usually required. This thesis research seeks to tailor the microstructure of lightweight Al to achieve high hardness and toughness that are comparable to those of structural steels (also shown in Figure 1.1).

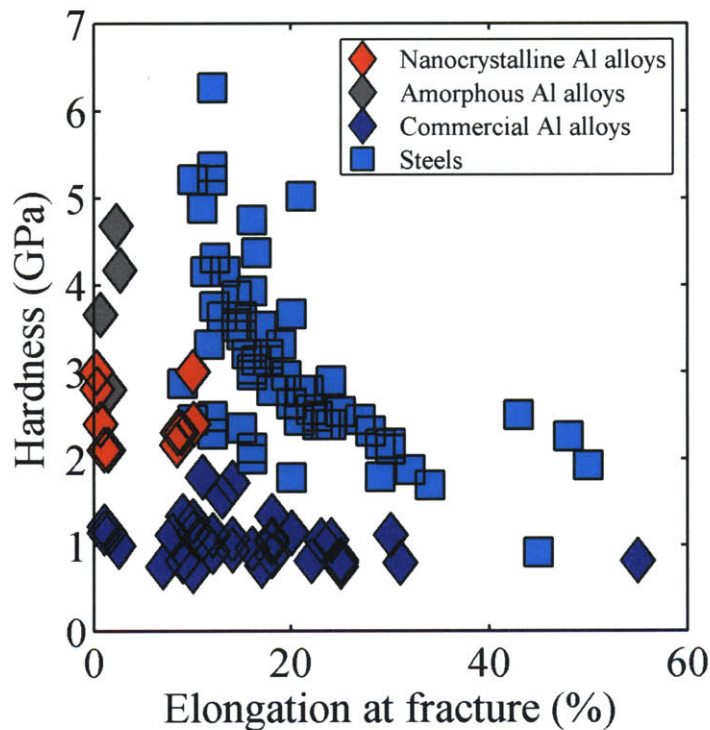


**Figure 1.1** Ashby plot showing hardness vs. tensile elongation at fracture of nanocrystalline, amorphous and commercial Al alloys, as well as structural steels [1-4].

Efforts to improve the hardness of Al alloys commonly involve structural refinement down to the nanocrystalline and amorphous regimes [1-3]. As illustrated in Figure 1.1, an improvement in hardness often occurs at the expense of ductility for most nanocrystalline and amorphous alloys. Low ductility in these alloys can be attributed to the absence of dislocation activity and rapid shear band propagation leading to catastrophic failure. However, some nanocrystalline alloys are capable of plastic

deformation up to ~10 % (Figure 1.1), likely because of low artifact and vacancy contents [2], as well as grain sizes that are above ~10 nm, which allow dislocation- and grain boundary-mediated deformation mechanisms to operate simultaneously [5-8]. These results point to the importance of synthesizing artifact-free and fully-dense nanocrystalline alloys with tailorable grain sizes.

Because the large volume fraction of high energy interfaces results in a huge thermodynamic driving force for grain coarsening, it is often challenging to synthesize nanostructured materials. A feasible approach that has proven successful in producing nanometer grain sizes involves adding secondary alloying elements [9-16]. Broadly, alloying elements facilitates nanostructure formation either by segregating to the grain boundaries to thermodynamically stabilize these high energy interfaces [17-20], or by forming competing secondary phases, which kinetically restrict structural coarsening [21-25]. In addition to its role in nanostructure formation and/or stabilization, alloying also introduces a multitude of avenues for tuning the properties of nanostructured materials. Whereas properties of pure nanocrystalline metals are primarily dictated by grain size, those of single phase alloys are also affected by chemical composition, solute distribution and chemical ordering [33, 35-58]. Properties of multi-phase alloys are additionally governed by phase composition, phase fraction and phase distribution [26-35]. Thus, alloying not only promotes nanostructure formation, but it also creates a broad range of microstructural features; these additional variables offer more opportunities to tailor the properties of nanostructured materials.

Due to their non-equilibrium states, details of the abovementioned microstructural features also hinge on the processing science pertinent to the synthesis technique employed. Techniques that have been developed to synthesize nanostructured alloys include mechanical milling [36-39], gas phase synthesis [36, 40], chemical and physical vapor deposition [36, 41], magnetron sputtering [36, 42] and electrochemical deposition [9, 36, 43-49]. Of these processing methods, electrochemical deposition (herein referred to as electrodeposition) has proven particularly attractive because each of the easily-adjustable processing variables, such as electrolytic bath composition, temperature, and applied current or voltage waveform, often affects some microstructural facet of the electrodeposit. Recent works have also demonstrated processing advances that permit a

fine level of control over the electrodeposited nanocrystalline grain size [9, 44, 50]. Besides offering more exact microstructural control, electrodeposition is also a readily scalable technique and can be used with substrates of virtually any shape. Thus, it has proven particularly important as a technology for creating nanostructured metal and alloy coatings as well as free-standing electroforms, with exceptional physical properties [46-48, 51] and good thermal stability [52, 53].

In addition to the abovementioned advantages, electrodeposition also allows a wide range of metals and alloys to be fabricated upon the judicious selection of an appropriate electrolyte. Many alloy systems, including copper-, iron- and nickel-based alloys, can be electrodeposited in aqueous electrolytes [9, 36, 43-49]. Metals which exhibit lower reduction potentials than water, such as titanium, magnesium and aluminum, can be electrodeposited in non-aqueous electrolytes, such as molten salts. In part because of the processing challenges involved, such as high temperature requirements and the corrosive effects of molten salts, efforts to tailor the microstructure and properties of electrodeposited titanium, magnesium and aluminum alloys have been relatively scarce. Fortunately, recent progress in the development of less hazardous ionic liquids has opened up the possibilities to electrodeposit these lightweight metals and alloys at reasonable processing temperatures that are below  $\sim 200^{\circ}\text{C}$  [54-59].

In this thesis, the concept of nanostructure formation and/or stabilization by alloying is employed to synthesize nanostructured lightweight aluminum alloys with high hardness and respectable toughness by electrodeposition. Experimental works span the processing, characterization, as well as property measurements of electrodeposited aluminum alloys. In the following sections, the relevant literature on (a) electrodeposition of aluminum and (b) the use of electrodeposition current pulses to tune alloy microstructure are reviewed to provide background for the thesis research that follows.

### ***1.1. Electrodeposition of aluminum alloys***

With an eye to electrodeposit aluminum alloys that exhibit a wide range of nanostructures, this section reviews previous works that have been performed to synthesize pure nanocrystalline aluminum, identifies suitable alloying elements and

presents a comprehensive summary of prior results that have been obtained for the selected system.

### ***1.1.1. Selection of alloy system***

Electrodeposition of nanocrystalline Al has been achieved by other researchers using additives, such as nicotinic acid and benzoic acid to chloroaluminate ionic liquid electrolytes [57, 59]. While additives effectively refine grain size, the range of grain sizes that can be obtained is limited; for instance, very small amount of benzoic acid (0.02 mol/L) reduces the Al grain size from >100 nm to 20 nm and further increase in benzoic acid concentration does not cause further reduction in grain size [59]. The narrow range of grain size, coupled to the limitations in tuning the properties of pure metals (as described in the previous section), points to a need to introduce a secondary element.

Possible solute elements that can be co-deposited with Al include manganese, titanium and nickel [60-65]. Of these, manganese (Mn) was selected because the binary Al-Mn system exhibits a rich variety of equilibrium phases, including solid solutions and at least nine intermetallic phases, thus suggesting the possibility of nanostructure formation and stabilization via secondary phase formation. Additionally, because the ratio of the atomic radius of Mn to that of Al is close to that which is ideal for icosahedral packing (0.923 and 0.905, respectively), Mn additions have been found to frustrate FCC packing in Al, thus resulting in icosahedral phase formation [66-68]. That Mn promotes disorder hints of possible structural refinement down to the amorphous limit under non-equilibrium processing conditions. A review of prior works on electrodeposition of Al-Mn at elevated temperatures is discussed in what follows.

### ***1.1.2. Electrodeposition of Al-Mn at elevated temperatures***

A rich variety of equilibrium and metastable phases that the Al-Mn system exhibits can be produced by a single technique, i.e., electrodeposition from acidic chloroaluminate salts [61, 62, 64, 69-78]. Figure 1.2 summarizes the different phases that have been electrodeposited at different temperatures as a function of Mn content in prior studies [69]. While phases predicted by the equilibrium phase diagram have been

electrodeposited in the temperature range of 250 to 425°C [73, 74], non-equilibrium phases, such as the quasicrystalline phases, amorphous phase, and supersaturated FCC phase, have been deposited at lower temperatures from 150 to 325°C [61, 64, 71, 73, 75-77].

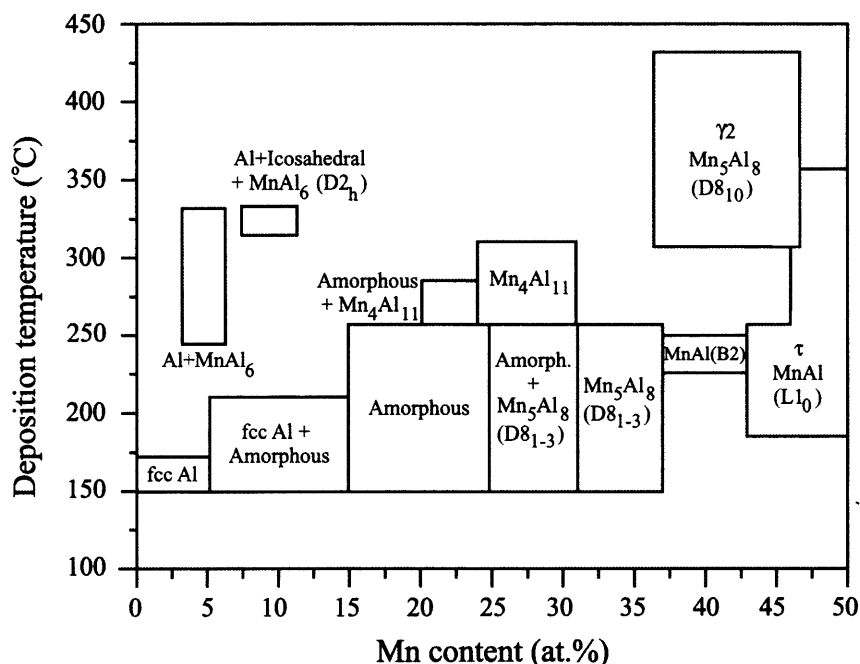


**Figure 1.2** A schematic summarizing the different phases that have been electrodeposited at different temperatures as a function of Mn content in prior studies [69].

Despite the significant number of works conducted on electrodeposited Al-Mn alloys [61, 62, 64, 70-79], only a few studies have provided detailed characterization of the deposited structure. In 1966, Read and Shores presented transmission electron diffraction patterns of Al-Mn alloys electrodeposited from a chloroaluminate molten salt electrolyte (AlCl<sub>3</sub>-KCl-NaCl-MnCl<sub>2</sub>) presumably at 200° C [76]. Their data suggested that for alloys with low Mn content below about 6 at.%, a single FCC phase was deposited, with higher Mn content promoting apparently finer grains. At somewhat higher Mn contents up to about 12 at.%, a second phase coexisted with the FCC phase, as evidenced by an additional diffuse reflection between the first and second rings in the electron diffraction patterns. The authors identified the second phase as the intermetallic compound Al<sub>6</sub>Mn. However, because no transmission electron microscope (TEM) images were provided, the grain size and structure, as well as phase distribution of these Al-Mn alloys were not discussed.

Later, Grushko and Stafford carried out structural studies on Al-Mn alloys electrodeposited from  $\text{AlCl}_3\text{-NaCl-MnCl}_2$  molten salt at 150 °C [61, 70]. Their x-ray diffraction (XRD) results suggested that, similar to the results of Read and Shores, intermediate Mn levels between 6 and 15 at.% led to a second phase coexisting with the FCC Al(Mn) solid solution. However, unlike Read and Shores, Grushko and Stafford identified the second phase as amorphous, due to the broad diffraction halo it exhibited. In these two-phase alloys, increasing the Mn content also caused some broadening of the dominant XRD peaks for the FCC phase, which might suggest a gradual size reduction of the FCC crystals (although no quantitative grain size measurements were made). Some bright-field TEM images of the duplex structures were presented, but without local area diffraction or dark-field images to identify the phases present.

Takayama and co-workers investigated the local structure and concentration of the two-phase Al-Mn alloys electrodeposited from eutectic molten salts of  $\text{AlCl}_3\text{-NaCl-KCl-MnCl}_2$  at 200 °C [77]. Micro-area elemental analysis on deposits containing 5.8, 8.8 and 14.9 at.% Mn provided direct evidence that the amorphous phase was enriched with Mn relative to the crystalline phase. Using high resolution TEM (HRTEM) and electron microbeam diffraction, the authors implied that there was actually one crystalline phase with two distinct morphologies coexisting with the amorphous phase, but the micrographs presented did not clarify the two proposed morphologies. Furthermore, while the micro-area images showed that the local structures of the 5.8, 8.8 and 14.9 at.% Mn alloys were somewhat different, the trends were unclear and only qualitative because of the limited fields of view.

Although the above studies provide some hints about the structural changes that occur as the Mn content rises in Al-Mn electrodeposits, many details are clearly missing for a complete understanding of the duplex structures; the crystal morphology and size remains unclear, as does the spatial distribution of the crystalline and amorphous phases. What is more, the nature of the amorphous phase remains ambiguous as well, especially in light of other studies that hint of possible relationships between the amorphous and quasicrystalline phases: First, Grushko and Stafford found that the amorphous phase deposited at 150 °C transformed into the quasicrystalline phase upon annealing [73]. In a



separate study, Grushko and Stafford directly electrodeposited the quasicrystalline phase, instead of the amorphous phase, at a higher deposition temperature of 325 °C [71].

Thus, although Grushko et al. [61, 70] and Takayama et al. [77] have identified an “amorphous” second phase in Al-Mn deposits owing to its broad diffraction halo, this could also correspond to an extremely fine ensemble of quasicrystalline domains [80]. Such “micro-quasicrystalline” (or, more aptly, “nano-quasicrystalline”) structures have been observed in Al-Mn alloys produced by techniques other than electrodeposition, and are indeed characterized by a broad, amorphous-like diffraction halo at the primary reflection. For example, Bendersky and Ridder used HRTEM and diffraction to suggest that rapidly-quenched Al-14 at.% Mn “amorphous” droplets might in fact contain nano-quasicrystalline domains smaller than 2-3 nm [81]. Chen and co-workers used a combination of HRTEM and differential scanning calorimetry (DSC) to establish that “amorphous” Al-17 at.% Mn produced by sputtering had a nano-quasicrystalline structure [82-84]. These findings are decidedly relevant for interpretation of the structures formed in electrodeposited Al-Mn alloys where an “amorphous” phase has been frequently observed, and call for renewed study of such electrodeposits.

### ***1.1.3. Film deposition at low temperatures***

The recent development of ionic liquid electrolytes has enabled room temperature electrodeposition of Al. However, the processing, structure and mechanical properties of Al-Mn alloys electrodeposited at ambient temperature have not been explored, to our knowledge. Recently, a kinetic Monte Carlo model of nanocrystalline film deposition has been developed to study the effects of processing conditions, such as temperature and deposition rate, on film microstructure. This study is described in detail in Appendix A and has been published in [85]. Low temperature is found to increase nano-scale roughness and stabilize surface grain nuclei, thus promoting structural refinement, as illustrated in Figures 1.3(a)-(c), where a fixed deposition rate was employed to simulate film deposition at three different normalized temperatures. In these figures, atoms that belong to the same grain share the same color and trapped vacancies are colored black. That the average grain size decreases as temperature decreases indicates the potential of

electrodepositing nanostructured Al-Mn alloys at room temperature and further stimulate such low temperature experiments.

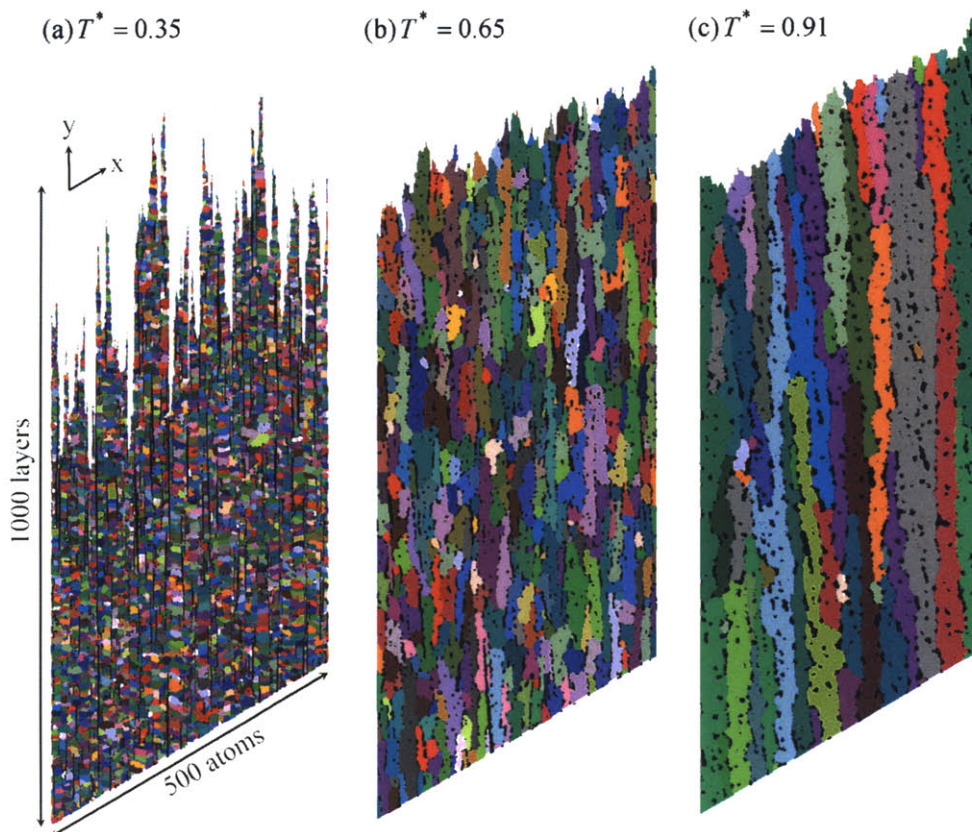
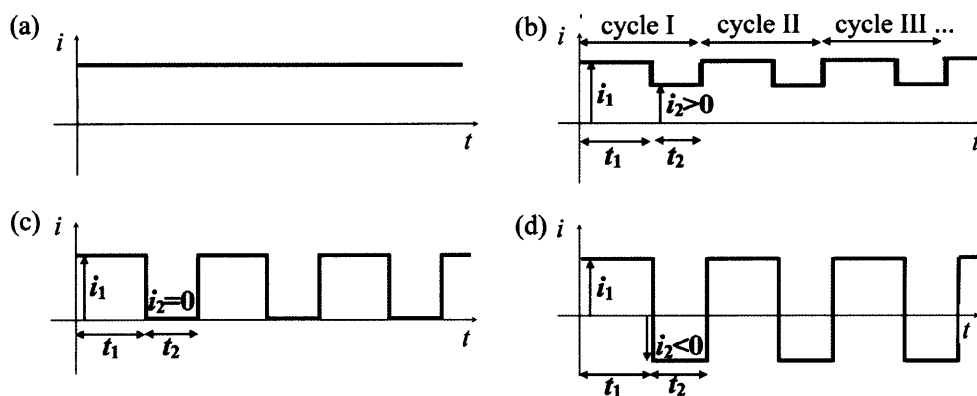


Figure 1.3 Microstructures of films deposited at different temperatures at a fixed deposition rate [85]. Only the top 1000 layers are shown.

## 1.2. Pulsed electrodeposition

In the studies described in section 1.1.2, electrodeposition was carried out under conventional galvanostatic conditions, where the power supply applies a constant current across the electrodes throughout the duration of the electrodeposition process, as shown in Figure 1.4(a). With advances in technology, power supplies can now apply pulsed current waveforms, such as those shown in Figure 1.4(b)-(d). This section provides background information on pulsed electrodeposition and reviews its effects on alloy microstructure.



**Figure 1.4** Schematic of four types of electrodeposition current waveforms, where cathodic current is defined as positive. Waveform (a) illustrates constant current density; waveform (b) contains two cathodic pulses; waveform (c) contains one cathodic pulse and one “off-time” pulse and waveform (d) contains one cathodic pulse, and one anodic pulse.

Each of the current waveforms illustrated in Figure 1.4(b)-(d) comprises cycles. Each cycle can, in turn, contain segments or pulses; and each pulse has a defined pulse current density (e.g. “ $i_1$ ”) and pulse duration (e.g. “ $t_1$ ”). Herein, cathodic current (i.e. current that flows in such a direction as to reduce metal ions into atoms on the cathode surface) is defined as positive. In Figure 1.4, waveform (b) is characterized by a cycle that contains two cathodic pulses, since  $i_1 > 0$  and  $i_2 > 0$ . The cycle in waveform (c) contains one cathodic pulse ( $i_1 > 0$ ) and one “off-time” pulse ( $i_2 = 0$ ); during the “off-time” pulse, no current flows across the electrodes. The cycle in waveform (d) contains one cathodic pulse ( $i_1 > 0$ ) and one anodic pulse ( $i_2 < 0$ ); during the anodic pulse, atoms on the cathode surface are oxidized into metal ions, which usually dissolve back into the electrolyte.

The waveforms illustrated in Figure 1.4 have been used to electrodeposit metals and alloys in aqueous electrolytes [9, 86-100], and to a much lesser extent in ionic liquids [59, 101]. The “off-time” illustrated in waveform (c) has been found to affect aspects of the deposits, such as chemical composition [87, 91, 95, 96], chemical homogeneity [87], surface roughness [87, 89, 98], grain size distribution [59, 89, 93, 95, 97] and texture [91]. In recent years, reverse-pulsed waveforms, such as that shown in Figure 1.4(d), have been gaining much attention because anodic pulses have been found to significantly affect chemical composition [9, 101], chemical homogeneity [88], grain size [9, 102], and improve surface appearance [89, 99, 102] and internal stress in the deposits [9, 102]. In the case of single phase alloys, the anodic pulse selectively removes the element with the

highest oxidation potential, thus allowing control over the alloy composition. For multiphase alloy systems, the situation is more complicated—the extent to which each phase is removed during the anodic pulse depends not only on the relative electronegativity of each phase, but also on the arrangement and distribution of various phases. The use of reverse-pulsed waveforms to affect the phase composition, phase distribution and microstructural length-scales of multiphase alloy systems has been relatively unexplored.

### ***1.3. Problem statement***

The above sections suggest a number of possible areas for the development of nanostructured electrodeposited Al films for practical applications and fundamental studies. This thesis specifically seeks to address the following issues pertaining to their processing, structure and properties:

- Theoretical results in Appendix A indicate that low deposition temperature favors structural refinement. However, the processing, structure and properties of Al-Mn alloys electrodeposited at ambient temperature has not been investigated.
- Even though experimental works discussed in section 1.1.2 provide some hints that Mn promotes grain size refinement in Al-Mn electrodeposits, the crystal morphology and size, spatial distribution of the different phases, as well as nature of the amorphous phase, remain ambiguous.
- As discussed in section 1.2, reverse-pulsing improves the properties of metals and alloys deposited in aqueous electrolytes. However, this technique has not been employed in ionic liquids or to the deposition of Al alloys, nor has it been used to tune the structure of multi-phase alloys.

## ***1.4. Structure of thesis***

To address the issues outlined in section 1.3, the chapters of this thesis are organized as follows:

- Chapter 2: A detailed characterization of Al-Mn alloys electrodeposited at ambient temperature using a conventional current waveform is carried out to investigate the effects of Mn on nanostructure formation, and the character of the “amorphous” phase in electrodeposited Al-Mn alloys is established. The hardness and ductility of these alloys are assessed and related to alloy microstructure.
- Chapter 3: Using the processing-structure-property relationships established in chapter 2, a reverse-pulse current waveform is designed to tune the microstructure, so as to achieve high hardness and toughness.
- Chapter 4: To further characterize the Al-Mn alloys electrodeposited with a reverse-pulse current waveform in chapter 3, solute distribution in the nanocrystalline, amorphous, as well as dual-phase alloys are examined using three-dimensional atom probe tomography. A method is developed to enhance phase contrast in the dual-phase alloy, revealing in detail the composition and distribution of the two phases.

## **2. Electrodeposited Al-Mn alloys with microcrystalline, nanocrystalline, amorphous and nano-quasicrystalline structures<sup>1</sup>**

In this chapter, Al-Mn alloys are prepared at ambient temperature using a different electrodeposition solution than used in the studies reviewed in section 1.1.2. The purpose of this work is to systematically investigate the structure of electrodeposited Al-Mn alloys across a broad range of compositions (from 0 to 16 at.% Mn), through the transition from a microcrystalline to an amorphous structure. A detailed analysis of structure and composition, using combined analysis by XRD, DSC, TEM, HRTEM and scanning transmission electron microscopy (STEM) is presented. This chapter examines the “amorphous” phase for pre-existing grain nuclei. In addition, preliminary studies of the mechanical properties of these electrodeposits are discussed, and structures with hardness that exceeds 3 GPa are identified. The toughness of alloys with high hardness is also assessed using the guided bend test.

### ***2.1. Experimental procedures***

The Al-Mn alloys used in this study were prepared through a process of electrodeposition from a non-aqueous ionic liquid. All chemicals were handled in a glove box under a nitrogen atmosphere, with H<sub>2</sub>O and O<sub>2</sub> contents below 1 ppm. The organic salt, 1-ethyl-3-methyl-imidazolium chloride, [EMIm]Cl (>98% pure, from IoLiTec), was dried under vacuum at 60 °C for several days prior to use. Anhydrous AlCl<sub>3</sub> powder (>99.99% pure, from Aldrich) was mixed with [EMIm]Cl in a 2:1 molar ratio to prepare the deposition bath. Prior to deposition, pure Al foil (99.9%) was added to the ionic liquid, and the solution was agitated for several days, in order to remove oxide impurities and residual hydrogen chloride [57, 104]. After filtering through a 1.0 μm pore size syringe filter, a faint yellowish liquid was obtained. The nominal manganese chloride (MnCl<sub>2</sub>) concentrations were varied between 0 and 0.20 mol/L by

---

<sup>1</sup> The content of this chapter has been published in ref. [103]

controlled addition of anhydrous  $\text{MnCl}_2$  (>98% pure, from Aldrich) to the ionic liquid; the various  $\text{MnCl}_2$  contents used in this study are listed in Table 2.1. Electropolished copper (99%) was used as the cathode and pure aluminum (99.9%) as the anode. Electrodeposition was carried out at room temperature under galvanostatic conditions at a current density of  $6 \text{ mA/cm}^2$ . Alloy sheets of approximately  $20 \text{ }\mu\text{m}$  thickness were obtained after 4 hours.

**Table 2.1 Summary of the various electrolytic compositions used in this study, and the deposits produced with them. The global Mn content is measured by EDX and is reported with error bars; the size of surface features is measured from SEM images; the area % of FCC peaks is calculated from the X-ray diffractograms; average grain size is reported from both XRD and TEM measurements; the extent of Mn enrichment in the amorphous phase, as determined by STEM, is reported according to the formula of Equation (2-2).**

Molarity of $\text{MnCl}_2$ in electrolyte (mols/L)	0.0	0.015	0.03	0.05	0.07	0.075	0.09	0.11	0.13	0.20
Alloy composition (at. % Mn)	0.0	2.4 $\pm 0.1$	4.1 $\pm 0.1$	6.0 $\pm 0.2$	7.5 $\pm 0.2$	8.2 $\pm 0.2$	9.2 $\pm 0.2$	10.8 $\pm 0.3$	12.3 $\pm 0.3$	15.8 $\pm 0.3$
SEM surface features ( $\mu\text{m}$ )	14 $\pm$ 4	12 $\pm$ 4	10 $\pm$ 3	8 $\pm$ 3	7 $\pm$ 3	5 $\pm$ 2	5 $\pm$ 2	5 $\pm$ 2	6 $\pm$ 2	3 $\pm$ 1
Area % of FCC peaks	100	100	100	100	100	73 $\pm$ 1	46 $\pm$ 1	32 $\pm$ 1	21 $\pm$ 1	0
XRD grain size (nm)	-	-	-	-	-	19 $\pm$ 4	8 $\pm$ 2	4 $\pm$ 1	3 $\pm$ 1	-
TEM grain size (nm)	-	-	-	-	4000 $\pm$ 1000	40 $\pm$ 10, 4 $\pm$ 1	7 $\pm$ 2	6 $\pm$ 2	4 $\pm$ 1	-
Extent of Mn enrichment in amorphous phase						0.13 $\pm$ 0.01	0.28 $\pm$ 0.02	0.30 $\pm$ 0.02	0.34 $\pm$ 0.02	

Scanning electron microscope (SEM) images of the as-deposited surfaces were obtained using a Leo 438VP SEM, and chemical composition was quantified via energy dispersive x-ray analysis (EDX, X-ray Optics/AAT #31102). Prior to XRD measurements, the copper substrates were removed by dissolution in concentrated nitric acid. X-ray patterns of the free-standing Al-Mn films were obtained using a PANalytical X'Pert Pro diffractometer operating at 45 kV and 40 mA with a  $\text{Cu-K}\alpha$  radiation source and Bragg-Brentano parafocusing geometry. Diffraction data was collected over a range

of 5 to 130 °2 $\theta$  with a 0.0167 ° $\theta$  step size and 60 s count time per step. Data analysis was carried out using the software package MDI Jade 8. After accounting for a linear background profile, each diffraction peak was fitted with a regular Pearson VII function, yielding the position of the peak center and the full width at half maximum. The peak positions were used to refine the unit cell lattice parameters, while the full width at half maximum values were used to estimate the crystallite size via a modified Williamson-Hall method: A Cauchy-Gaussian relationship was used to separate instrumental from intrinsic (i.e., strain plus size) broadening. Strain broadening was approximated by a Gaussian function, while effects of crystallite size were captured with a Cauchy profile [105].

TEM specimens were prepared from the free-standing Al-Mn films by twin-jet electropolishing at 10 V in a 20% solution of perchloric acid in methanol at -60 °C. Selected alloy films were also ion-milled at -80 °C with an ion accelerating voltage of 4 kV and source current of 4 mA (Fischione Model 1010). The TEM specimens were examined using two TEM instruments: a JEOL 200CX and a JEOL 2010F, both of which were operated at 200 kV. The probe area used to obtain the selected area diffraction patterns was 1  $\mu$ m in diameter. Statistical analysis of the average grain size was carried out using both the bright-field and dark-field images; for each bright-field image, at least 4 dark-field images were obtained using the (111) and (200) reflections. These dark-field images were used to identify the grains on the bright-field image by hand. The grain size corresponds to the diameter of a circle with an equivalent area. For each specimen, at least 200 grains were analyzed. Chemical composition of the different nanostructures was studied quantitatively by EDX using the JEOL 2010F in STEM mode. A probe size of 1 nm was used and typical acquisition times were 200 s. Inca software was used to process the STEM/EDX data.

Calorimetric measurements of films with 15.8 at.% Mn were carried out in a Perkin-Elmer Diamond DSC under a nitrogen atmosphere. For each measurement, 4.0 mg of free-standing film pieces were sealed in an aluminum pan. Scanning measurements were made at 10 °C/min up to 520 °C. The sample was cooled to room temperature, and then re-heated to 520 °C at the same rate to obtain the baseline heat flow. Isothermal experiments were performed by heating the sample at 10 °C/min to 310



°C and then maintained at 310 °C for 55 minutes before cooling to room temperature. The baseline heat flow was obtained by repeating the isothermal experiment a second time on the same sample. X-ray diffractograms of the alloys subjected to both scanning and isothermal experiments were obtained using the PANalytical X'Pert Pro diffractometer following similar procedures as described earlier. Samples from the isothermal experiment were also observed using TEM (JEOL 2010F).

To evaluate the hardness of the alloys, nanoindentation tests were carried out using a Ubi1 nanoindenter from Hysitron Inc. (Minneapolis, MN) using a diamond Berkovich indenter. Samples were prepared for indentation through a standard regimen of mechanical polishing, to a surface roughness of less than 1 nm. The indentation depth was in all cases significantly less than 1/10<sup>th</sup> the film thickness, ensuring a clean bulk measurement. Each indentation was carried out with a loading rate of 4 mN/s and the maximum applied load was 10 mN. The instantaneous contact area was determined using the calibrated area function of the Berkovich tip, and hardness was determined using the Oliver-Pharr method [106]. Each reported data point represents an average of at least 36 indentations.

The guided-bend test, as detailed in ASTM E290-97a (2004), was employed to assess the ductility of selected alloys. The thickness,  $t$ , of tested samples (i.e. film and copper substrate together) was measured using a micrometer and ranged from  $0.220 \pm 0.02$  mm to  $0.470 \pm 0.02$  mm; and the radii of the end of the mandrel,  $r$ , ranged from 0.127 to 1.397 mm. After the guided bent test, the convex bent surfaces of our films were examined for cracks and fissures using the SEM. For each bent sample (i.e. film and copper substrate together), the thickness of the film was less than 10% that of the substrate. Thus, to a good approximation, the film lies on the outer fiber of the bent specimen, and experiences a state of uniaxial tension. The top half of the bent sample is in a state of tension, while the bottom half is in compression, and the neutral plane is approximately midway between the convex and concave surfaces. The true tensile strain on the convex surface is approximated as  $\varepsilon = \ln\left(\frac{l}{l_0}\right)$ , where  $l$  is the convex arc length

and  $l_0$  is the arc length of the neutral plane. Geometric considerations give

$$\varepsilon = \ln \left( \frac{r_t + 1}{r_t + \frac{1}{2}} \right).$$

## 2.2. Results

In this section we present detailed characterization results on all of the alloys prepared in this study. Rather than refer to the composition of the deposition bath, it is more convenient to label samples with their alloy composition, which is presented in Table 2.1 based on EDX analysis. Table 2.1 also assembles quantitative results from our SEM, XRD, TEM and STEM investigations, along with uncertainty ranges on all of our measured values.

### 2.2.1. SEM—Surface Morphology

A series of representative surface morphologies of the deposited alloys are shown in Figure 2.1. Broadly, two distinct classes of surface morphologies are observed. Alloys with global Mn content below about 7.5 at.% exhibit angular or polyhedral-like structures (Figure 2.1(a)-(d)), while alloys with higher Mn content exhibit a smoother morphology comprising rounded nodules (Figure 2.1(e)-(h)). The characteristic lengths of the surface structures are determined using a linear intercept method and the results are shown in Table 2.1. As the Mn content increases from 0 to 7.5 at.%, the characteristic length of the angular surface structures decreases continually from 14 to 7  $\mu\text{m}$ . For alloys with compositions between 8.2 and 12.3 at.% Mn, the average diameters of the nodules are about 5  $\mu\text{m}$ . For the 15.8 at.% Mn alloy, the nodules are only about 3  $\mu\text{m}$  in diameter.

The faceted and angular structures seen in Figure 2.1(a)-(d) are characteristic of conventional microcrystalline films, where each angular feature corresponds to a single grain [107]. The rounded nodule structures seen in Figure 2.1(e)-(h) are commonly observed in nanocrystalline electrodeposits when no organic leveling agents are used in the deposition; in such cases each nodule is a “colony” of many smaller grains [10, 99, 108]. The present data thus indirectly suggest that a structural transition from coarse- to fine-grained structures occurs in the vicinity of ~8 at.% Mn; more detailed structural analysis will clarify this point in what follows.

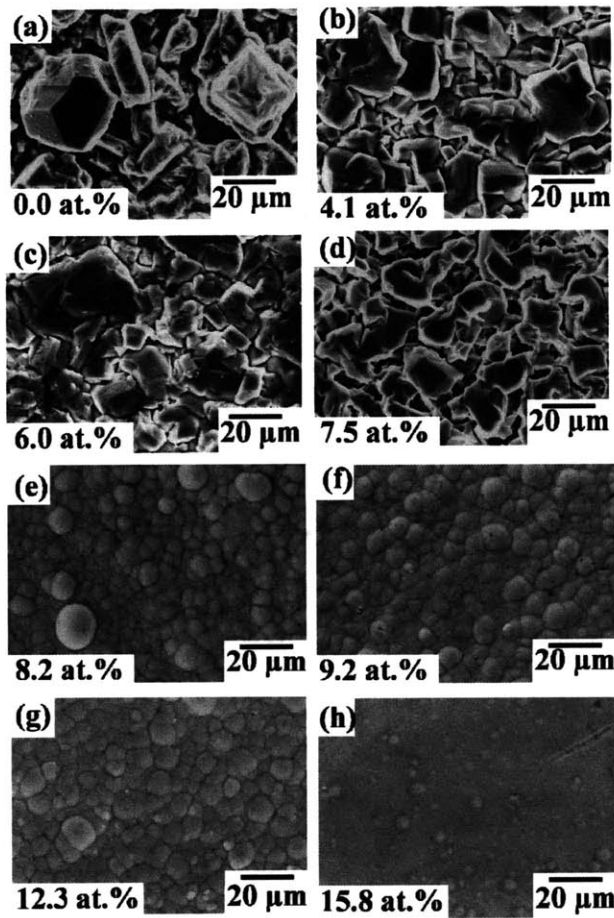


**Figure 2.1** SEM images of as-deposited Al-Mn alloys with global Mn content as shown in the lower-left corner of each panel. Note the transition from faceted features in images (a)-(d) to rounded nodules in images (e)-(h).

### 2.2.2. XRD—Phase identification and characteristics

Figure 2.2 illustrates the X-ray diffractograms of the as-deposited alloys. For alloys with global Mn content between 0 and 7.5 at.%, we observe peaks that are all consistent with the FCC Al(Mn) solid solution reflections. A broad and low-intensity amorphous-like halo starts to appear at  $2\theta \approx 42^\circ$  for the 8.2 at.% Mn alloy, and for alloys with global Mn content between 8.2 and 12.3 at.%, the patterns suggest that the Al-rich FCC phase coexists with an amorphous phase. The percent contribution of the FCC peaks to the total integrated intensities observed in each diffractogram is calculated and tabulated in Table 2.1. As the alloy composition increases from 8.2 to 12.3 at.% Mn, the FCC peak contribution decreases from 73 to 21%. For alloys with Mn content between 13.6 and 15.8 at.%, no FCC peaks are observed.

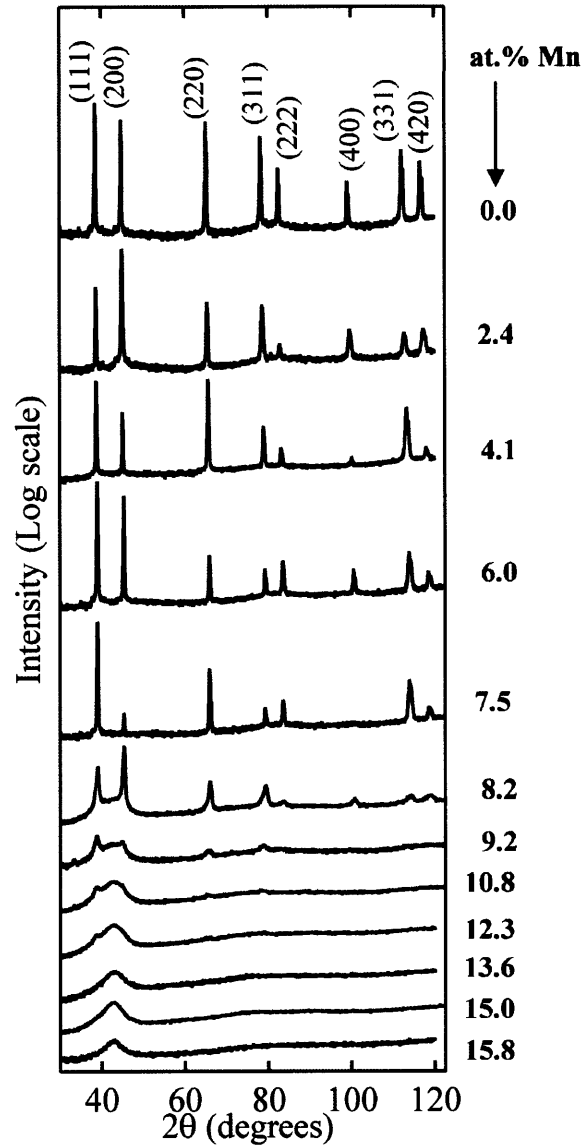


**Figure 2.2** X-ray diffractograms of as-deposited Al-Mn alloys, the compositions of which are shown at the right. Locations of the FCC Al(Mn) reflections are shown at the top. Note also the emergence of a broad amorphous halo at  $\sim 42^\circ 2\theta$  for compositions above 8.2 at%.

Also evident in Figure 2.2 is the shift in FCC peak positions as the alloy composition changes. We employ the Jade software to solve for the lattice parameter of each XRD profile; the software explicitly solves and corrects for systematic errors, such as in specimen positioning, and then uses the refined peak positions to obtain a least-squares fit for the lattice parameter. Figure 2.3 shows the lattice parameter of the FCC phase as a function of global Mn content of the alloys. As the Mn content increases from 0 to 7.5 at.%, the lattice parameter decreases from 4.049 to 4.005 Å. Beyond this point,

for the two-phase alloys, the opposite trend is observed: increasing the global Mn content from 8.2 to 12.3 at.% causes the lattice parameter to increase from 3.996 to 4.044 Å.

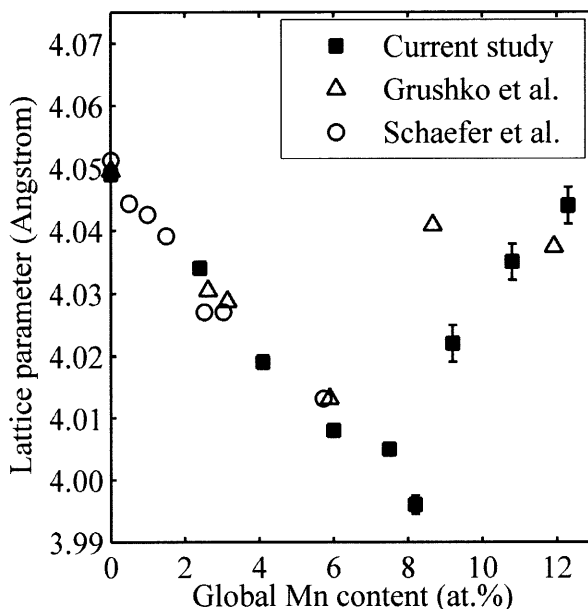


**Figure 2.3** Lattice parameter of the FCC phase, as calculated from peak positions in the X-ray diffractograms of Figure 2.2. Also shown for comparison are data obtained for Al-Mn alloys electrodeposited at 150 °C by Grushko and Stafford in ref. [61], and for melt-spun alloys by Schaefer et al in ref. [109].

As shown in Figure 2.2, for alloys with Mn content between 0 and 7.5 at.%, the FCC peaks are narrow. Thus, instrumental broadening effects dominate and the modified Williamson-Hall method is insufficiently resolved to determine the grain sizes of these alloys, which are greater than about 100 nm. On the other hand, the two-phase alloys with Mn content between 8.2 and 12.3 at.% exhibit significant FCC peak broadening, which increases with Mn content. Over this compositional range, the XRD grain sizes of these alloys, as tabulated in Table 2.1, decrease from 19 to 3 nm.

### 2.2.3. TEM—Phase distribution and structure

TEM samples that were jet-polished exhibited similar features to the ion-milled ones, and we conclude that sample preparation did not significantly alter the microstructure of the alloys. Bright field images and electron diffraction patterns of alloys with compositions ranging from 7.5 to 15.8 at.% Mn are shown in Figure 2.4.

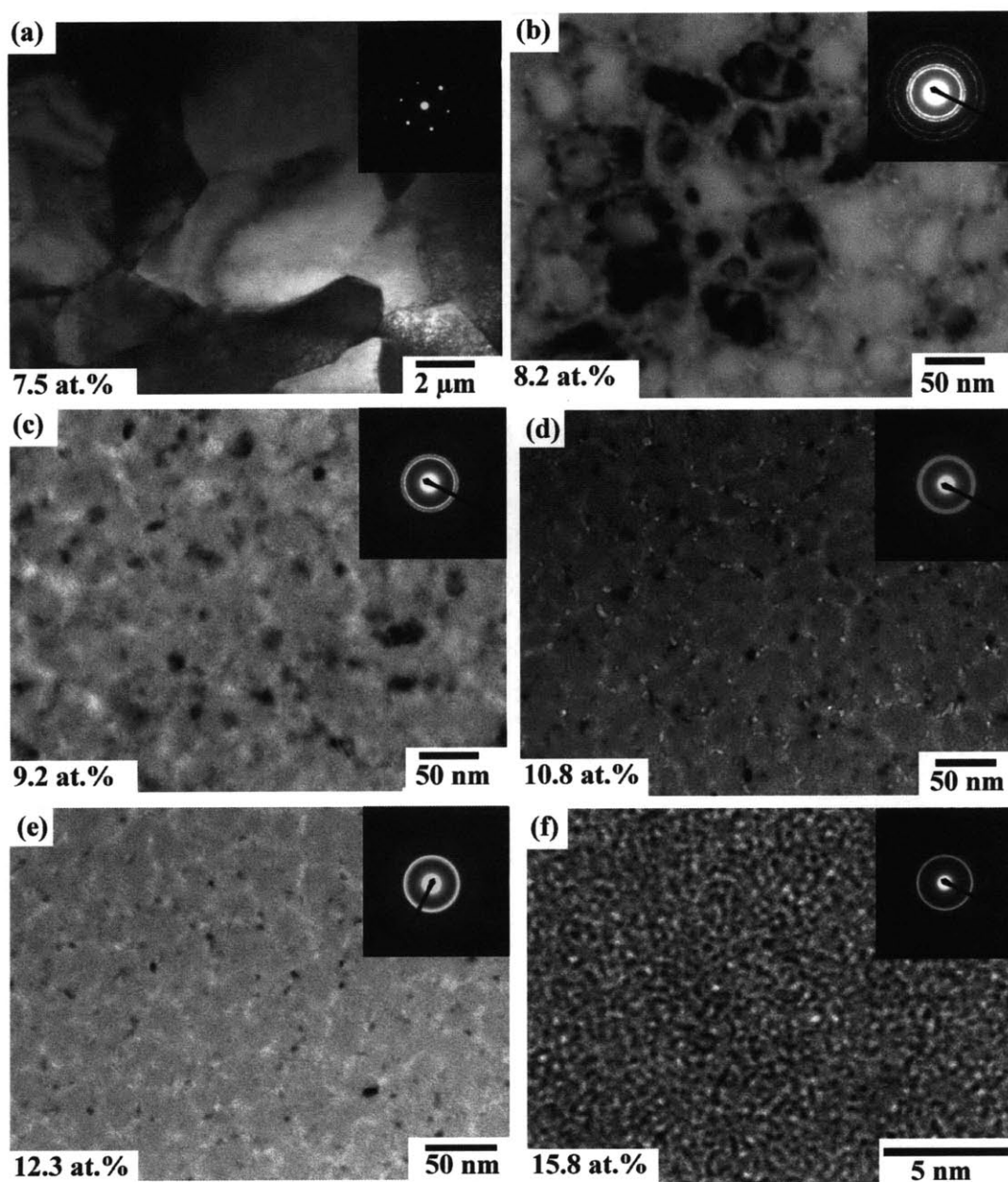


**Figure 2.4** Bright-field TEM images and electron diffraction patterns of as-deposited alloys with global Mn content as shown in the lower-left corner of each panel. Note the transition from micron-size grains in image (a) to nanocrystalline grains in images (b)-(e). Note also that images (b)-(e) show ~20-50 nm convex domains surrounded by a matrix or network structure.

The bright field image of an alloy with 7.5 at.% Mn (Figure 2.4(a)) shows that the grains have characteristic sizes between 3 and 10  $\mu\text{m}$ , in line with the  $\sim 7 \mu\text{m}$  surface features seen in the SEM in Figure 2.1(a). The electron diffraction pattern exhibits discrete spots consistent with a single phase FCC crystal structure. The zone axis of the electron diffraction pattern in Figure 2.4(a) is [111].

As shown in the bright field image in Figure 2.4(b), an 8.2 at.% Mn alloy consists primarily of grains that are approximately 40 nm in diameter. The rings in the electron diffraction pattern, as shown in Figure 2.5(a) for better clarity, are indexed consistently with an FCC crystal structure. The spottiness of the rings confirms that the FCC phase consists of small grains. However, unlike a conventional grain structure, these grains are apparently embedded in a matrix; rather than being separated by grain boundaries, they are separated by a network of matrix ligaments about 10 nm thick. At first glance, it might appear that what we term the “matrix” or “network” region in this system is amorphous, as suggested by the diffuse ring between the (111) and (200) reflections in the diffraction pattern (see Figure 2.5(a)). However, HRTEM reveals that the matrix region is more complex than this: a typical high resolution image is shown in Figure 2.6, revealing that the ~10 nm thick matrix region between large FCC grains (which are labeled ‘A’ in Figure 2.6) comprises small (~4 nm) crystallites (labeled ‘B’) in a featureless amorphous-like field (labeled ‘C’). We conclude that the 8.2 at.% Mn alloys consists of two phases- an amorphous-like phase and a FCC phase that has bimodal grain size distribution with peaks at ~40 nm and ~4 nm; the larger grains are surrounded by a network of the amorphous-like phase containing the smaller grains.

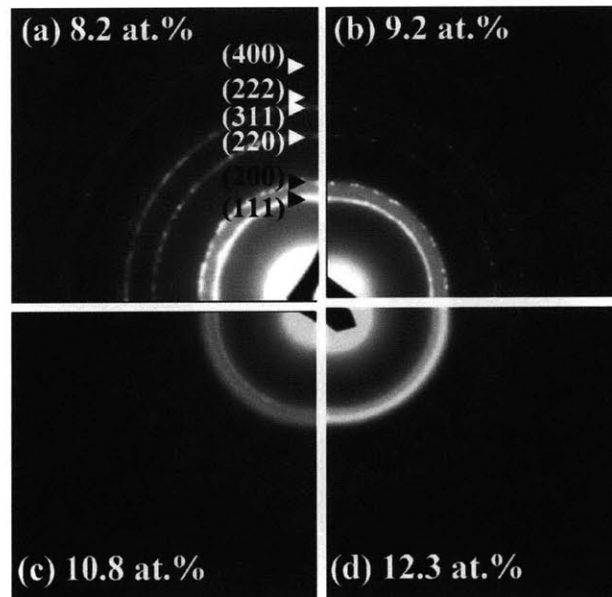


**Figure 2.5** Electron diffraction patterns of two-phase alloys with global Mn content labeled in each panel. Peak positions of the sharp reflections are indexed to be consistent with FCC Al(Mn), as shown in panel (a). Note that the relative intensity of the broad halo, whose peak position is located between the (111) and (200) reflections, increases as the global Mn content increases.

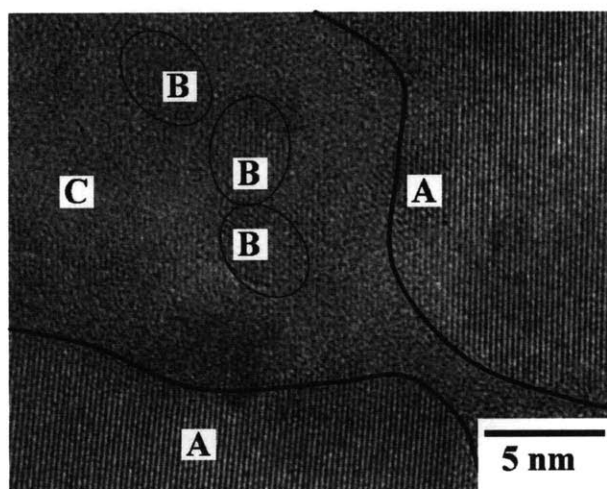


**Figure 2.6** HRTEM image of an 8.2 at.% Mn alloy, showing the “matrix” or “network” region between two large grains that are labeled ‘A’. This region comprises small ~4 nm crystallites (some of which are circled and labeled ‘B’) embedded in an amorphous-like field (labeled ‘C’).

The bright-field image of a 9.2 at.% Mn alloy is shown in Figure 2.4(c). We observe domains that are between 20 and 40 nm in diameter, again surrounded by a network region that is about 10 nm thick. However, unlike the 8.2 at.% Mn sample, in this sample the domains do not appear to be crystalline, and we can more clearly see a population of small crystallites located in the network structure, with sizes in the range of 5 – 10 nm. HRTEM image of the domains and their surrounding network structure is shown in Figure 2.7(a). Here the domains are outlined in bold and labeled ‘D’, and seem featureless. A higher magnification image of the network region, taken from the region denoted by dotted lines in Figure 2.7(a), is shown in Figure 2.7(b). Figure 2.7(b) provides compelling evidence that the network comprises mainly small crystallites (labeled ‘E’). The spots that constitute the FCC rings in the electron diffraction pattern of the 9.2 at.% Mn alloy (Figure 2.5(b)) are finer than in the 8.2 at.% Mn alloy (Figure 2.5(a)), which is consistent with the smaller grain sizes observed in the bright field images. In addition, the electron diffraction pattern in Figure 2.5(b) also shows that the intensity of the diffuse ring relative to the FCC rings is higher than that shown in Figure 2.5(a), suggesting a higher amorphous phase fraction in line with the XRD results in Table 2.1. In short, the 9.2 at.% Mn alloy apparently also has two phases, comprising an amorphous-like phase that exists as large convex domains, embedded in a network of small FCC crystals of about 5 to 10 nm diameter.



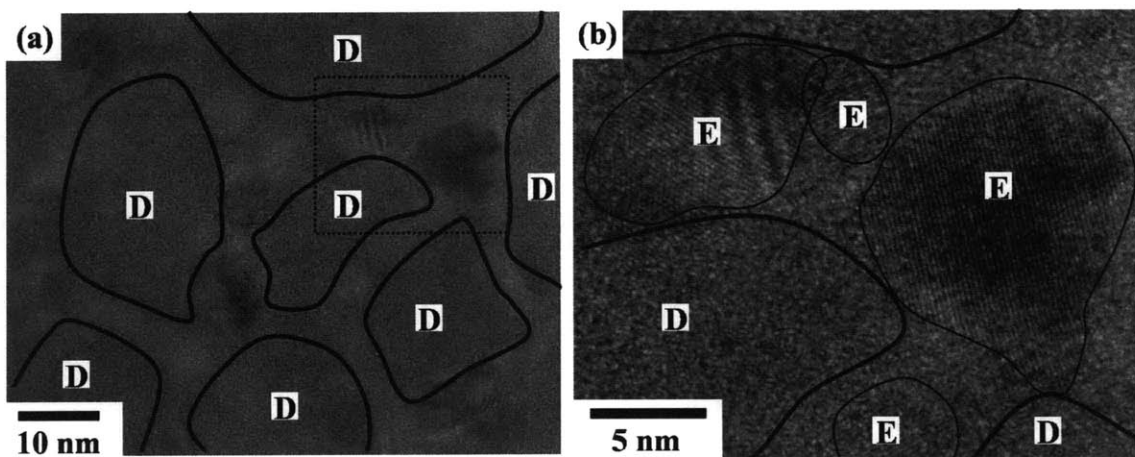


Figure 2.7 HRTEM images of a 9.2 at.% Mn alloy, showing domains and the surrounding network structure in (a), where the domains are outlined in bold and labeled ‘D’, and appear featureless. A higher magnification image of the surrounding network region, taken from the region denoted by dotted lines in (a), is shown in (b). The network region comprises mainly small crystallites (labeled ‘E’).

Bright field images of the 10.8 and 12.3 at.% Mn alloys are shown in Figures 2.4(d) and (e). The features observed in these images are very similar to those seen in Figure 2.4(c): amorphous domains are surrounded by a network structure comprised mainly of crystallites. As the alloy composition increases from 10.8 to 12.3 at.% Mn, the average crystallite diameter decreases to just a few nm. The electron diffraction patterns of both alloys (Figure 2.5(c) and (d)) consist of continuous FCC rings and the diffuse halo, consistent with a duplex structure of fine grains and an amorphous-like phase. As the Mn content increases from 10.8 to 12.3 at.%, the relative intensity of the diffuse ring increases, thus suggesting an increasing amount of amorphous-like phase, which agrees with the XRD results in Table 2.1.

For alloys with compositions above 13.6 at.% Mn, the TEM images appear featureless. Figure 2.4(f) shows a HRTEM image of an as-deposited 15.8 at.% Mn alloy. No lattice fringes are observed, indicating that the alloy lacks long-range order, thus resulting in the halo observed in the electron diffraction pattern.

#### 2.2.4. STEM—Phase composition

As noted above, for a range of Mn contents between about 8.2 and 12.3 at.%, we observe two-phase structures that comprise larger grains or domains embedded in a matrix or network. For these alloys, the local chemical compositions of the domains and

the network regions are analyzed using STEM/EDX and the results are shown in Figure 2.8.

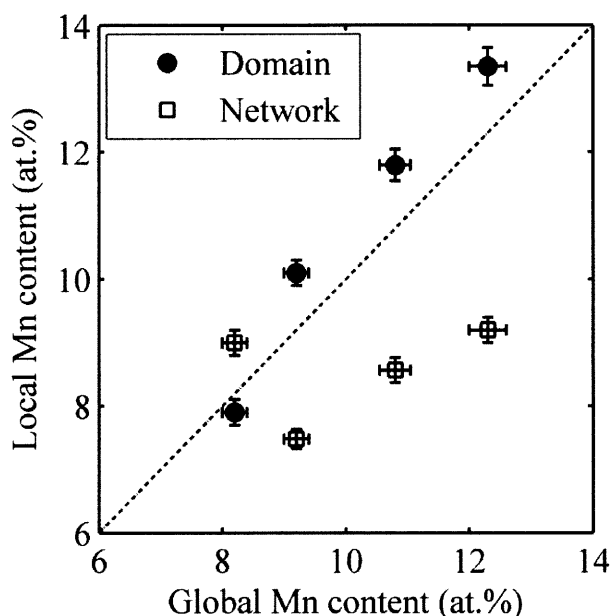


**Figure 2.8 STEM results comparing local compositions of domain and network regions of the two-phase alloys, along with a dashed line showing the expected composition for a homogeneous alloy. The amorphous phase is located in the network regions for the 8.2 at.% Mn alloy, but in the domain regions for alloys with higher Mn contents. Thus, Mn preferentially partitions to the amorphous phase for all these alloys.**

For an 8.2 at.% Mn alloy, recall that the ~40 nm diameter “domains” were in fact FCC solid solution crystals (see Figure 2.4(b) and the regions labeled ‘A’ in Figure 2.6). In Figure 2.8 we now see that these larger grains are depleted of Mn, whereas the featureless regions on the network (labeled ‘C’ in Figure 2.6) are enriched with Mn. Their compositions are 7.9 and 9.0 ( $\pm 0.2$ ) at.%, respectively. For alloys with higher global Mn content, the partitioning tendency of Mn is reversed: the domains, which are apparently amorphous (see Figure 2.4(c) and regions ‘D’ in Figure 2.7(b)) are enriched with Mn, while the surrounding network of crystallites is depleted of Mn. As the global Mn content increases from 9.2 to 12.3 at.%, the Mn content of the larger domains increases from 10.1 to 13.4 at.% and the composition of the network increases from 7.5 to 9.2 at.%. In all of the data collected in Figure 2.8, there is thus one common feature: the microstructures are duplex, and the amorphous-like regions are always found to have an enrichment of Mn, while the crystalline regions are depleted of Mn. The specific arrangement of these phases is different from lower to higher Mn content, but the tendency of Mn to preferentially populate the amorphous regions is consistent.

### 2.2.5. DSC--Structure of the amorphous phase

The scanning calorimetry signal from a 15.8 at.% Mn sample at a heating rate of 10 °C/min is shown in Figure 2.9(a), exhibiting a first exothermic peak at 341 °C and a second at 463 °C. The enthalpy of the first transformation is 900 J/mol, much smaller than that of the second transformation at 2770 J/mol. Qualitatively, we note that both peaks are asymmetric, and whereas the rising edge of the first peak is steeper, the converse is observed for the second peak. Figure 2.9(b) shows the calorimetric signal from another 15.8 at.% Mn sample that is subject to isothermal heat treatment at 310 °C—just at the onset of the first transformation—where a monotonically decaying signal is observed. The total heat evolved is 840 J/mol, which is close to that of the first crystallization event observed in the scanning experiment.

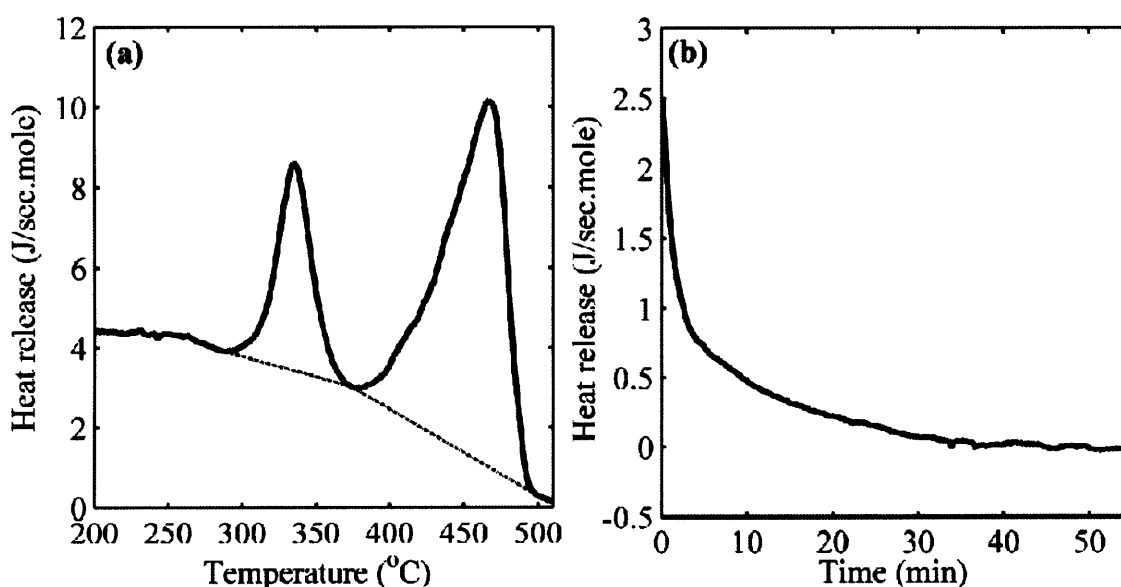
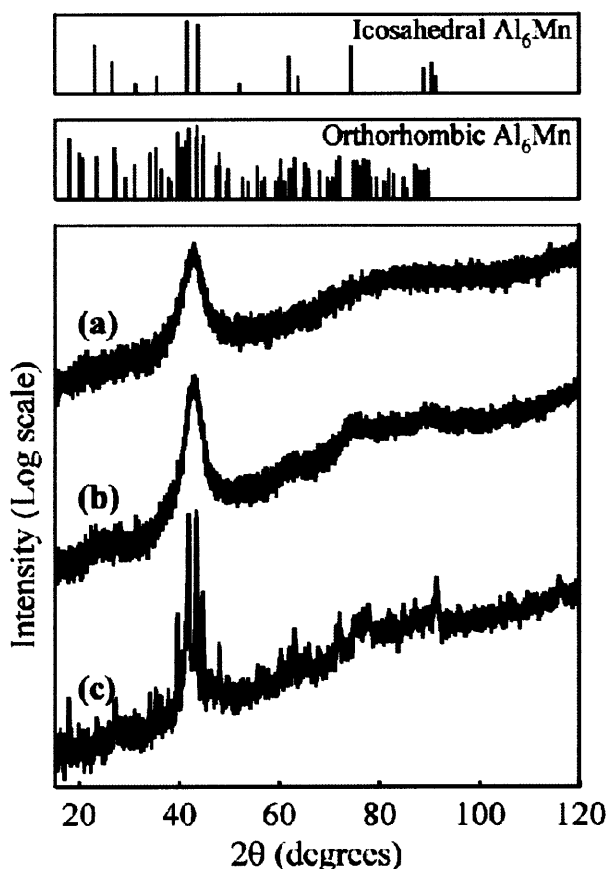


Figure 2.9 (a) A Scanning-mode DSC trace showing the two exothermic peaks observed when a 15.8 at.% Mn alloy was heated from 30 °C to 520 °C at 10 °C/min. Using the dotted lines as baselines, the enthalpies of the two transformation events were 900 J/mol and 2770 J/mol respectively. (b) The isothermal DSC output for a 15.8 at.% Mn alloy annealed at 310 °C for 55 minutes; the total heat evolved was 840 J/mol.

X-ray diffractograms of samples subjected to these thermal cycles in the DSC are shown in the bottom panel of Figure 2.10 along with data for an as-deposited specimen. Along the top of this figure the expected peak positions and relative intensities of the icosahedral and orthorhombic Al<sub>6</sub>Mn phases are shown, as obtained from the x-ray powder diffraction files (PDF#00-044-1195 and 00-041-1285 respectively) [110]. The

diffractogram of the as-deposited alloy, labeled (a), exhibits a broad halo at  $2\theta \approx 42^\circ$ , and another lower intensity hump at  $2\theta \approx 80^\circ$ . After isothermal annealing at  $310^\circ\text{C}$ , however, a series of additional broadened peaks appear at positions that correspond well to the icosahedral  $\text{Al}_6\text{Mn}$  produced by rapid quenching [111]. The diffractogram (labeled (c)) of the sample that was heated to  $520^\circ\text{C}$  during the scanning experiment (i.e., across both exothermic reactions) exhibits sharp peaks that are consistent with orthorhombic  $\text{Al}_6\text{Mn}$  [112].



**Figure 2.10** X-ray diffractograms of 15.8 at.% Mn samples (a) in the as-deposited state, (b) after isothermal treatment at  $310^\circ\text{C}$  for 55 minutes and (c) after being heated from  $30^\circ\text{C}$  to  $520^\circ\text{C}$  at  $10^\circ\text{C}/\text{min}$ . For comparison, the top panel shows peak positions and relative intensities of icosahedral  $\text{Al}_6\text{Mn}$  produced by rapid quenching in ref. [111], while the second panel shows those for orthorhombic  $\text{Al}_6\text{Mn}$  in ref. [112].

Figure 2.11 shows a HRTEM image of a 15.8 at.% Mn sample that was subject to isothermal annealing at  $310^\circ\text{C}$ . Lattice fringes are clearly evident and the grain size is approximately 2 nm. This value agrees well with the results of a Williamson-Hall analysis of the XRD data in Figure 2.10 (curve b), which yields a grain size for the icosahedral phase of  $\sim 2$  nm. The electron diffraction pattern, as shown in Figure 2.11

exhibits continuous rings. The diffraction peak positions are similar to those of icosahedral Al-Mn particles studied by Bendersky and Ridder [81]. Figure 2.12(a) and (b) show the electron diffraction patterns of the as-deposited and annealed samples respectively. We note that the diffraction pattern of the annealed sample consists of rings that are sharper and more discernible than that of the as-deposited sample, and which are consistent with the reflections expected for the icosahedral phase.

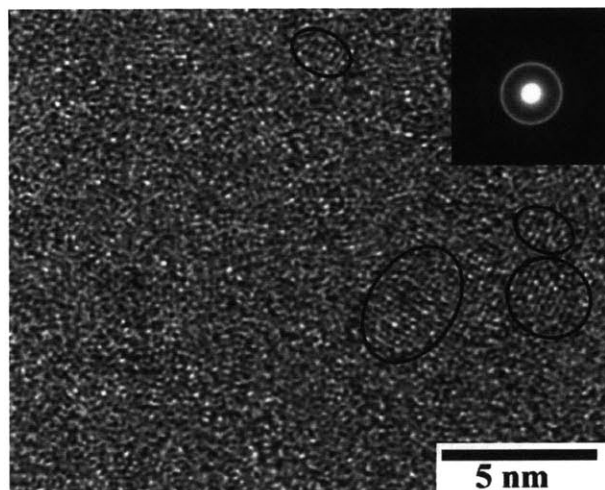


Figure 2.11 HRTEM image and electron diffraction pattern of a 15.8 at.% Mn alloy after isothermal annealing at 310°C for 55 minutes. As compared to the as-deposited condition, which was apparently amorphous (Figure 2.4(f)), this specimen exhibits small regions with clear lattice fringes. Some of the crystallites are outlined in bold; the average grain size is about 2 nm.

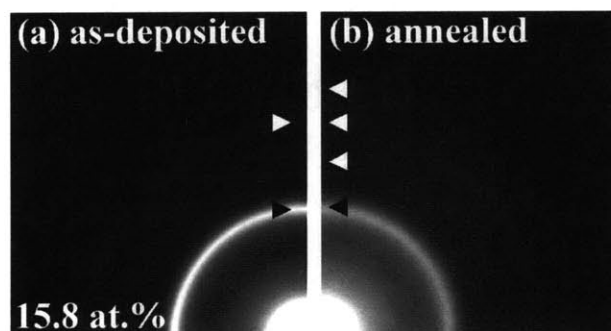
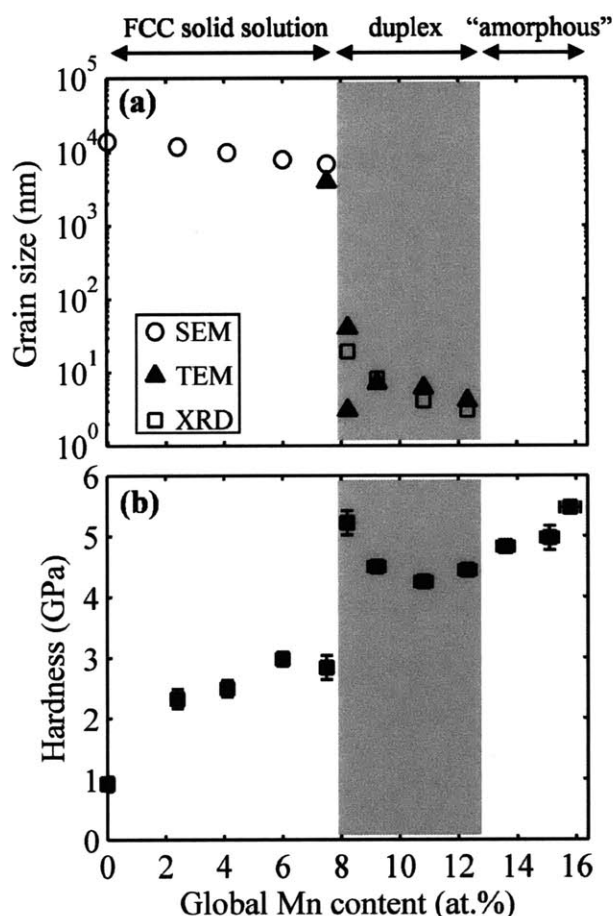


Figure 2.12 Electron diffraction patterns of 15.8 at.% Mn alloys (a) in the as-deposited state and (b) after isothermal annealing at 310 °C for 55 minutes. Note the appearance of additional reflections in (b), which are indexed as consistent with the icosahedral phase. The arrows indicate the positions of the rings in each panel.

#### 2.2.6. Nanoindentation—hardness

Figure 2.13 shows the measured hardness values of the various deposits, in comparison to their structural length scales. The hardness of pure microcrystalline

electrodeposited Al is about 1 GPa. For the single FCC phase alloys, increasing the Mn content from 0 to 7.5 at.% Mn causes the hardness to increase from 1 to 2.8 GPa. At 8.2 at.% Mn, hardness reaches a local maximum value of 5.2 GPa. Further increase in Mn content causes the hardness to decrease to a local minimum of 4.3 GPa near 10.8 at.% Mn, followed by an increase to 5.4 GPa for our sample with highest Mn content.



**Figure 2.13** (a) Plot summarizing the grain/crystal size measurements of the FCC solid solution phase as determined by various techniques. Phase compositions of the alloys are labeled at the top of the panel. (b) Plot of hardness vs. alloy composition; notice that the dramatic decrease in grain size at ~8.2 at.% Mn is accompanied by an increase in hardness by about a factor of 2.

### 2.2.7. Guided bend test—ductility

Figure 2.13 shows that the nanostructured and amorphous Al-Mn alloys with Mn content above 8.2 at.% exhibit impressive hardness that exceeds 3 GPa. Guided bend tests were performed on alloys containing 8.2 at.%-Mn and 13.6 at.%-Mn. Figure 2.14 illustrates SEM images of the convex bent surfaces of these alloys upon application of

~5% tensile strain. Figures 2.14(a) and (c) show that both alloys exhibit multiple cracks that propagate across the entire sample widths and the corresponding higher magnification images on the right illustrate relatively straight crack paths, which is characteristic of catastrophic failure in brittle materials. Thus, Figure 2.14 shows that the ductility of these alloys falls below ~5%.

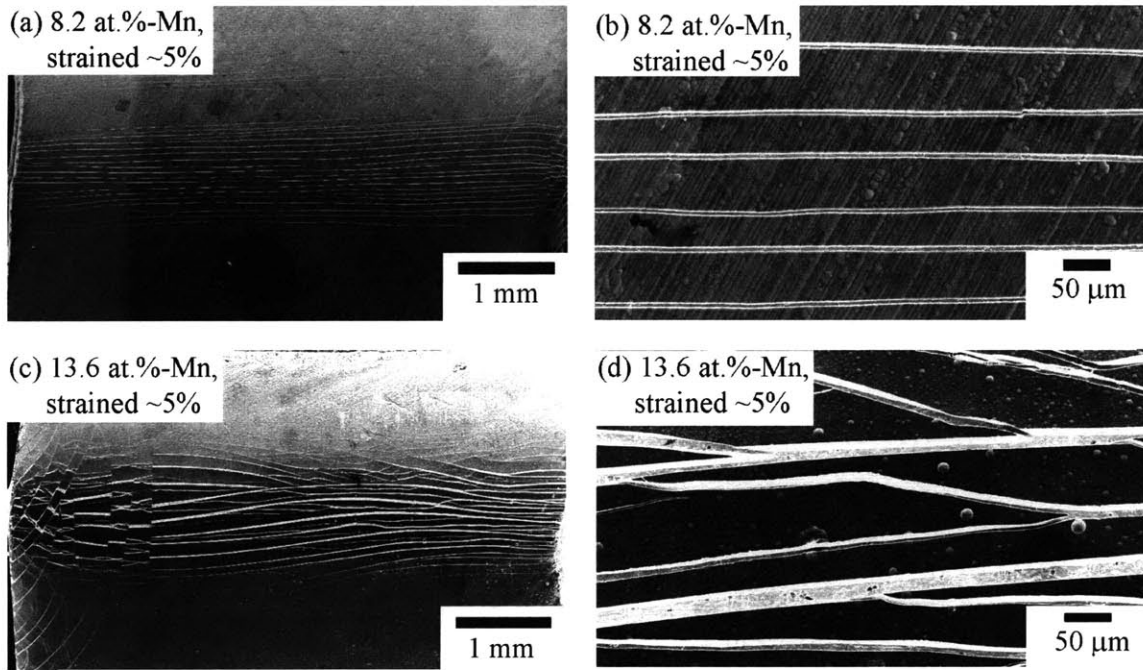


**Figure 2.14** SEM images of the convex bent surfaces of the 8.2 at.%-Mn and 13.6 at.%-Mn alloys upon application of ~5% tensile strain are shown in (a)-(b) and (c)-(d), respectively. The relatively straight crack paths are characteristic of brittle fracture.

### 2.3. Discussion

The above results show the following general trend as Mn increases in our deposits. First, at low Mn levels below about 7.5 at.%, the deposits are FCC and have micron-scale grains that decrease in size with Mn content. Second, at intermediate Mn levels (between 8.2 and 12.3 at.%) we see complex dual-phase structures involving nano-scale FCC crystallites and domains of amorphous-like material. Finally, at sufficiently high Mn levels (above 13.6 at.%) we see only the amorphous-like phase, which transforms first to a quasicrystalline phase and then intermetallic  $\text{Al}_6\text{Mn}$  upon heating. In the following sections, we discuss in more detail the phases and microstructures in these alloys.

### 2.3.1. Phase composition

Even though the maximum equilibrium solubility of Mn in Al is 0.62 at.% [113], Figure 2.2 shows that our electrodeposited alloys exhibit a single FCC phase up to about 7.5 at.% Mn. Such extended solubility is frequently found in electrodeposited alloys because of the non-equilibrium processing conditions [69]. For our single FCC phase alloys, the decrease in lattice parameter with increasing Mn content, as shown in Figure 2.3, is indicative of Mn (which has a smaller Goldschmidt radius than Al by about 11%) being substitutionally incorporated into the Al lattice. Figure 2.3 also shows that our results are in very good quantitative agreement with those obtained for melt-spun alloys [109] and alloys electrodeposited from  $\text{AlCl}_3\text{-NaCl}$  electrolyte at 150 °C [61]. The following equation relates the lattice parameter,  $a$  (Å), of our single phase alloys to the global atomic fraction of Mn,  $X_{\text{Mn}}$ :

$$a = a_0 - bX_{\text{Mn}} , \quad (2-1)$$

where  $a_0$  is the lattice parameter of pure Al (4.049 Å) and  $b = 0.640$  Å.

At the first appearance of the amorphous phase at 8.2 at.% Mn, the FCC lattice parameter is the lowest at 3.996 Å. While this result may suggest that the FCC phase is the most super-saturated at this composition, we note that the microstructure of an 8.2 at.% Mn alloy exhibits two types of crystallites, which differ not only in their grain size, but also in their local environment (Figure 2.4(b) and 2.8). Thus, these two types of crystalline grains may have different lattice parameters. Additionally, the bimodal grain size distribution may have implications on the XRD peak locations, which may thus affect the accuracy of our lattice parameter calculations.

For even higher Mn contents ( $\geq 9.2$  at.%), Figure 2.3 reflects an increasing lattice parameter of the FCC phase. We suggest that this increase is a result of Mn partitioning into the amorphous-like phase (cf. Figure 2.7), depleting from the FCC crystallites and thus reducing their lattice parameter according to Equation 2-1). Using our STEM data, we compare the extent of Mn enrichment in the amorphous phase by introducing a normalized enrichment parameter,  $\eta$ , as:



$$\eta = \frac{(X_{Mn}^{amorphous} - X_{Mn}^{FCC})}{X_{Mn}}, \quad (2-2)$$

where  $X_{Mn}^{amorphous}$  and  $X_{Mn}^{FCC}$  correspond to the atomic fraction of Mn in the regions that consist primarily of the amorphous and FCC phases respectively. The results are shown in Table 2.1. As the global Mn content increases from 8.2 to 12.3 at.%, the Mn enrichment in the amorphous phase increases from 0.13 to 0.34.

Our results above are broadly in line with those for alloys electrodeposited at 150 °C by Grushko and Stafford [61, 70]. They observed a single FCC phase up to 5.9 at.% Mn, and at 8.7 and 11.9 at.% Mn found an amorphous phase co-existing with an FCC phase depleted in Mn [61, 69]. Whereas these authors only inferred the composition of the FCC crystals from the inflection in lattice parameter measurements (cf. Figure 2.3), here we have more direct confirmation of Mn partitioning from our STEM data and the values of  $\eta$  in Table 2.1. Because Grushko and Stafford did not examine alloys of composition between 5.9 and 8.7 at.% Mn, we are not able to precisely compare the composition at which the alloys transition from a single crystalline phase to a duplex structure, although it is clearly in the general vicinity of the transition that we observe in our deposits.

### ***2.3.2. Amorphous phase character***

The shapes of the peaks in the DSC signal obtained from heating the 15.8 at.% Mn alloy (Figure 2.9(a)) give an indication that the first and second exotherms correspond to different types of transformation events. [114] and Chen et al. [82-84] modeled the nucleation-and-growth process during such a linear heating profile using a modified Johnson-Mehl-Avrami equation. They showed that for a transformation involving nucleation and growth of a new phase, the trailing edge of the exothermic peak should be steeper than the leading edge. On the other hand, for the case of phase growth from pre-existing nuclei, the leading edge should be steeper than the trailing edge. With these results in mind, examination of Figure 2.9(a) suggests that the first exotherm corresponds to a transformation that proceeds by growth from pre-existing nuclei, whereas the second corresponds to a nucleation-and-growth process. Additionally, the enthalpy of the first transformation event (900 J/mol) is unusually small compared to that

of crystallization from a truly amorphous metal (usually a few kilojoules per mole), which is consistent with the first event being one of growth from pre-existing nuclei [83, 115].

While scanning calorimetric experiments provide qualitative hints on the nature of a transformation event, isothermal experiments such as those in Figure 2.9(b) allow unambiguous determination of the transformation type. Again, the work of Chen et al. [82-84] provides some guidance in the interpretation: for nucleation and growth a peak should be observed in the heat flow at non-zero time due to the formation of nuclei, whereas during a growth process from pre-existing nuclei, a monotonically decreasing signal should be observed. Thus, the monotonically decreasing signal obtained upon annealing our 15.8 at.% Mn alloy (Figure 2.9(b)) provides compelling evidence that our as-deposited alloy, nominally called “amorphous” based on diffraction data, in fact contained pre-existing nuclei.

Our microscopic and XRD evidence also conform to the above interpretation. In the as-deposited state, HRTEM reveals an amorphous-like structure, whereas after isothermal annealing at 310 °C pre-existing nuclei grew to a clearly discernible size in the range of 1-3 nm (see Figure 2.11). What is more, these grains exhibit diffraction patterns consistent with the icosahedral phase (Figures 2.10(b), 2.13 and 2.14(b)). Thus, these HRTEM and DSC results together establish that our as-deposited 15.8 at.% Mn is seeded with pre-existing quasicrystalline nuclei that grow into nano-quasicrystalline domains upon annealing at low temperatures (~310 °C). Annealing at higher temperatures leads to the nucleation-and-growth transformation to orthorhombic  $\text{Al}_6\text{Mn}$  crystalline grains.

Our results present a clear parallel to those of Chen and co-workers, who carried out a calorimetric study on magnetron sputtered Al-17 at.% Mn films [82-84]. In their scanning experiments, two exotherms qualitatively similar to ours were observed. The first exotherm obtained in both that study and ours have similar peak temperatures (341 °C and 337 °C) and heats of transformation (900 J/mol and 1046 J/mol, respectively). Monotonically decreasing signals were obtained upon isothermal annealing of their samples in the vicinity of the first exothermic peak, and their annealed samples exhibited diffraction patterns consistent with the icosahedral phase. The structure of the

“amorphous” phase in the sputtered films of Chen et al. is thus believed to be essentially similar to that seen in our electrodeposited films.

We note that when Grushko and Stafford thermally annealed their “amorphous” 16 at.% Mn alloy that was electrodeposited at 150 °C, they also observed the formation of very small icosahedral grains, which transformed to intermetallics with further annealing [73]. However, to our knowledge, our results here represent the first time that the apparently “amorphous” structure of Al-Mn electrodeposits has been established as containing pre-existing nanoquasicrystalline nuclei. Additionally, our observation that these pre-existing nuclei grow into clearly discernible quasi-crystals at about 300° C helps to unify prior reports in the literature, where deposition at 325° C directly yielded the quasicrystalline phase [71], while deposition at lower temperatures led to an apparently amorphous phase [61, 69, 70]. In combination with these literature results, our analysis suggests that quasicrystalline order is in fact preferred at all deposition temperatures; below about 300° C, the quasicrystalline nuclei are sufficiently small that the structure appears amorphous, while above this temperature they grow to the ~2-3 nm required to discern them in diffraction data and HRTEM images.

### ***2.3.3. Structure-composition relationship***

The structures produced in this study span an impressive range of length scales, ranging from supermicron FCC grains (e.g., Figure 2.1(a)) to extremely fine nanocrystals of dimension ~3 nm (e.g., Figure 2.6). No single characterization technique can be used to assess grain/domain sizes across this entire range, so in this section we compile our measurements from various techniques, to develop a picture of how the characteristic structural length scales change with composition.

Across the entire range of composition examined, the size of the FCC solid solution phase, including grains and embedded crystallites, decreases as the global Mn content increases, as shown in Figure 2.13(a). For the single phase alloys, as the Mn content increases from 0 to 7.5 at.%, the average crystallite size decreases from 15 to 7  $\mu\text{m}$ . At around 8 at.%, the grain size decreases drastically from several microns to nanometer-scale dimensions, and it is also at this composition that we observe a bimodal distribution of crystallites (~40 and 4 nm). At higher Mn content, from 9.2 to 12.3 at.%,

the average crystallite size decreases further to about 4 nm. Beyond this point, the apparently amorphous structure contains nano-quasicrystalline nuclei, which must be of ~1 nm or finer scale.

The monotonic relationship between grain size and solute content of our single phase alloys (i.e., 0 to 7.5 at.%) has also been observed in other alloy systems, such as Ni-W and Ni-P [17, 20], where the observed trend has been attributed to grain boundary segregation effects (i.e. because solute segregation to the grain boundaries reduces the grain boundary energy, increasing the solute content allows promotes finer grains [16, 116]). In light of this possibility, we carried out STEM analysis of the grain boundaries and grain interior regions for some of our single phase alloys. We also used Auger electron spectroscopy to compare the Mn content at the intergranular and transgranular regions using standard procedures [117]. Both techniques yielded similar results: there was insignificant variation in composition between the bulk and grain boundaries. We conclude that the progressive refinement of structure as summarized in Figure 2.13 is not principally driven by segregation of solute to intergranular regions.

On the other hand, the structure-composition relationship may be related to nucleation kinetics at the electrode. Stafford carried out linear sweep voltammetry in a 2:1 mole ratio  $\text{AlCl}_3\text{:NaCl}$  electrolyte and found that as the content of  $\text{MnCl}_2$  in the electrolyte increases, the cathodic overpotential becomes more negative [64]. A similar trend was also observed in the  $\text{AlCl}_3\text{-NaCl-KCl}$  electrolyte by Hayashi [118]. Assuming that our ionic liquid electrolyte behaves similarly, an increase in  $\text{MnCl}_2$  content in the electrolyte would drive the cathodic overpotential more negative, which in turn favors the nucleation of new grains, and thus a finer grain size, during electrodeposition [119-121].

Upon the appearance of a second phase at higher Mn content (> 8 at.%), the FCC grain size decreases drastically from microns to nanometers. Recall that the structures of all the two-phase alloys exhibit one similarity: they all contain domains that are between 10 and 25 nm in radius, and surrounded by a network or matrix structure. We speculate that this recurring characteristic length scale may be associated with the characteristic diffusion distance,  $L$ , for atoms on the surface of the growing film. Given a deposition rate of 5  $\mu\text{m/hr}$ , we take  $\tau \approx 0.2$  s as a characteristic time to deposit one monolayer, and for Al surface self-diffusion, a typical diffusivity  $D \approx 4 \times 10^{-12}$   $\text{cm}^2/\text{s}$  at ambient

temperature [122]. With these values we approximate a diffusion length of  $L \approx 2\sqrt{D\tau} = 18$  nm, very close to the characteristic radius (10-25 nm) of the domains in our deposits. Interestingly, in Grushko and Stafford's studies, similar domains were also observed in a 12 at.% alloy, but with a larger characteristic domain size ranging from 125 to 250 nm in radius [61, 69, 70]. Because Grushko and Stafford used higher current densities (as much as ten times higher), we approximate  $\tau \approx 0.02$  s, and given their higher deposition temperature of 150 °C,  $D \approx 3 \times 10^{-9}$  cm<sup>2</sup>/s. The approximate surface diffusion length in this case is about 150 nm, again in good agreement with the experimental scale of the structural domains. These considerations offer some support for the notion that phase separation in these alloys is a surface phenomenon that occurs during electrodeposition, and that the surface diffusion length governs the domain size of two-phase electrodeposits (cf. Figure 2.4(b)-(e)).

#### **2.3.4. Hardness of the deposits**

It is beyond our scope to provide a detailed mechanistic interpretation of the hardness trends seen in Figure 2.13(b), especially in light of the fact that many of our deposits have extremely complex duplex structures, the hardness of which is not simply predicted. However, since these measurements are, to our knowledge, the first mechanical property data presented for Al-Mn alloys electrodeposited from ionic liquid, we offer a few observations about our results.

First, the initial increase in hardness from 0 to 7.5 at.% Mn covers the range of compositions where the alloys remain single-phase FCC solid solutions and the grain size decreases; the strength increase can likely be attributed to the combined effects of solution strengthening and the Hall-Petch effect. Second, within the composition range of 13.6 to 15.8 at.% Mn, the alloys are “amorphous” (containing nanoquasicrystalline nuclei), and hardness increases with Mn content. The role of solute content on the strength of amorphous phases is neither simple nor well understood, but the negative heat of mixing of our system indicates that Mn additions increase the average bond strength in the alloy, which, all other things being equal, would promote higher hardness. Other amorphous Al alloys are hardened by increases in solute content in a similar way [123-125]. Changes in the degree of chemical order (the density of nano-quasicrystalline

nuclei) with Mn content are also plausible, and could lead to strengthening in the manner well-known for amorphous metals containing nanocrystals [126-128]. A similar argument could explain the decrease in hardness from 8.2 to 10.8 at.% Mn, over which range the structure is essentially an amorphous/nanocrystal composite, but with a decreasing volume fraction of reinforcing nanocrystalline particles at higher Mn levels. In any event, it is interesting to observe that the complex changes in structure we observe with Mn content in these alloys are mirrored by unusual trends in hardness; the suggestion that there may be local optimums in the composition space (e.g., at ~8 at.% Mn) is also of practical interest.

### ***2.3.5. Ductility of nanostructured and amorphous alloys***

Even though the nanostructured and amorphous alloys exhibit high hardness that exceeds 3 GPa, their low tensile ductility (<5%) renders them unsuitable for structural applications. That the amorphous 13.6 at.%-Mn alloy exhibits low ductility is in line with catastrophic failure commonly observed in amorphous alloys and bulk metallic glasses, where shear band formation followed by rapid shear band propagation leads to macroscopic failure. Thus, it is also likely that the brittle amorphous phase in the nanostructured 8.2 at.%-Mn contributes to its low toughness. As shown in Figures 2.4(b) and 2.6, this two-phase alloy exhibits a bimodal grain size distribution centered at ~40 and ~4 nm. Since nano-grains that are less than ~10 nm are considered incapable of dislocation pinning and accumulation [7, 8]; it is also plausible that these extremely fine grains impair the alloy's ability to deform plastically. Additionally, inhomogeneous phase distribution, as evidenced by the characteristic domain-network structures in Figure 2.4(b), may also affect ductility.

## ***2.4. Conclusions***

We have presented a detailed microstructural study of Al-Mn alloys electrodeposited from an ionic liquid at room temperature. Additionally, we have provided the first measurements of hardness in Al-Mn electrodeposits across a broad range of structural conditions. Three structural regimes, defined by the alloy Mn content, are identified:

(a) 0 to 7.5 at.% Mn: These alloys are microcrystalline FCC solid solutions exhibiting rough angular surface morphologies. As the Mn content increases over this range, the grain size decreases from 15 to 7  $\mu\text{m}$  due to kinetic effects on deposition, and the hardness increases from about 1.0 to 2.8 GPa.

(b) 8.2 to 12.3 at.% Mn: These deposits have a smooth, nodular surface structure, and comprise nanometer-scale crystals of the FCC solid solution phase coexisting with an amorphous phase. The amorphous phase is Mn-enriched, and its volume fraction increases with the global Mn content. The phases are arranged as domains of one phase embedded in a network or matrix of the other; the characteristic radius of the domains is about 10-25 nm, which is consistent with the surface diffusion length during electrodeposition. These alloys exhibit a local peak in hardness of 5.2 GPa at 8.2 at.%, where the FCC phase is the majority phase.

(c) 13.6 to 15.8 at.% Mn: These alloys exhibit a single amorphous phase, whose hardness increases from 4.8 to 5.5 GPa as Mn content rises. For the first time, we confirm that this apparently amorphous phase contains pre-existing nano-quasicrystalline nuclei in the as-deposited state; these nuclei grow into nano-quasicrystals at about 300°C.

The observation of nano-quasicrystalline nuclei in the amorphous alloys unifies prior reports in the literature, where deposition at temperatures above 300° C directly yields the quasicrystalline phase, while deposition at lower temperatures leads to an amorphous phase. These experimental results are in line with those obtained from our theoretical model in Appendix A, where low deposition temperatures promote nano-scale roughness and increase the stability of surface nuclei, thus resulting in structural refinement.

Even though the nanostructured and amorphous alloys exhibit impressive hardness, they exhibit extremely low tensile ductility. Their brittleness is likely due to nanocrystalline grain sizes (<10 nm) that are incapable of the usual dislocation activities, inhomogeneous phase distribution, as well as rapid shear band propagation that leads to catastrophic failure in the amorphous phase.

### **3. Tailoring the grain size and phase distribution of electrodeposited Al-Mn alloys to achieve high hardness and toughness<sup>2</sup>**

As described in the chapter 2, Mn effectively promotes nanostructure formation in electrodeposited Al-Mn alloys and the nanostructured and amorphous alloys exhibit impressive hardness. Unfortunately, structure refinement into the nanometer regime occurs concomitantly with the appearance of a brittle amorphous phase. Additionally, the nanocrystalline phase of these duplex alloys contains a large fraction of grains that are less than ~10 nm and incapable of dislocation pinning and accumulation. Inhomogeneous phase distribution in these alloys likely induces brittle failure as well. Therefore, synthesis of Al alloys with high hardness and toughness relies on the ability to tailor both the grain size and phase distribution of Al-Mn alloys.

Results obtained in chapter 2 indicate that microstructural features of electrodeposited Al-Mn alloys appear principally governed by nucleation kinetics at the electrode. Progressive grain refinement with increasing Mn content of the microcrystalline FCC phase is postulated to be controlled by nucleation kinetics at the electrode and phase distribution of the duplex structures is plausibly related to adatom surface diffusion during electrodeposition. Since the characteristic length of the domain-network structures observed in the dual-phase alloys is probably related to the characteristic diffusion length of an adatom on the film surface (see section 2.3.3 and Figure 2.4), it is likely that the shape of the applied current waveform would affect the extent of phase segregation.

Various current waveforms that each comprise two unique pulses, as shown in Figures 1.4(b)-(d), were used to deposit alloys with ~8 at.% Mn content; details of these experiments and the results obtained are described in Appendix B and [129]. The parameters of the first cathodic pulse were kept the same for all waveforms; the current density was set at 6 mA /cm<sup>2</sup>, which was the cathodic current density of the direct-current waveform used in chapter 2; the pulse duration was fixed at 20 ms. As discussed in

---

<sup>2</sup> Much of the content of this chapter has been submitted in a patent application [129]



section 2.3.3, for an applied current density of  $6 \text{ mA /cm}^2$ , the time required for monolayer coverage is  $\sim 200 \text{ ms}$ . The cathodic pulse duration was chosen to be  $1/10^{\text{th}}$  this time interval (i.e.  $20 \text{ ms}$ ), to reduce the extent of phase segregation before the application of the next pulse. One of the waveforms that yielded the best results comprises, in addition to the cathodic pulse described above, an anodic pulse with pulse duration of  $20 \text{ ms}$  and anodic current density of  $3 \text{ mA/ cm}^2$ . This reverse-pulse waveform was selected to deposit films of different compositions to systematically analyze their structures and properties.

Herein, alloys deposited with the selected reverse-pulse waveform will be called the “RP” alloys; those produced by the conventional current waveform, as described in the previous chapter, will be named the “DC” alloys. In this chapter, the composition and microstructure of the RP alloys are analyzed using SEM/EDX, XRD and TEM. Particular emphasis is placed on the effects of reverse pulsing on the characteristic grain size, grain size distribution, as well as phase distribution. The hardness and toughness of these alloys are then assessed. The effects of reverse-pulsing on the structures and properties of alloys electrodeposited in a non-aqueous medium are thus studied for the first time. .

### ***3.1. Experimental procedures***

The chloroaluminate ionic liquid used to electrodeposit our RP Al-Mn alloys was prepared using the same procedures detailed in section 2.1 and ref. [103]. The current waveform comprises a cathodic and anodic pulse, as illustrated in Figure 1.4(d), where both pulse durations were  $20 \text{ ms}$  and the cathodic and anodic current densities were  $6$  and  $3 \text{ mA /cm}^2$ , respectively. Alloys with different Mn contents were obtained by controlled additions of anhydrous manganese chloride to the electrolytic baths. Electrodeposition experiments were carried out at room temperature until film thicknesses of  $\sim 10 \text{ }\mu\text{m}$  were obtained. Alloy chemical composition was measured using SEM/EDX; phase composition was determined with XRD; grain size and phase distributions were examined in the TEM. These procedures are identical to those described in section 2.1 and ref. [103].

Using the results obtained from our microstructural analysis, three RP alloys with unique phase contents (and hence, solute contents) were selected for mechanical testing. To measure hardness, micro-indentation tests were carried out using a load of 5 grams and a holding time of 15 seconds. The indentation depth was in all cases significantly less than  $1/10^{\text{th}}$  the film thickness, ensuring a clean bulk measurement. Each reported data point represents an average of at least 8 indentations. To assess tensile ductility, guided bend tests following ASTM E290-97a (2004) were performed, as described in section 2.1. For each of the three unique alloys, multiple samples were subjected to different amounts of tensile strain during the guided bend tests. After the bent tests, the convex bent surfaces were examined for cracks and fissures using the SEM. The reported ductility value for each alloy corresponds to the largest applied strain at which no cracks or fissures were observed on the bent film.

For samples that did not exhibit any cracks after the bend test, their copper substrates were dissolved in concentrated nitric acid. Both the bent portions of the Al-Mn films, as well as the regions that were far from the bend, were jet-polished for post-mortem TEM analysis. Because samples that failed during the bend tests exhibited cracks that were narrow, the fracture surfaces were not sufficiently exposed for microscopic analysis. Thus, an Instron machine was used to fracture fresh specimens (film and substrate together) in tension. The fracture surfaces were analyzed in the JEOL 6700 SEM at 5 kV and the back-scattered detector was used to distinguish between the film and copper substrate.

### ***3.2. Microstructure characterization***

In this section, we present characterization results on all of the RP alloys prepared in this study and compare the alloy microstructure to that of the DC alloys.

#### ***3.2.1. Alloy composition***

RP alloys with Mn contents between 0 and 13.8 at.% were synthesized in this study. Figure 3.1 compares the relationship between electrolyte composition and alloy composition for experiments conducted with the DC and RP waveforms. For electrolytes that contained up to  $\sim 0.08$  mol/L  $\text{MnCl}_2$ , the applied current waveform had negligible

effects on the alloy composition. However, for electrolyte compositions between  $\sim 0.08$  and  $\sim 0.17$  mol/L  $\text{MnCl}_2$ , the as-deposited RP alloys exhibited lower Mn contents. Thus, Figure 3.1 indicates that within this range of electrolyte composition, the anodic pulse preferentially removes Mn from the as-deposited alloy. Interestingly, as shown in Figure 3.1, the corresponding alloy compositions lie between  $\sim 8$  and  $\sim 14$  at.%-Mn. Recall that for the DC alloys, Mn content of  $\sim 8$  at.% corresponds to the onset of a duplex structure, where nanocrystalline grains co-exists with an amorphous phase, and  $\sim 14$  at.% coincides with the disappearance of the crystalline phase (see Figures 2.2 and 2.4). Therefore, the results presented in Figure 3.1 provide hints that reverse-pulsing exerts an interesting effect on the dual-phase alloys. In what follows, we will focus on the effects of reverse-pulsing on the alloy microstructure.

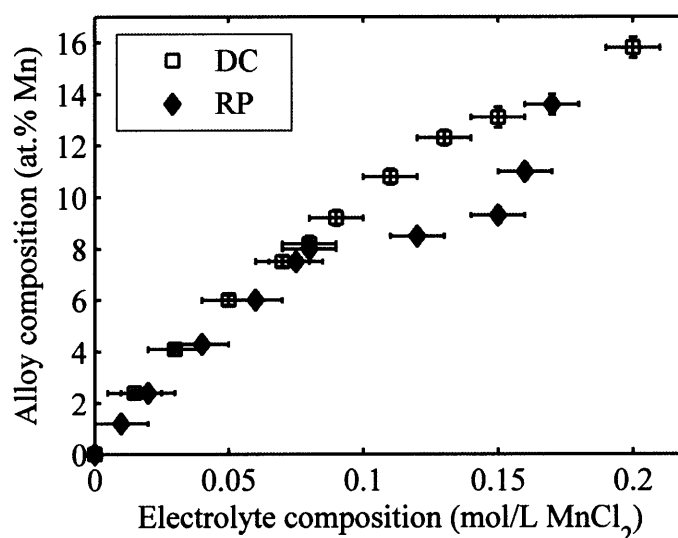


**Figure 3.1** Plot showing the effects of current waveform on alloy composition at different electrolyte compositions.

### 3.2.2. Phase content

Figure 3.2 shows X-ray diffractograms of the RP alloys. At low Mn content, the alloys exhibit a FCC  $\text{Al(Mn)}$  solid solution phase; at intermediate Mn content between 8.0 and 10.4 at.%, an amorphous phase, which exhibits a broad halo in the diffraction pattern at  $\sim 42^\circ 2\theta$ , co-exists with the FCC phase; at high Mn content above 11 at.%, the alloys contain a single amorphous phase.

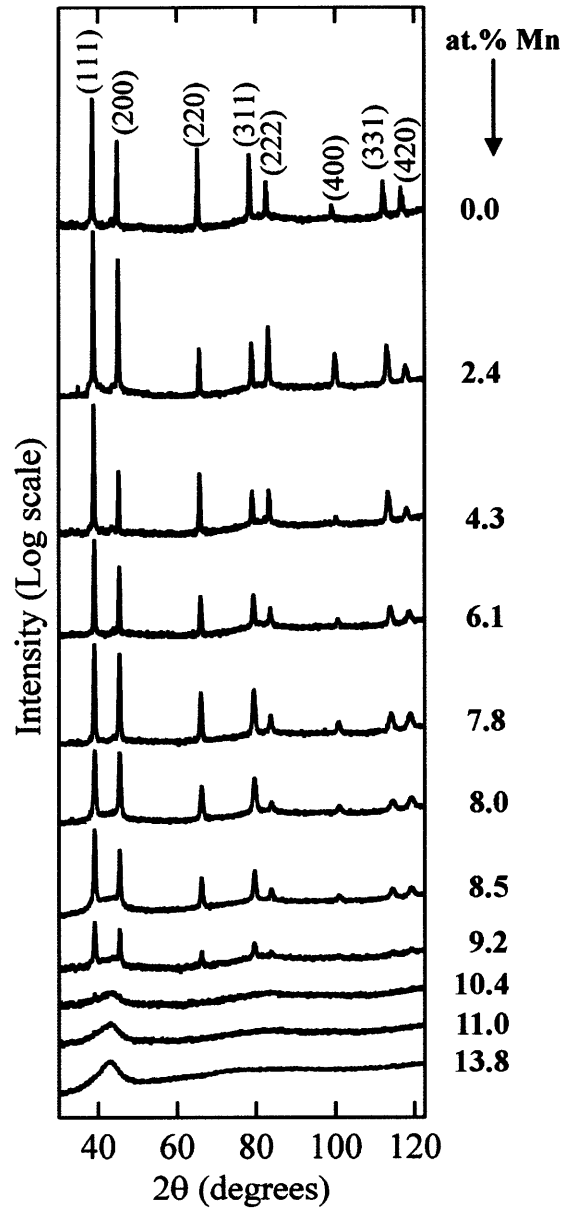


**Figure 3.2** X-ray diffractograms of as-deposited RP Al-Mn alloys, the compositions of which are shown at the right. Locations of the FCC Al(Mn) reflections are shown at the top. Note also the emergence of a broad amorphous halo at  $\sim 42^\circ 2\theta$  for compositions above 8.0 at.%.

Figure 3.3 compares the percent contribution of FCC peaks to the total integrated intensities observed in the XRD patterns for the DC and RP alloys. Even though both DC and RP alloys transition from a single FCC phase to a duplex structure at about the same composition of  $\sim 8$  at.% Mn, the composition range over which the alloys exhibit a two-phase structure is narrower for the RP alloys (between 8.0 and 10.4 at.% Mn) than that of the DC ones (between 8.2 and 12.3 at.% Mn). The XRD results presented in Figure 3.2 suggest that reverse-pulsing alters the phase content of the alloys. The grain

size distribution and phase distribution in the RP alloys will be examined in the following section.

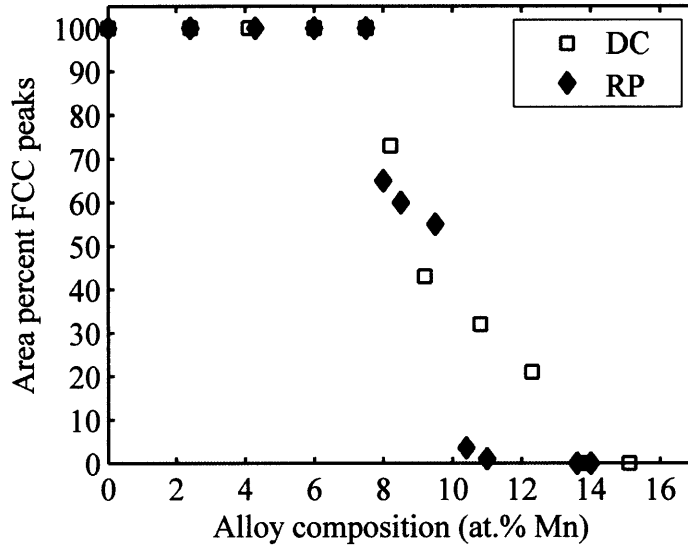


**Figure 3.3** Percent contribution of FCC peaks to the total integrated intensities observed in X-ray diffractograms, as shown in Figure 2.2 for the DC alloys and Figure 3.2 for the RP alloys.

### 3.2.3. Grain size and phase distribution

Figure 3.4 shows the TEM images along with the electron diffraction patterns of the RP alloys. The phase contents, as inferred from the electron diffraction patterns in Figure 3.4, are consistent with the XRD results shown in Figure 3.2 – alloys with up to 7.8 at.%-Mn comprise a single FCC phase; alloys with Mn contents between 8.2 and 10.4 at.% contain an amorphous phase co-existing with the FCC phase, as evidenced by the diffuse halo between the (111) and (200) FCC rings; alloys with more than 11 at.%-Mn consist of a single amorphous phase.

Figures 3.4(a) and (b) indicate that when the Mn content increases from 0 to 6.1 at.%, the average grain size decreases from ~2.5 to ~1  $\mu\text{m}$ . Interestingly, alloys with 7.0 and 7.8 at.% Mn contents exhibit nanometer-sized grains, with averages of ~500 and ~160 nm, respectively (see Figures 3.4(c)- (d)). Further increase in Mn contents from 8.2 to 10.4 at.% causes the average grain size to decrease from ~37 nm to ~5 nm.

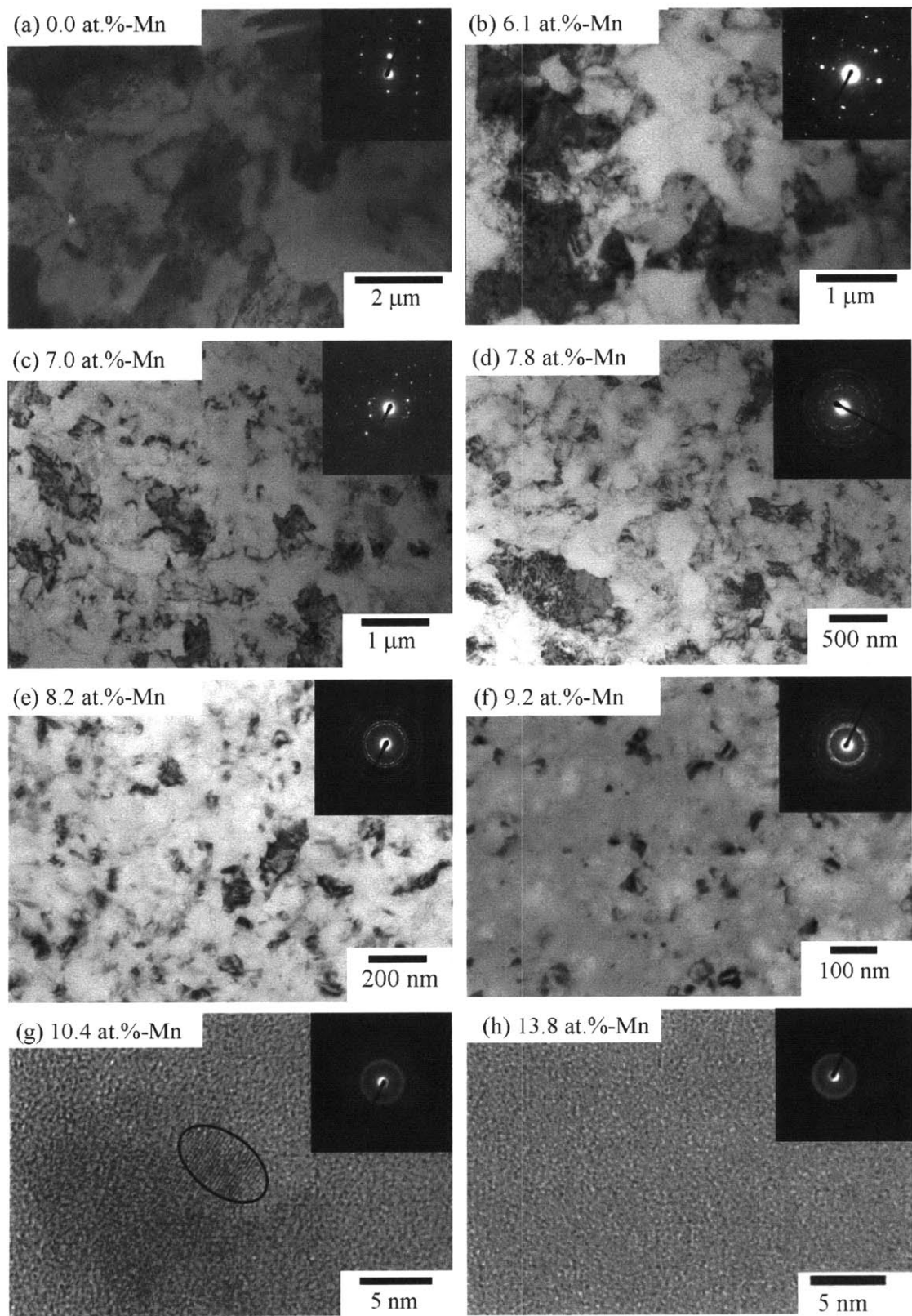


**Figure 3.4** Bright-field TEM images and electron diffraction patterns of the RP alloys. Note the single phase nanocrystalline structures in (c)-(d). Images (e)-(g) shows that the two-phase alloys no longer comprise the domain-network structures observed in the DC alloys in Figure 2.4.

The relationships between solute content and crystalline grain size for both the DC and RP alloys are illustrated in Figure 3.5(a), where the region shaded gray corresponds to the composition range where the alloys exhibit a single crystalline phase. Whereas the DC alloys show an abrupt microcrystalline-to-nanocrystalline transition upon the appearance of an amorphous phase at ~8 at.-%Mn, the grain size of the RP alloys gradually transitions from microns to nanometers at ~7 at.-%Mn, before an amorphous phase emerges at ~8 at.-%Mn. Thus, Figures 3.4(c)-(d) and 3.5(a) underscore that with the use of a reverse-pulsed waveform, nanocrystalline grain sizes can be achieved in single phase Al-Mn electrodeposits.

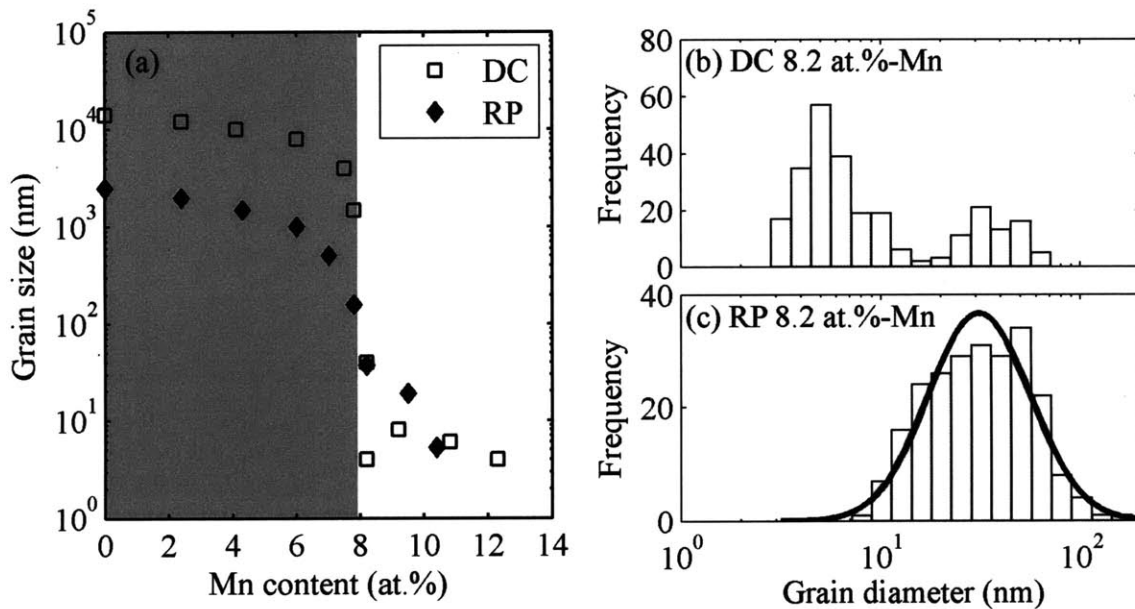


**Figure 3.5 (a) Average grain sizes of DC and RP alloys at different Mn compositions. Region shaded gray represents the composition range within which both the RP and DC alloys contain a single FCC phase. The grain size distribution of ~250 grains observed in the 8.2 at.-%Mn alloys are shown in (b) for the DC alloy and (c) for the RP alloy. Also shown in (c) is a lognormal distribution curve.**

The grain size distribution of ~250 grains observed in the DC and RP alloys containing 8.2 at.-%Mn are shown in Figures 3.5(b) and (c), respectively. The thick solid line in Figure 3.5(c) represents a lognormal distribution curve. In contrast to the DC alloy, which exhibits a bimodal grain size distribution centered at ~40 and ~4 nm, that of the RP alloy concurs well with the lognormal distribution, with an average grain size of ~37 nm. In addition to changing the grain size distribution, the TEM images presented in Figures 3.4(e)-(h) show the duplex RP alloys do not exhibit the characteristic domain-

network structure that was observed in the DC alloys (cf. Figures 3.4(b)-(e)). Instead, the FCC grains appear uniformly dispersed and the amorphous phase is assumed to be distributed in the intergranular regions.

The results presented in this section shows that the use of a reverse-pulsed waveform effectively allows us to (a) synthesize single phase nanocrystalline Al-Mn alloys, (b) alter the grain size distribution and (c) homogenize the phase distribution in duplex Al-Mn alloys.

### 3.3. *Mechanical properties*

Based on the results presented in the previous section, the RP alloys exhibit three distinct phase compositions: a single FCC phase, an FCC phase co-existing with an amorphous phase and a single amorphous phase. One alloy is selected from each of these phase regimes for mechanical testing. The solute compositions, phase contents and crystalline grain sizes of these alloys are summarized in Table 3.1.

**Table 3.1 Solute contents of the three RP alloys selected for mechanical testing are listed on the top row. Also shown are the phase composition, FCC grain size, micro-hardness and tensile elongation at fracture of each alloy.**

	Alloy composition (at.%-Mn)		
	7.8	8.2	13.8
Phase content	FCC	FCC + amorphous	amorphous
FCC grain size (nm)	159	37	-
Microhardness (GPa)	3.0	3.4	4.5
Tensile elongation (%)	>37	13	5

#### 3.3.1. *Micro-hardness*

Results of our micro-indentation tests are tabulated in Table 3.1. That the 7.8 at.%-Mn alloy exhibits a high hardness of ~3.0 GPa is likely due to solid solution strengthening effects and its nanocrystalline grain size. Further increase in Mn content and reduction in grain size causes the hardness of the 8.2 at.%-Mn alloy to increase to ~3.4 GPa. The 13.8 at.%-Mn amorphous sample exhibits the highest hardness of ~4.5 GPa. Even though the role of solute on the strength/hardness of amorphous phases is not well understood, the negative heat of mixing between Al and Mn indicates that Mn



additions increase the average bond strength in the alloy, which would promote higher hardness.

### 3.3.2. Tensile ductility

SEM images of the Al-Mn films that were subject to ~37% tensile strain during the guided bend tests are presented in Figure 3.6. Low-magnification images of the entire bent surfaces are shown on the left column; images on the right correspond to higher magnification images of the bent regions.

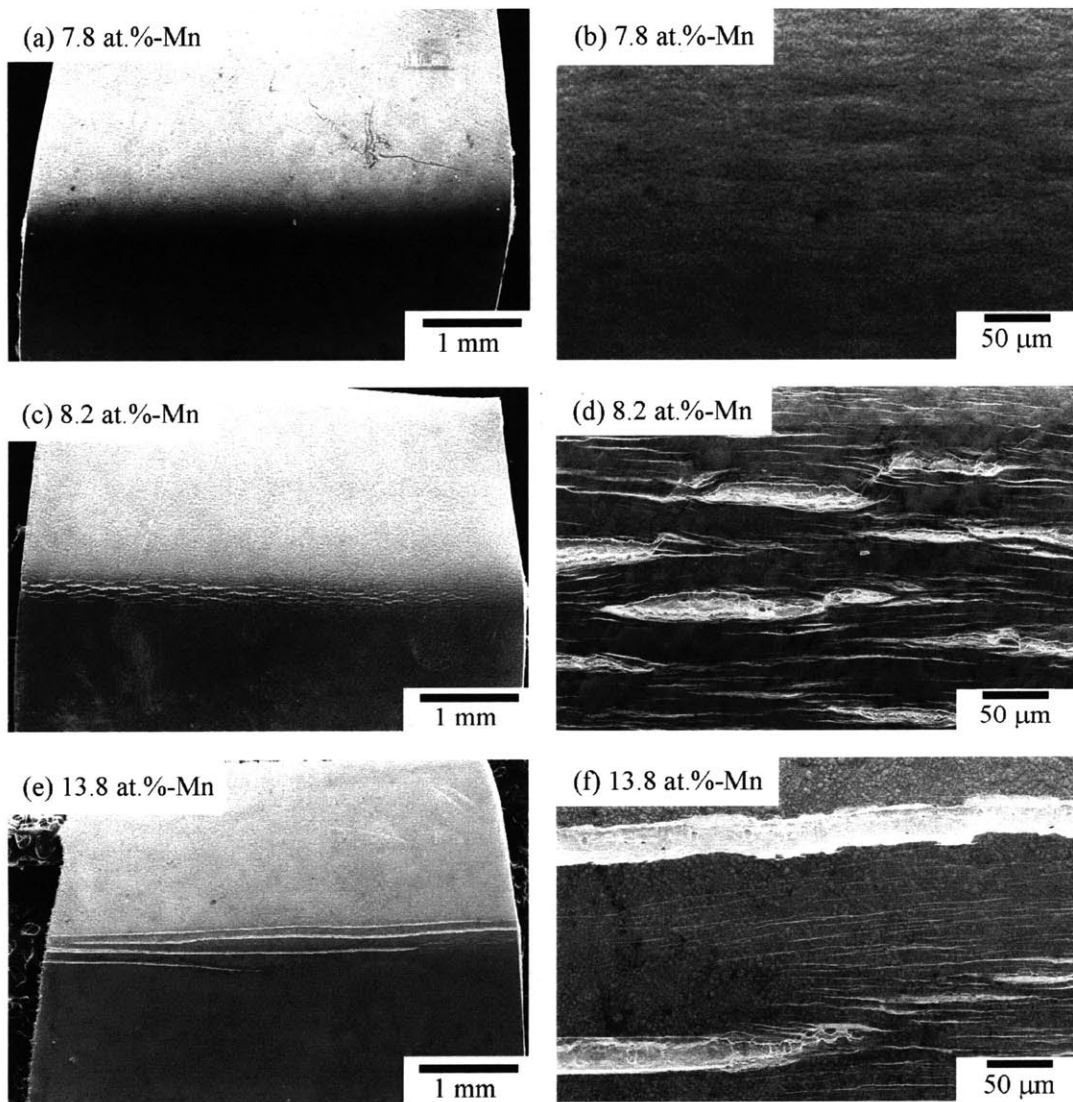


**Figure 3.6** SEM images of the entire bent surfaces of films that were subject to ~37% tensile strain are shown on the left column. Corresponding higher magnification images of the bent regions are presented on the right.

Figures 3.6(a)-(b) show that the 7.8 at.-%-Mn specimen remained crack-free, thus indicating that its ductility exceeds 37%. On the other hand, the same level of strain resulted in micron-sized fissures with topologically rough edges in the 8.2 at.-%-Mn alloy, as shown in Figures 3.6(c)-(d). The extent of cracking increased further in the amorphous 13.8 at.-%-Mn film (Figures 3.6(e)-(f)), where cracks initiated at the sample edge and terminated slightly more than halfway across the sample width. Even though Figures 3.6(c)-(f) indicate that the 8.2 and 13.8 at.-%-Mn specimens exhibit lower ductility than their single phase nanocrystalline counterpart, their abilities to resist crack propagation, together with the jagged crack edges point to some degree of toughness. Reduction of the applied strain to ~13% and ~5% during the bend tests resulted in fissure-free surfaces for the 8.2 and 13.8 at.-%-Mn specimens, respectively. The tensile elongations at fracture of these alloys are listed in Table 3.1.

### 3.3.3. *Fractography*

The fracture surfaces of the 7.8 and 8.2 at.-%-Mn films are presented in Figures 3.7(a)-(b) and (c)-(d), respectively, where higher magnification images are shown on the right column. In these images, black solid lines are used to demarcate the Al-Mn film and copper substrate; the tensile axis points out of the page. Chisel-type or knife-edge fracture is observed in both samples; such fracture surfaces, which are more aptly called “rupture surfaces” since the corresponding reduction in area is almost 100%, occur when failure is delayed until a high degree of necking has occurred, i.e. they are commonly observed in metals and alloys that exhibit high ductility [130-137]. Upon necking, zones of localized shear develop and rupture occurs when two opposing diagonal shear zones cross through the center of the neck [131, 133, 136]. It is proposed that chisel-type fracture is an alternative fracture mode to “cup-and-cone” fracture in ductile materials when void development and coalescence are suppressed [130, 131]. Thus, the chisel-edges observed in Figures 3.7(a)-(d) provide corroborating evidence of non-negligible toughness in these nanostructured alloys.

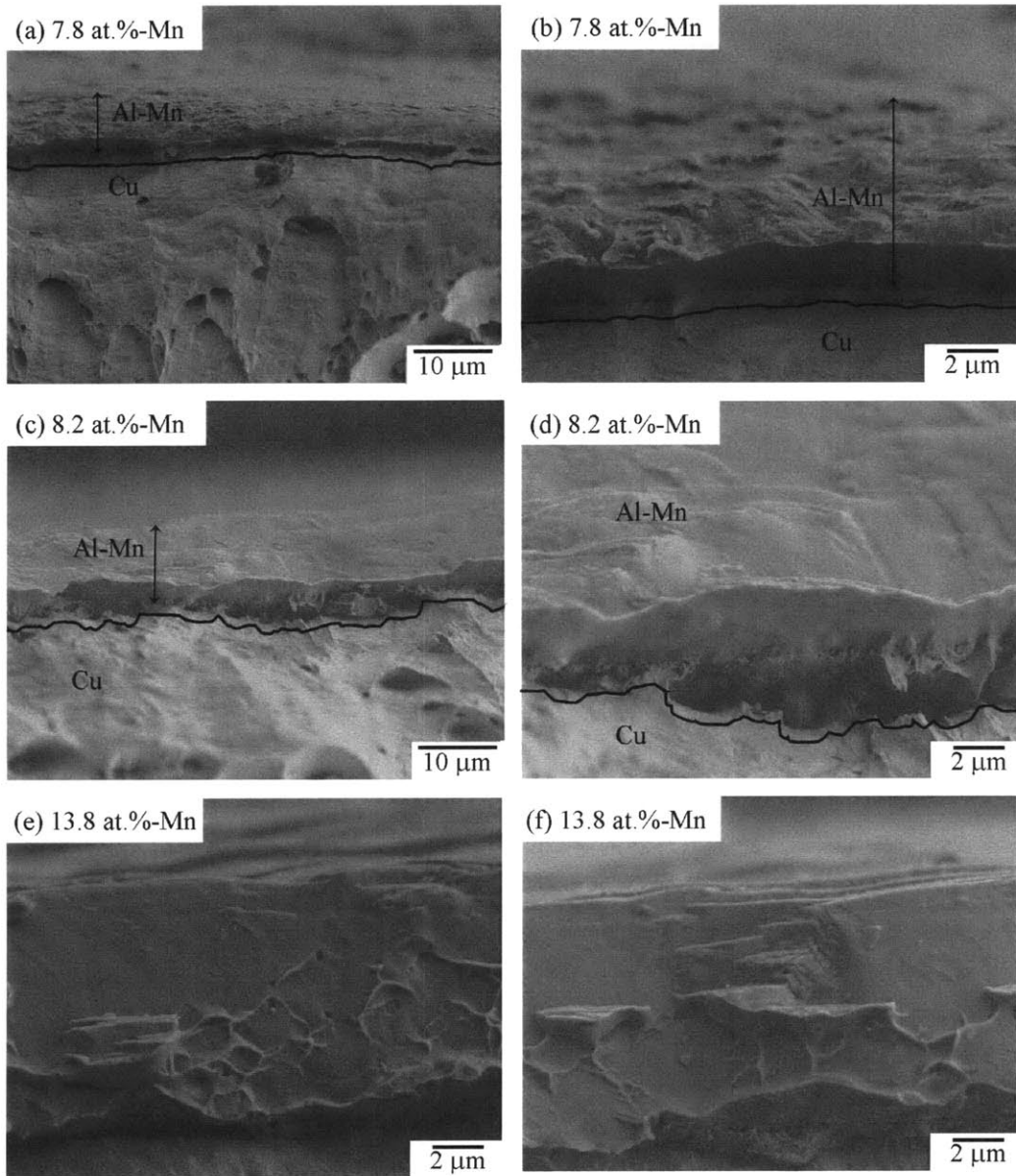


**Figure 3.7** SEM images of the fracture surfaces of films containing (a)-(b) 7.8, (c)-(d) 8.2 and (e)-(f) 13.8 at.%-Mn. In images (a)-(d), the solid black lines demarcate the Al-Mn film and its copper substrate and the double-headed arrows are used to roughly approximate the film thickness in the trailing regions of the fracture.

The double-headed arrows in Figures 3.7(a)-(c) represent rough approximations of the film thicknesses at the trailing regions of the rupture. The values are  $\sim 6$ - $7$  and  $\sim 9$ - $10$   $\mu\text{m}$  for the 7.8 and 8.2 at.%-Mn films, respectively. Even though these values do not reflect the exact film thickness prior to fracture, similar measurements along other regions of the fracture surfaces consistently yielded values that are less than  $\sim 7$   $\mu\text{m}$  for the 7.8 at.%-Mn film while those for the 8.2 at.%-Mn are  $\sim 9$   $\mu\text{m}$ . Since the as-deposited

film thickness was  $\sim 10\ \mu\text{m}$  for both alloys, it is reasonable to deduce that the 7.8 at.-%-Mn alloy fractured after necking down more extensively than the 8.2 at.-%-Mn film. This explanation is consistent with the higher tensile ductility observed in the 7.8 at.-%-Mn alloy (see Table 3.1).

Figures 3.7(e)-(f) illustrate different features observed along the fracture surface of the amorphous 13.8 at.-%-Mn film; these images were obtained from different regions. Both images show that the fracture surface is inclined at an angle to the plane normal to the tensile axis, which is consistent with catastrophic failure due to shear-banding—a deformation mechanism commonly observed in amorphous alloys and metallic glasses. In contrast to a simple shear-off appearance observed in brittle alloys, the fracture surfaces in these images appear rough. The vein-like patterns in Figure 3.7(e) reflect local viscous flow and indicate some amount of plastic flow is involved in fracture [138-140]. Additionally, step-like relief in Figure 3.7(f) could be related to multiple shear bands operating at once, which has been associated with enhanced malleability since the microscopic strain is the sum contribution of local strain from every shear band [141, 142].

The results presented in Figure 3.7 provide corroborating evidence that legitimate plastic flow can occur in these nanostructured and amorphous alloys, and also qualitatively illustrate the decreasing trend in toughness as solute content and amorphous phase fraction increase.

#### **3.3.4. *Post-mortem TEM***

Post-mortem TEM images of a 7.8 at.-%-Mn film that sustained a tensile strain of  $\sim 37\%$  without cracking are shown in Figure 3.8(a)-(b), where (a) corresponds to a region far away from the bend and (b) corresponds to a strained/bent region. This specimen is single phase FCC, and has a grain size of  $\sim 159\ \text{nm}$ . Comparison of both images reveals higher dislocation density within the grains of the deformed region, possibly due to dislocation nucleation and emission from grain boundaries and dislocation entanglement during deformation [143]; these results are consistent with the notion that nanocrystalline grain sizes above  $\sim 100\ \text{nm}$  are capable of normal dislocation activity [7, 8].

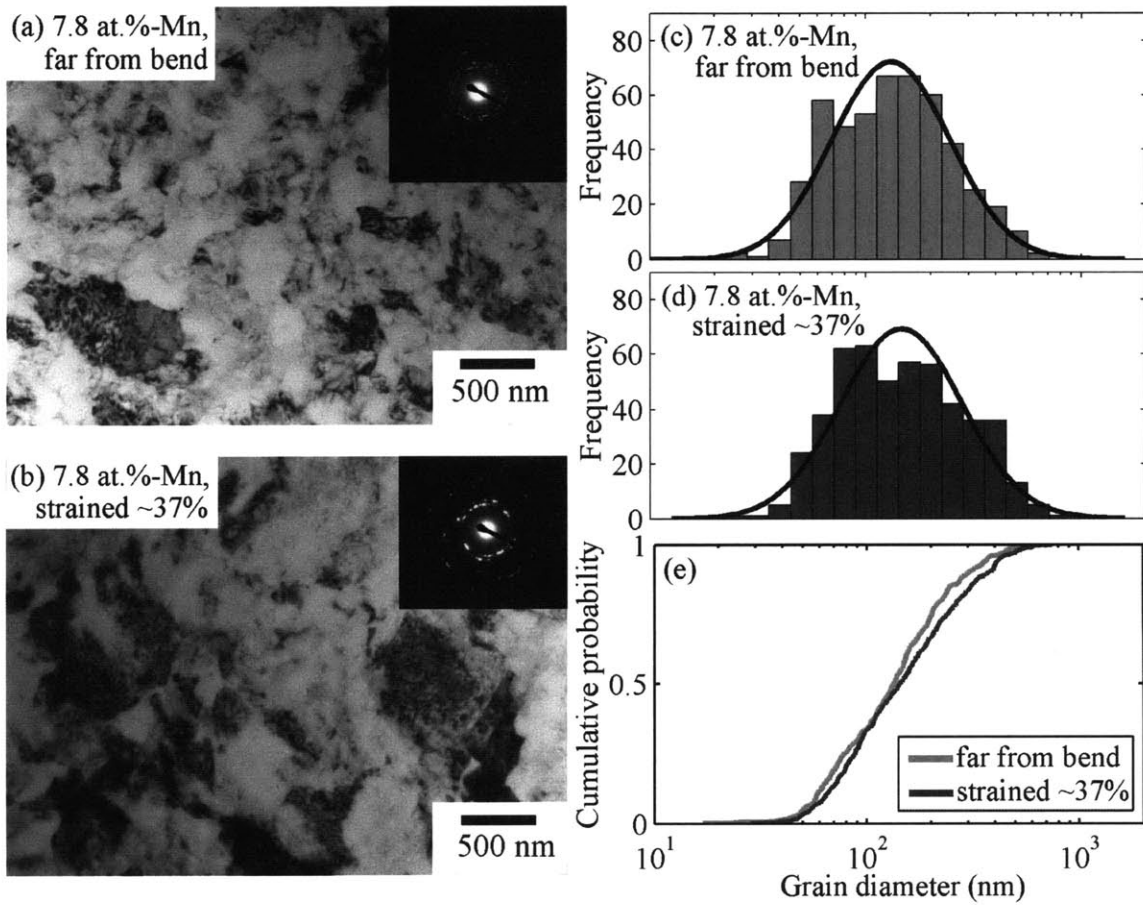


**Figure 3.8** TEM image in (a) belongs to a region far from the bend; image (b) corresponds to a bent region where the applied tensile strain is ~37%. The corresponding grain size distributions are shown in (c) and (d), along with the lognormal distribution curves. The cumulative grain size distribution plots of both regions are illustrated in (e).

A comparison of the bright-field images in Figure 3.8(a) and (b) also hints of coarser grains in the strained region. The corresponding electron diffraction pattern in Figure 3.8(b) comprises bigger and more discrete spots than that of the as-deposited sample (Figure 3.8(a)), also suggesting the possibility of some deformation-induced grain coarsening. The grain size distributions in the un-deformed and strained regions are plotted in Figures 3.8(c) and (d), respectively, along with the corresponding lognormal distributions, which are represented by thick solid curves. Grain sizes were measured on more than 400 grains in each region. In the un-deformed region, the grain size distribution concurs rather well with the lognormal distribution (Figure 3.8(c)). The grain size distribution of the deformed region, as shown in Figure 3.8(d), exhibits greater deviation from lognormal. More specifically, grain sizes between ~70 and 90 nm, as well as ~300 and 400 nm, are observed more frequently than expected for a lognormal

distribution. The cumulative grain size distributions in both regions are presented in Figure 3.8(e), where grain sizes in the strained region are evidently larger than in the undeformed region. Our post-mortem analysis indicates that upon deformation, the average grain size increased from 159 to 184 nm. Deformation-induced grain growth could be facilitated by grain sliding, which brings grains of similar orientation into close contact [143], or by grain rotation, which causes neighboring grains to coalesce [144, 145], or by stress-assisted grain-boundary migration [146]. That a 16% increase in grain size is insufficient to account for the 37% applied tensile strain shows that both dislocation activities and grain boundary mediated deformation mechanisms, such as deformation-induced grain coalescence, contribute to the high toughness of the 7.8 at.-%Mn alloy.

Based on the above discussion, we expect that the 8.2 at.-%Mn alloy exhibits lower toughness because it comprises smaller nano-grains (~37 nm) that are less capable of dislocation storage and accumulation. Also, this specimen is dual-phase, and we believe that the amorphous phase is located in the intergranular regions; this would tend to inhibit grain growth and coalescence by conventional mechanisms. Consequently, statistically significant changes in the grain size distribution were not observed from our post-mortem TEM images, as shown in Figure 3.9.

Post-mortem TEM analysis of the 13.8 at.-%Mn sample revealed that an amorphous phase prevailed at the deformed region; thus, ruling out the possibility of deformation-induced crystallization.

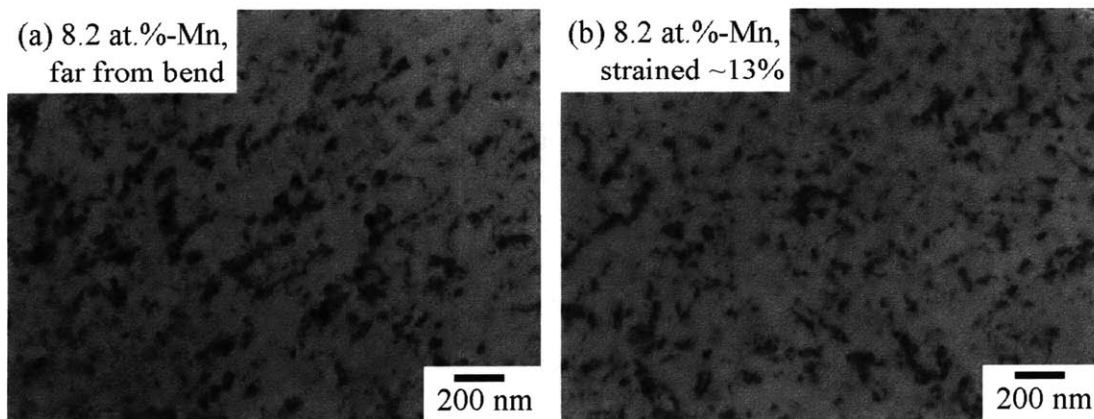


**Figure 3.9** TEM images of a 8.2 at.-%Mn sample; image (a) belongs to a region far from the bend; image (b) corresponds to a bent region where the applied tensile strain is ~13%.



### 3.3.5. Hardness vs. toughness

Figure 3.10(a) compiles the hardness and ductility of our alloys. The solid red diamonds denote alloys that did not exhibit any crack or fissure after the guided bend tests while the white diamonds outlined in red represent alloys that cracked. Also shown in the plot are the corresponding values for commercial Al alloys and structural steels. The hardness,  $H$ , of some Al- alloys are approximated from their reported yield stress,  $\sigma_y$ , by using Tabor relation, i.e.  $H \approx 3 \sigma_y$ . Figure 3.10(a) shows that our alloys exhibit high hardness and toughness that not only outperform other Al alloys, but are also comparable to structural steels. Because our alloys weigh three times less than steels, a remarkable combination of high specific hardness and tensile elongation is achieved, as shown in Figure 3.10(b).

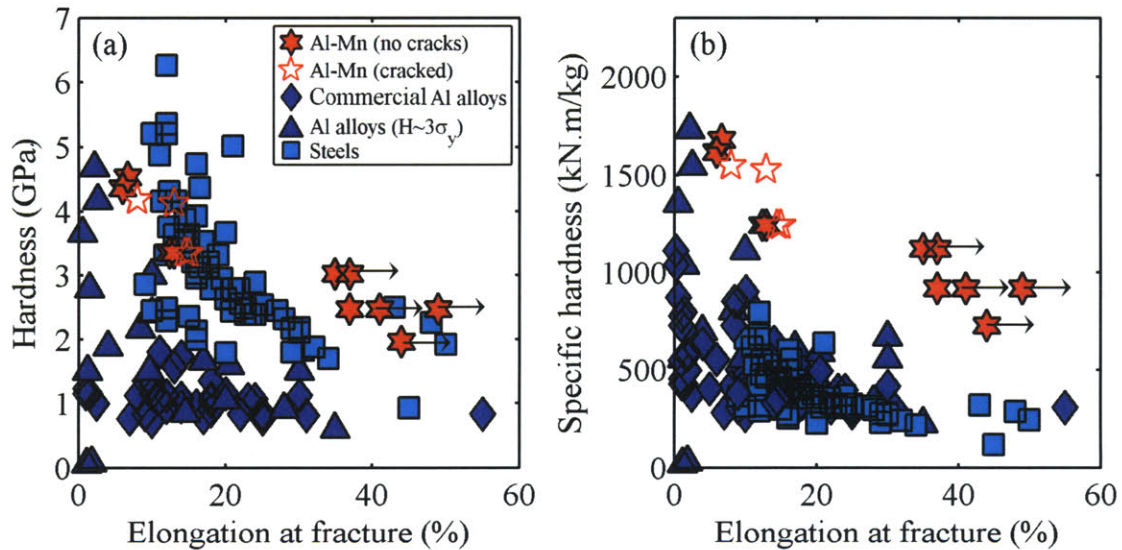


Figure 3.10 Ashby plot showing (a) hardness and (b) specific hardness vs. tensile elongation at fracture of our electrodeposited Al-Mn alloys. Samples that did not exhibit any crack after the guided bend test are represented by solid red hexagons. The solid black arrows pointing to the right of these hexagons indicate that the ductility of these samples exceeds the values represented by the data points. Samples that failed, i.e. exhibited fissures or cracks of any length and width, are denoted by pentagons outlined in red. Also shown in this plot are the properties of commercial Al-based alloys, as well as structural steels.

The toughness exhibited by our nanocrystalline and nanostructured alloys outperforms many electrodeposited nanocrystalline metals and alloys. In contrast to common methods that are used to electrodeposit nanocrystalline metals and alloys, such as by adding organic additives into the electrolytic bath to promote grain nucleation, the

technique employed here does not introduce additional impurities into the deposits. In fact, experimental evidence of nanocrystalline metals and alloys with low impurity contents that are produced by severe plastic deformation also suggests that such materials can exhibit high ductility and that the low tensile ductility observed in other studies could be related to contaminants [5, 6].

Therefore, the combination of high hardness and toughness reported in this study is mainly attributed to our ability to (a) synthesize single-phase nanocrystalline grains without using organic additives and (b) create uni-modal grain size distribution and homogeneous phase distribution in nanocrystalline/amorphous duplex alloys through the application of a reverse-pulsed current waveform.

### ***3.4. Conclusions***

With an eye to achieve high hardness and toughness in electrodeposited Al-Mn alloys, we employ a reverse-pulse current waveform to tailor the characteristic grain size, grain size distribution, as well as phase distribution of the alloys. In this study, alloys with Mn contents between 0 and 13.8 at.% were synthesized. Between 0 and ~7.8 at.%-Mn, the alloys comprise a single FCC solid solution phase; between ~8.0 and ~10.4 at.%-Mn, the FCC phase co-exists with an amorphous phase; above 11.0 at.%-Mn, a single amorphous phase dominates. Unlike Al-Mn alloys electrodeposited with conventional DC current, the following microstructures were achieved:

- Single phase nanocrystalline grains.
- Uni-modal nanocrystalline grain size distribution.
- Homogeneous phase distribution.

As a result of the fine microstructural length-scales and structural homogeneity, these alloys were found to exhibit an impressive combination of hardness and toughness:

- The single phase 7.8 at.%-Mn alloy exhibits a high micro-hardness of ~3.0 GPa because of its nanocrystalline grain size (~159 nm) and solid-solution strengthening. Activation of grain boundary mediated deformation mechanisms, such as grain growth, in addition to dislocation-mediated plasticity result in an impressive ductility of >37%.



- The 8.2 at.%-Mn two-phase alloy exhibits finer nanocrystalline grains (~37 nm) and thus, higher micro-hardness of ~3.4 GPa. Because of its unimodal grain size distribution, low fraction of grains that are less than ~10 nm and homogeneous phase distribution, its elongation at fracture reaches a respectable value of ~13%. It is likely that the amorphous phase inhibits grain boundary-mediated deformation mechanisms, thus resulting in lower toughness than its single phase nanocrystalline counterpart.
- The 13.8 at.%-Mn amorphous alloy exhibits the highest hardness of ~4.5 GPa. Because of shear band formation and rapid shear band propagation, its ductility value is only ~5%. That some degree of toughness is observed in this amorphous alloy can be attributed to multiple shear band formation.

This work highlights the use of reverse-pulsing to tailor the microstructure of multi-phase electrodeposits and underscores that high hardness and toughness can be simultaneously achieved in nanocrystalline, nanostructured and amorphous alloys.

## **4. An atom probe investigation of weak solute partitioning in nanocrystalline and amorphous phases of Al-Mn<sup>3</sup>**

Because of homogeneous phase distribution and very fine microstructural length-scales (<40 nm) in the dual-phase RP alloys, traditional techniques like STEM and EDX in the TEM are inadequate to probe solute partitioning between the different phases of these alloys. Three-dimensional atom probe tomography (APT), on the other hand, offers atomic-level resolution. In this chapter, we employ APT to characterize our nanostructured and amorphous RP alloys. Using single phase alloys as baselines for comparison, we specifically aim to understand the solute distribution in a two-phase nanocrystal/amorphous alloy, where the solute is only weakly partitioned between the two phases, which are themselves homogeneously distributed spatially. We show that although the compositional difference between the two phases is far too small to provide contrast for imaging and analysis by standard data analysis techniques, we can identify the phases by using implanted Ga ions as markers, because they preferentially decorate the amorphous phase. The use of such chemical markers can enhance the capability of APT as an avenue for probing the structures of nanostructured and amorphous alloys with subtle composition inhomogeneities. A review of APT studies on nanostructured and amorphous alloys is provided in section 4.1.

### ***4.1. APT studies on nanostructured and amorphous alloys***

The properties of nanostructured and amorphous alloys rely on details of the solute content and its distribution at the finest scales. For example, in nanocrystalline alloys, chemical ordering and solute enrichment at grain boundaries affect such properties as strength and thermal stability [17, 19, 20, 31, 147-149]. In amorphous alloys, subtle changes in chemical composition influence crystallization behavior and glass forming ability [29, 30, 150-165]. In dual-phase nanocrystal/amorphous composites, the phase composition, phase fraction and phase distribution impact, for instance, their magnetic

---

<sup>3</sup> The APT experiments described in this chapter were done in collaboration with G.B.Thompson and K.L.Torres at the University of Alabama, Tuscaloosa.

[26-32] and mechanical properties [33-35]. Thus, a sound understanding of solute distribution at scales from the nanometer down to the sub-nanometer regime is central to tailoring the properties of nanostructured and amorphous alloys. Unfortunately, many traditional chemical mapping methods like Auger microscopy and energy dispersive x-ray spectroscopy in the transmission electron microscope (TEM) lack the resolution necessary for these advanced problems. On the other hand, three-dimensional atom probe tomography (APT) has very high spatial and chemical resolution, as well as equal sensitivity for all elements [166-168]; as a result, APT has been increasingly used to probe the spatial distribution of atoms in nanostructured and amorphous alloys.

There have been several APT studies on nanocrystalline alloys. Among these, the most common issue addressed is local chemistry at grain boundaries [33, 35-38, 43, 129-136]; nanostructure formation in many such alloy systems is attributed either to the thermodynamic effect of solutes in decreasing grain boundary energy [19, 20, 147], or to the kinetic effect of solutes in inhibiting grain growth [169, 170]. Additionally, APT studies on some Ni-P [17, 31] and Co-P [147] alloys help account for their high thermal stabilities; in such systems, as the alloys are heated to higher temperatures, the extent of solute segregation to grain boundaries increases, thus decreasing the driving force for grain growth. APT has also been employed to elucidate the phase transformation sequence and mechanisms in nanocrystalline alloys [17, 31, 53, 147, 171, 172]: as temperature increases, solute enrichment occurs at the grain boundaries until a new solute-rich phase precipitates there.

Valuable knowledge about amorphous alloys, such as their crystallization mechanism during heat treatment, has also been acquired from APT studies [29, 30, 150-165]. In these studies, clusters of atoms are identified by considering the local density around each atom [28-30, 151-155, 157, 160, 162-165, 173, 174]. The chemical identity of atoms in these pre-nuclei, in turn, helps rationalize the effects of subtle chemical composition changes on the nucleation behavior of the alloys. Dual-phase nanocrystalline/amorphous composites formed by such partial devitrification processes have also been the subject of many APT studies, where the segregation tendencies of solute atoms to the different co-existing phases are established [26-29, 31-35, 159, 161, 175-183]. In some of these works, the volume fraction of each phase, together with its

composition, is quantified, and the microstructures that optimize the magnetic properties [26-32] and malleability [33-35] are identified.

The above studies contribute significantly to our fundamental understanding of nanostructured and amorphous alloys. However, most of these studies are restricted to alloy systems that exhibit strong tendencies for solute segregation to interfaces [17, 19, 20, 31, 147] or among different phases [26-35], and to alloys that experience long thermal exposures [26-29, 31-35, 150, 159, 161, 175-183], which aids redistribution of solute atoms among the different phases. In such cases the extent of solute segregation often exceeds a factor of two, so compositional differences are easily visualized via atom dot maps, and quantified by standard atom probe data analysis techniques, such as ladder diagrams and one-dimensional composition profiles. Very few APT studies have been carried out on weakly-segregating systems, or on multi-phase alloys that are formed by driven or out-of-equilibrium processes without post-annealing, because in such cases, it is challenging to distinguish the different phases and features [19, 20, 178].

#### ***4.1. Experimental procedures***

Four RP alloys were prepared using the procedures described in section 3.1. The compositions of these alloys were measured by energy-dispersive spectroscopy (X-ray Optics/AAT #31102 in a Leo 438VP scanning electron microscope) and confirmed by atom probe tomography (see Table 4.1). In what follows we will refer to these samples by the average compositions determined by both methods, i.e. ~8.0, 9.2, 10.2, and 15.0 at% Mn for samples 1-4, respectively. XRD and TEM characterization of these alloys were performed using the procedures described in section 2.1.

Sharp atom probe tips with radii of curvature between 50 and 100 nm were prepared from the alloy sheets by annular focused ion beam (FIB) milling. The *in situ* lift-out technique described by Thompson and co-workers was used to shape the tips into the appropriate geometry [184]. The lift-out procedure was conducted using a FEI Quanta 3D dual-beam FIB. Initial milling was performed at 30 keV and final milling at 5 keV. The atom probe tips were analyzed using an Imago Scientific Instruments Local Electrode Atom Probe (LEAP ®) 3000XSi. All analyses were performed at  $10^{-9}$  Pa, with a tip temperature of 60 K, a pulse fraction of 25%, and a pulse repetition rate of 200 kHz.

Multiple atom probe tips were prepared and analyzed to ensure data reproducibility. Table 4.1 lists the total number of atoms collected for each APT tip; the typical sample size was between 5 and 15 million atoms. Data analysis was conducted with custom software programs written by the authors.

**Table 4.1 A summary of the total number of atoms collected for each APT specimen, along with its APT and SEM/EDX alloy composition. Also shown are the grain sizes determined from XRD and TEM analysis.**

Deposition number	APT sample	Total number of atoms collected	Composition (at.%)			Grain size (nm)	
			APT		SEM/EDX	XRD	TEM
			Ga	Mn	Mn		
1	A	5,977,410	0.02	8.25	7.8±0.2	-	159
	B	8,765,416	0.17	8.39			
2	C	14,197,531	0.34	9.12	9.5±0.3	25±4	19
	D	9,604,795	0.25	9.03			
3	E	13,401,688	0.24	10.07	10.5±0.3	-	5
	F	10,153,271	0.23	10.21			
	G	7,342,614	0.22	10.13			
4	H	2,202,166	0.12	16.15	14.0±0.3	-	-

## 4.2. Composition and structure of the deposits

This section provides a short review of the composition and structure of the four RP alloys used in this study; the details are discussed earlier in chapter 3. Note, however, that in chapter 3, the alloys are labeled according to the compositions determined using SEM/EDX; in this chapter, the average compositions determined from SEM/EDX and APT are employed (see Table 4.1).

In electrodeposited Al-Mn, there is a well-documented transition in structure as the deposit composition increases through the range of ~6-15 at.% Mn, as discussed in chapters 3 and 4 and prior literature [61, 70, 76, 77, 103]. Generally, single-phase FCC Al(Mn) solid solutions prevail at lower Mn contents, near 6-9 at.%, a second amorphous phase emerges and coexists with nanocrystalline FCC Al(Mn), and at higher Mn contents the structure becomes entirely amorphous [61, 70, 76, 77, 103]. The present set of samples was designed to explicitly cover this range of compositions, to better explore the attendant structural changes. And, our results in Figure 4.1, which shows the XRD

patterns and TEM images of the four samples, bear out the trend described above and discussed in prior literature [61, 70, 76, 77, 103].

In Figure 4.1(a), XRD reveals sharp and narrow peaks in the 8.0 at.%-Mn alloys, which are also consistent with the bright spots observed in the electron diffraction pattern in Figure 4.1(b), and are indexed with the FCC Al(Mn) solid solution reflections. TEM reveals that the grain size of the 8.0 at.%-Mn alloy ranges from 50 to 500 nm, with a number average size of ~159 nm and volume-average spherical-equivalent grain size of 373 nm.

In Figure 4.1(c), the XRD pattern of the 9.2 at.% Mn alloy reveals a broad and low-intensity amorphous-like halo at  $2\theta \approx 42^\circ$ , in addition to the FCC Al(Mn) solid solution reflections. The calculated XRD grain size of the FCC phase is 25 nm. Consistent with this, the bright-field TEM image in Figure 4.1(d) shows a two-phase structure comprising crystals between ~10 and 80 nm in diameter (21 nm number-average and 36 nm spherical equivalent diameter), randomly distributed in an amorphous matrix, which constitutes about one-third of the dual phase structure.

At a higher Mn content of about 10.2 at.%, the amorphous halo dominates the X-ray diffractogram, as shown in Figure 4.1(e), with a barely discernible FCC (111) peak superimposed. Consistent with this, TEM imaging reveals mostly featureless regions, although a very few ~5 nm crystallites can be found embedded in an amorphous matrix; the bright-field image in Figure 4.1(f) shows one of these relatively rare instances. These samples are thus “near-amorphous”.

Finally, at a Mn content of about 15.0 at.%, the alloy comprises only the amorphous phase, as evidenced by the rounded amorphous halo in the XRD pattern and the diffuse ring in the electron diffraction pattern in Figures 4.1(g) and (h), respectively. The bright-field image reveals a featureless microstructure, which is characteristic of an amorphous alloy.

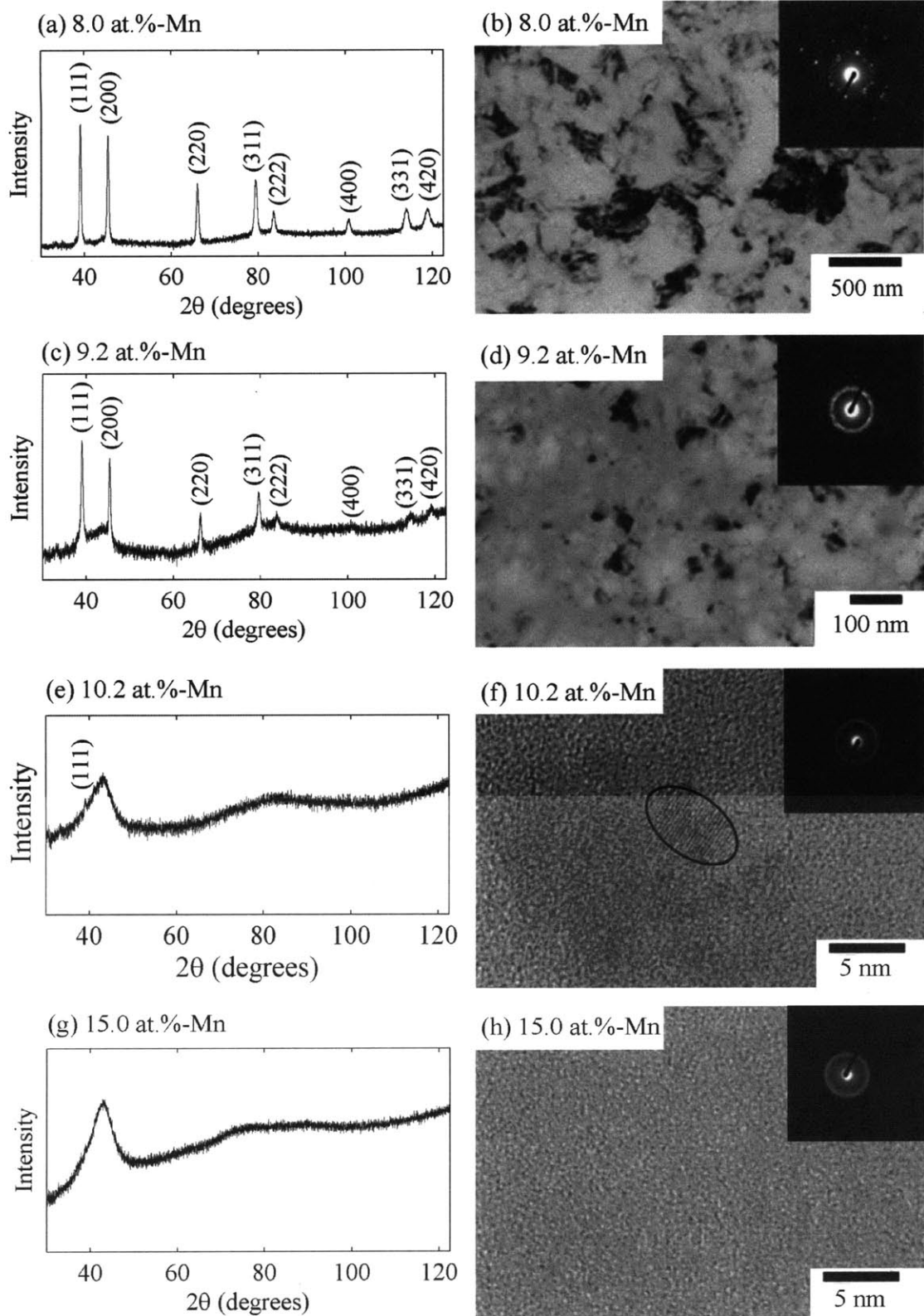


**Figure 4.1** XRD patterns of the electrodeposited Al-Mn alloys are shown on the left column. The corresponding bright-field TEM images and electron diffraction patterns are shown on the right. The four rows respectively correspond to samples 1, 2, 3, and 4, from Table 4.1. Notice the transition from a single FCC phase to an amorphous phase as Mn content increases.

### 4.3. APT analysis of Mn distribution

Perspective views of a few typical APT specimens are shown on the left column of Figure 4.2; the Al and Mn atoms are represented by yellow and blue dots, respectively. Although no dot maps are shown for the 15.0 at% Mn specimen, the data appear very similar those from the 10.2 at% Mn sample in Figures 4.2(e)-(f). In all three specimens, Al and Mn atoms appear randomly distributed to the eye. Similar uniformity in solute distribution is observed in the corresponding two-dimensional atom dot maps shown on the right. These 2 nm-thick cross-sectional slices are extracted perpendicularly to the z-axis of the sampling volume, which lies along the acquisition direction. The only possible suggestion of local compositional variations is for the 9.2 at% Mn specimen in Figures 4.2(c)-(d), which appears somewhat more mottled in appearance than the other samples. To further evaluate the distribution of Mn we now present a quantitative analysis using standard atom probe data analysis techniques. In the following we present typical data for each deposit composition, but we stress that in every case where duplicate APT specimens were analyzed (see Table 4.1), the results were reproducible between samples of the same composition.

First, we employ Mn composition profiles to evaluate characteristic length scales present in the solute distribution. The specimen volume is divided into  $1.5 \times 1.5 \times 1.5$  nm blocks on a fixed grid, resulting in  $n_x$ ,  $n_y$ , and  $n_z$  blocks in each of the three directions. The composition in each block is then computed, yielding  $c^i(x, y, z)$ , where  $i$  denotes the composition of a given species, e.g., Mn. For each chain of composition blocks parallel to the x-axis, its average solute content,  $c_0^i(y, z)$ , and the corresponding standard deviation,  $\sigma_0^i(y, z)$ , are also calculated. Figure 4.3 shows typical composition profiles along the x-direction for all four specimens. The horizontal solid lines in these plots represent the average composition, i.e.,  $c_0^i(y, z)$ , and the dashed lines denote values that are two standard deviations above or below the average composition, i.e.,  $c_0^i(y, z) \pm 2\sigma_0^i(y, z)$ . Values exceeding the upper threshold represent statistically significant solute enrichment; values below the lower threshold denote solute depletion.



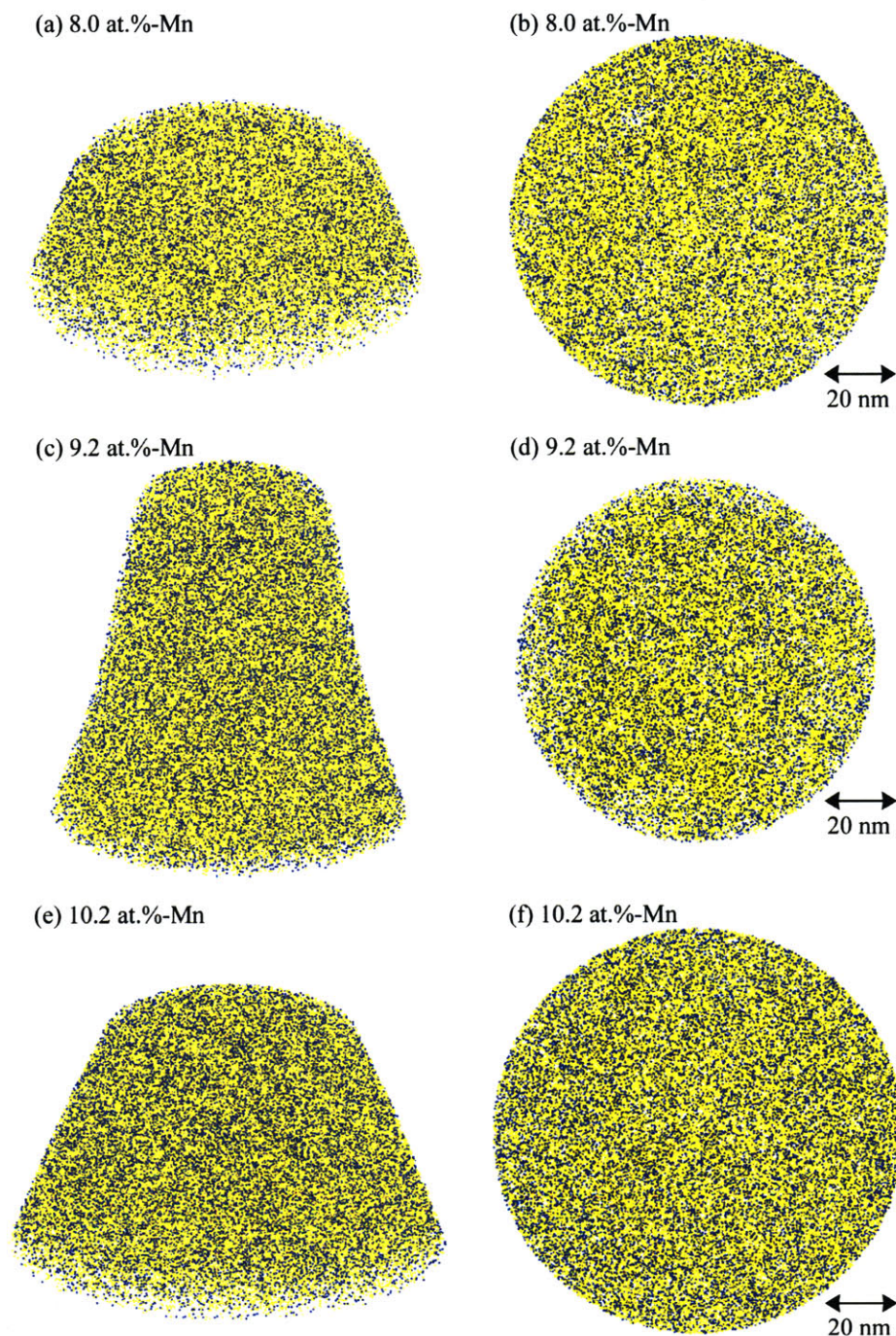


**Figure 4.2** Perspective views of a few representative APT specimens are shown on the left column with corresponding two-dimensional atom dot maps in the x-y plane on the right. These images are obtained from (a)-(b) sample 1A, (c)-(d) sample 2C and (e)-(f) sample 3E (see Table 4.1). The yellow dots represent Al atoms and the blue dots denote Mn atoms.

Figure 4.3 shows that in samples from each of the four specimens, Mn content fluctuates only mildly about its mean value. For each sample, the local Mn content remains within two standard deviations of the mean value; only rarely does the

composition even approach the upper threshold, and there is no convincing spike of Mn content that would be regarded as a clear signature of local enrichment. Such results are in contrast to strongly-segregating systems, where the composition profiles not only reveal regions of local solute enrichment or depletion, but also the characteristic length-scales involved [185].

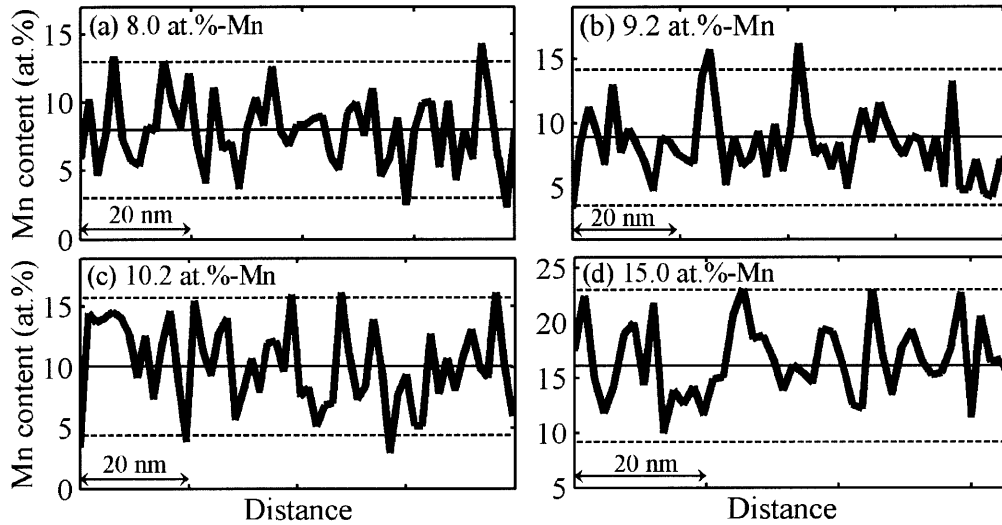


**Figure 4.3** Typical one-dimensional composition profiles of Mn in the APT specimens. The sampling volume was divided into  $1.5 \times 1.5 \times 1.5$  nm blocks to compute the local solute content. The thin horizontal line represents the average solute content; the thin dashed lines represent values that are two standard deviations away from the average composition. In all four samples, Mn distribution appears uniform.

The lack of periodicity in Mn composition distribution is also confirmed statistically using the autocorrelation function along the long axis of each sample. Figure 4.4 shows a few representative autocorrelation functions (represented by solid lines), which all decay rapidly to negligible values and exhibit no non-trivial peaks. Non-trivial peaks in these data would indicate a characteristic wavelength in composition distribution, and their absence is suggestive of a homogeneous Mn distribution. What is more, all of the fluctuations and noise in the data here are purely an artifact of sample size: when the chemical identities of the atoms in these samples are randomized at constant compositions, the dashed lines in Figure 4.4 result. The similarity of the autocorrelation functions for the true data and compositionally randomized data verify that the Mn distribution is homogeneous.

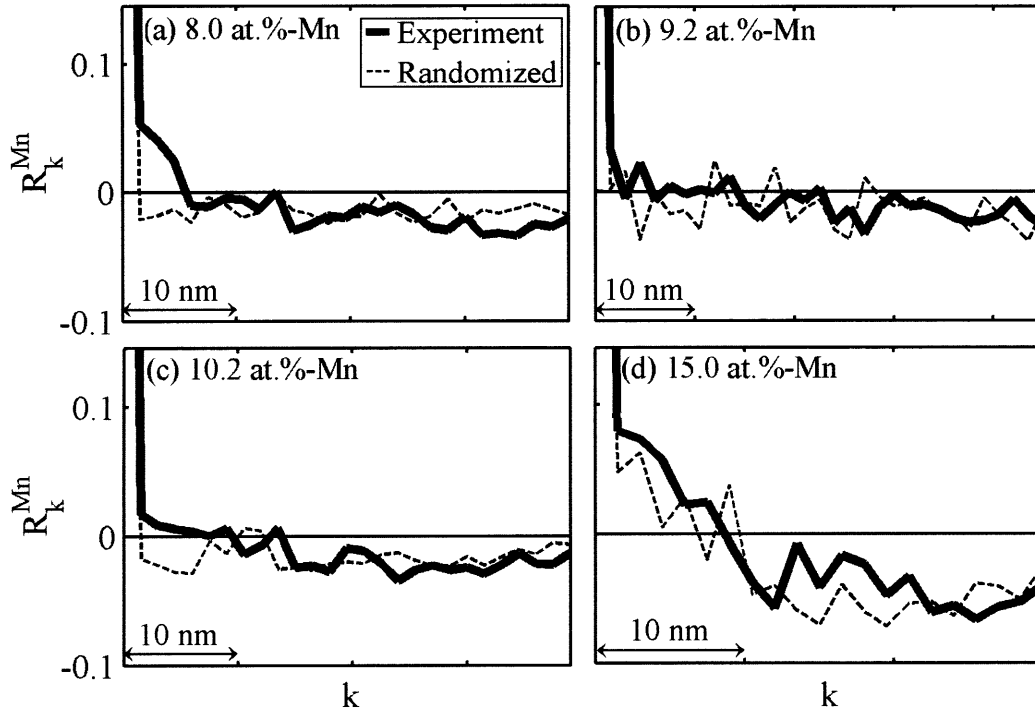


Figure 4.4 Autocorrelation functions of Mn content along the long axis of each sample, plotted as a function of wavelength,  $k$ . The sampling volume was divided into  $1.5 \times 1.5 \times 1.5$  nm blocks to compute the local solute content. The thick solid lines represent experimental results, whereas the thin dashed lines denote results obtained for compositionally randomized structures with the same atomic positions.

Finally, statistical analysis of the Mn content is performed by counting the frequency of composition observations amongst small blocks within a single sample. For this analysis we divide the specimen volume into blocks containing 100 Al and/or Mn atoms. The results are shown by solid circles in Figure 4.5 for a set of typical specimens spanning the four compositions. The dashed curves in Figure 4.5 represent the probability density function,  $P(c)$ , of a normal approximation to the binomial distribution:

$$P(c) = \frac{1}{\sigma\sqrt{2\pi}} \exp\left(-\frac{(c - c_0)^2}{2\sigma^2}\right), \quad (4-1)$$

where  $\sigma^2 = c_0(1 - c_0)/n$  and  $n=100$ . The binomial distribution describes the case of a perfectly random binary solid solution, since it represents  $n$  independent series of Bernoulli trials; in a perfectly random alloy, the probability of a solute atom occupying any atomic site is that of a Bernoulli trial, which depends only on the average concentration,  $c_0$ . Since  $n$  is sufficiently large, the normal approximation holds [186].

Figure 4.5 shows that the composition distributions in all of our specimens agree rather favorably with the binomial distributions. In fact, for the samples containing 8.0, 10.2 and 15.0 at.%-Mn, the data are in excellent agreement with the binomial distribution (c.f. Figures 4.5(a),(c) and (d)), with very high coefficients of determination of  $R^2 = 0.985, 0.992$  and  $0.992$ , respectively. In these specimens, there is no suggestion from the present data that there is any significant solute clustering or ordering; the data support the interpretation of a homogeneous Mn distribution.

Only in the case of the 9.2 at% Mn sample is there any hint of non-random solute distribution. For this specimen (Figure 4.5(b)) there is a small but reproducible disagreement between the measurement and the binomial distribution, especially at compositions between 8 and 11 at.% (highlighted by an arrow on the figure). The experimental distribution is somewhat shorter than the binomial; such a deviation is directionally suggestive of some degree of solute segregation or phase separation. However, the difference is sufficiently small that, by itself, it cannot be construed as decisive evidence of any structural heterogeneity. Quantitatively, the disagreement is very slight for the two separate samples tested in this work (samples 2C and 2D in Table 4.1), their coefficients of determination for Equation (4-1) being high at  $R^2 = 0.977$  and  $0.978$ , respectively.

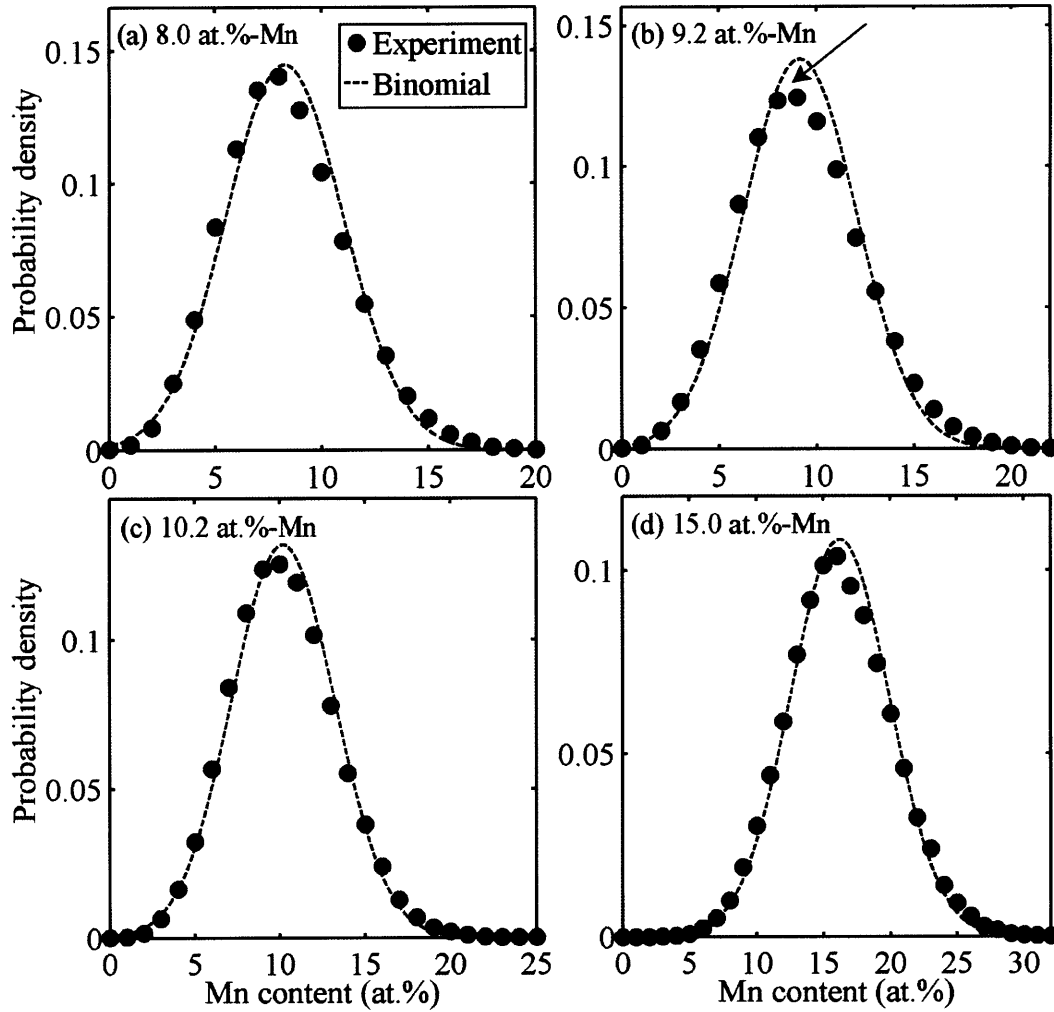


Figure 4.5 Composition distributions of Mn based on binning the APT data into blocks containing 100 Al and Mn atoms. Experimental results are denoted by solid circles and the binomial distributions are represented by dashed lines. The coefficients of determination,  $R^2$ , are (a) 0.985, (b) 0.977, (c) 0.992 and (d) 0.992. Notice that in (b), there is a slight discrepancy between the experimental result and binomial curve, especially between 8 and 11 at.%-Mn (highlighted by an arrow).

#### 4.4. Enhancing APT phase contrast with Ga markers

The above section showed that both qualitatively and quantitatively, the distribution of Mn in our alloys appears, to first order, very uniform at all four compositions. And for the samples with 8.0, 10.2, and 15.0 at% Mn, this result may be construed as reasonable, since these samples are all essentially single-phase (FCC, near-amorphous, and amorphous, respectively). However, the 9.2 at% sample is a two-phase structure that is about two-thirds FCC Al(Mn) and one-third amorphous (cf. Figure 4.1(c) and (d)). Therefore, that the APT results suggest a uniform composition is somewhat

surprising for this sample. It is certainly interesting that for the 9.2 at% Mn sample, there are a few subtle suggestions of irregular Mn distribution, such as the more mottled appearance of the dot map in Figure 4.2(d) or the slight deviation of the composition distributions from the binomial case in Figure 4.5. However, none of these hints constitutes clear evidence of Mn partitioning into two identifiable phases. Because the scale of the APT specimens ( $\sim 100 \times 100$  nm) is significantly larger than the characteristic scale of the dual-phase structure in the 9.2 at% Mn sample ( $\sim 20$ -30 nm), there is little doubt that the APT specimens should sample both phases, which are each present with significant volume fractions. Thus, we conclude that the Mn partitioning between FCC and amorphous phases must be very weak in this system. With no structural information from the APT data, and Mn distributed nearly uniformly, we describe in what follows an alternative method of revealing phase contrast in the APT data.

Because the present specimens were all prepared through the use of FIB milling with Ga ions, they all contain implanted Ga. Combined with the well-known rapid diffusion of Ga in Al [187-191], this leads to Ga atoms distributed throughout the APT samples. The positions of Ga atoms in the specimens shown in Figure 4.2 are represented by red dots in Figure 4.6. There are several noteworthy features in these images. First, in Figures 4.6(a)-(b) and (e)-(f), we observe that in the single-phase samples (FCC and near-amorphous), the distribution of Ga is quite homogeneous; although it is not shown here, we find the same homogeneity of Ga in the fully amorphous 15.0 at%-Mn sample as well. Second, the Ga atoms in the two-phase 9.2 at%-Mn specimen, as illustrated in Figures 4.6(c)-(d), appear strongly segregated into patches that have a width of about 10 nm, and which are situated around relatively Ga-free domains of about  $\sim 20$  and 40 nm in diameter. Third, the total content of Ga is very low in FCC Al(Mn) in Figures 4.6(a)-(b), while it is substantially higher in the near-amorphous sample in Figures 4.6(e)-(f). Table 4.1 shows that the global Ga compositions in these phases are more than an order of magnitude different at 0.02 at.% and 0.34 at.%, respectively.



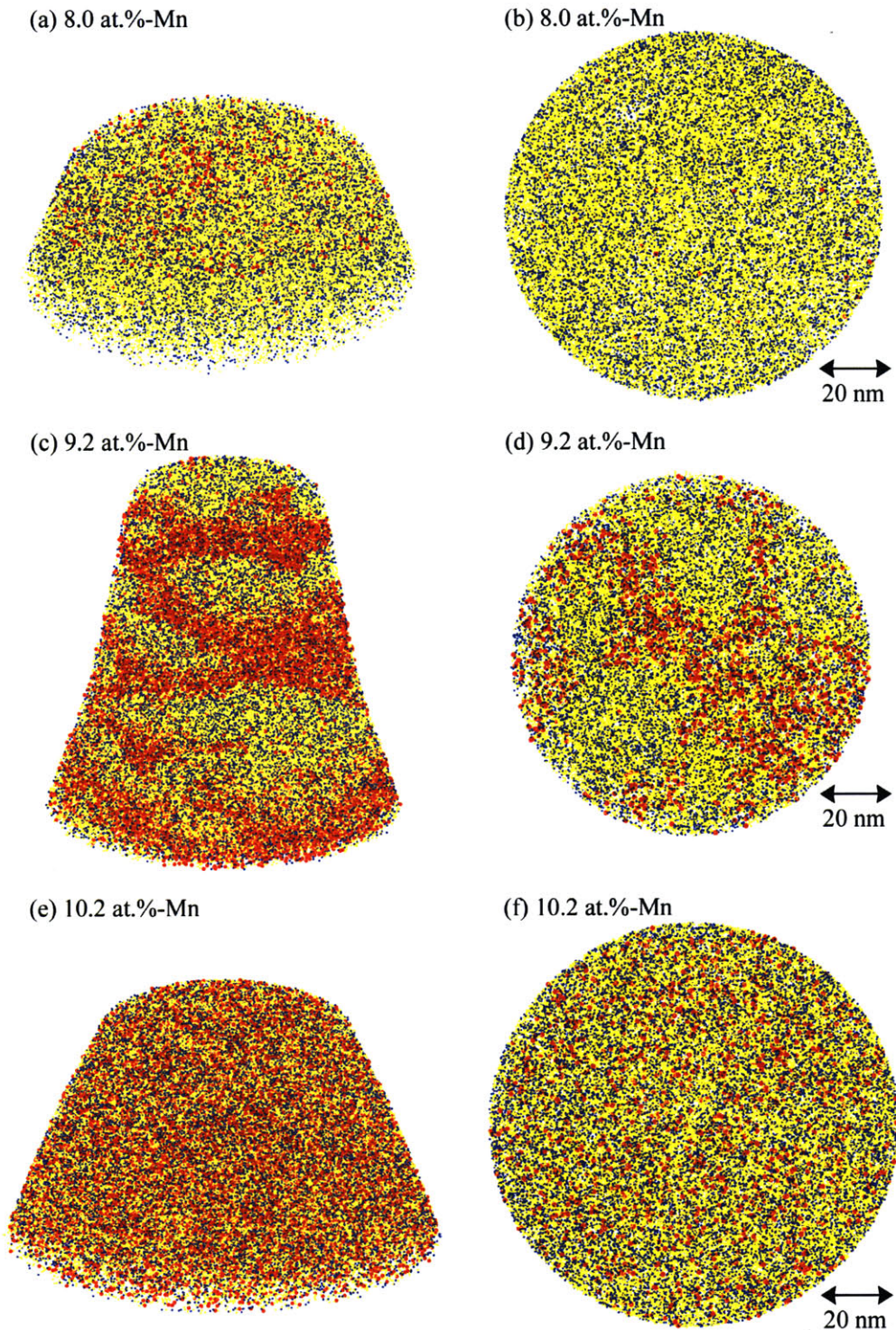


**Figure 4.6** Perspective views of a few typical APT specimens are shown on the left column and the corresponding two-dimensional atom dot maps are shown on the right. These images are obtained from the same samples as those shown in Figure 4.2, i.e. (a)-(b) sample 1A, (c)-(d) sample 2C and (e)-(f) sample 3E. In addition to the Al (yellow dots) and Mn (blue dots) atoms already shown in Figure 4.2, the dot maps presented here also show the Ga atoms (red dots). Figures 4.6(c)-(d) show a strongly-partitioned Ga distribution.



Combining the above three observations from Figure 4.6 with the knowledge of the structure and phases in these samples from Figure 4.1, we conclude that Ga preferentially decorates the amorphous phase in these samples. The notion of structure-dependent Ga distribution is supported by extensive experimental and theoretical studies on the rapid penetration of liquid Ga along disordered intergranular regions in Al [187-191]. By analogy, we suggest the Ga distribution in Figures 4.6(c) and (d) traces the locations of the more disordered, amorphous phase in the dual-phase sample. This effect is reproducible, being observed in both of the two dual-phase samples prepared for APT analysis; Figure 4.7(a) shows a 2-nm thick slice of the second sample (sample 2D), also revealing a dual-phase structure in the Ga distribution. In both Figure 4.6(c-d) and Figure 4.7(a), Ga atoms preferentially populate the periphery of regions that have the same characteristic dimensions as the nanocrystals observed in Figure 4.1(d), i.e. between ~15 and 40 nm in diameter.

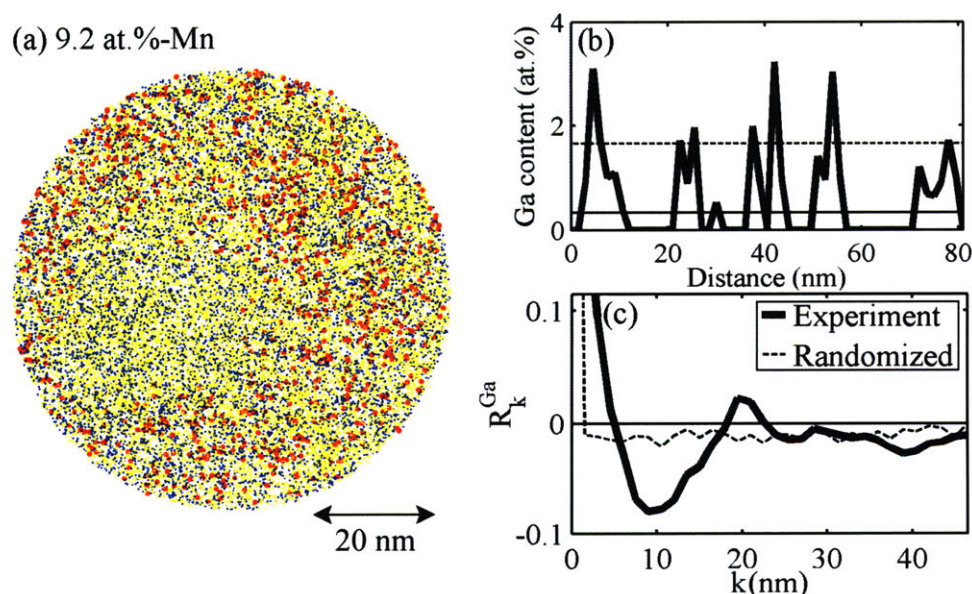


**Figure 4.7** (a) Two-dimensional atom dot map of sample 2D, showing Ga atoms (red) preferentially occupying patches that surround domains that are relatively Ga-free; these domains are between ~15 and ~40 nm in diameter. Such a non-uniform Ga distribution is similar to that observed in Figure 4.6(d) for sample 2C. For these 9.2 at.%-Mn samples, a typical composition profile of Ga is shown in (b) and the autocorrelation function is shown in (c) with  $k$  the wavelength. The plots in (b) and (c) indicate strong Ga segregation at a wavelength of ~20 nm.

That Ga partitioning is observed and reveals the same basic structure expected from TEM analysis in both samples 2C and 2D, and is not observed in any of our single



phase samples, strongly substantiates the use of Ga as chemical markers for the amorphous phase. This information can be used in a more quantitative sense to analyze the phases and structure of the dual-phase specimens, as discussed in more detail below.

Statistical analysis verifies that Ga distributes uniformly in the single-phase samples: not only do their composition profiles reveal statistically insignificant variations in Ga composition, but the autocorrelation functions for Ga also do not exhibit any non-trivial peaks (not shown here). In stark contrast, the Ga composition profile of the dual-phase specimen, as illustrated in Figure 4.7(b), is highly non-uniform, comprising a few localized regions of very high Ga content—up to several percent, despite a global concentration of just 0.34 at.%. Whereas some regions do not contain any Ga atoms, those that do are either locally-enriched with Ga (i.e., contain significantly more than the average concentration), or located in close proximity to other Ga-enriched regions. The enrichment factor in these regions is as high as ~8, and they occur at spatial intervals between ~15 and 25 nm.

The corresponding Ga autocorrelation function is presented in Figure 4.7(c). Unlike all the Mn autocorrelation data in Figure 4.4, the Ga autocorrelation curve illustrated in Figure 4.7(c) exhibits a large negative trough followed by a positive peak at 20 nm. This curve is statistically significant, as verified by comparing with the dashed line in Figure 4.7, which is constructed by using the same set of spatial coordinates and randomizing the chemical identity of the atoms at fixed composition. The non-trivial positive peak in Figure 4.7(c) corresponds to the average wavelength of the composition variation, and the magnitude of the first negative minimum is indicative of the extent of composition variation [185]; this data thus indicates strong Ga segregation at a characteristic wavelength of ~20 nm.

The length-scale of Ga segregation (~20 nm) obtained from Figure 4.7(c) concurs remarkably well with the number average FCC grain size (~21 nm) measured from Figure 4.1(d). Thus, the above quantitative analysis is in line with our qualitative assessment of Figures 4.6 and 4.7: Ga preferentially populates the amorphous phase.

Careful cross-examination of Figures 4.2(d) and 4.6(d) suggests that the Ga-enriched regions in Figure 4.6(d) may correspond to regions that are slightly Al-depleted (or equivalently, Mn-enriched) in Figure 4.2(d). To quantitatively assess the co-

segregation behaviors of Mn and Ga, we employ contingency tables. The results obtained for specimens of three compositions are shown in Tables 4.2-4.4; this analysis is not possible for the 8.0 at% specimen because of its very low Ga content (0.02 at%). These tables are constructed from non-overlapping blocks that contain 100 Al atoms each, following ref. [185]. Here the experimental values that exceed those expected for a random, uncorrelated condition are shaded dark grey, whereas those that are lower are shaded light grey. The chi-squared statistic is used to evaluate the extent of deviation from randomness; the ratios between the chi-squared values computed from Tables 4.2-4.4 and the corresponding values at the 0.001% significance level are 81, 1.2 and 1.1; these respectively refer to the three compositions: 9.2, 10.2, and 15.0 at% Mn. Since the ratios for the 10.2 and 15.0 at.%-Mn specimens are very close to unity, Mn and Ga distributions are very likely uncorrelated in these specimens. On the other hand, there is compelling evidence for Mn and Ga co-segregation in the 9.2 at.%-Mn specimen, with a chi-squared ratio of 81, much greater than unity.

**Table 4.2 Contingency table for blocks of atoms containing 100 Al atoms in the 9.2 at.%-Mn specimen. The chi-squared statistic for experimental deviation from randomness is 2259 and the corresponding value at the 0.001% significance level is 28.**

		# Ga atoms				
		0	1	2	>2	Total
# Mn atoms	0-4	5389	663	163	64	6279
	5-9	41334	7377	2497	961	52169
	10-14	37399	9277	3663	1648	51987
	>14	9323	3020	1423	737	14503
	Total	93445	20337	7746	3410	124938

**Table 4.3 Contingency table for blocks of atoms containing 100 Al atoms in the 10.2 at.%-Mn specimen. The chi-squared statistic for experimental deviation from randomness is 33 and the corresponding value at the 0.001% significance level is 28.**

		# Ga atoms				
		0	1	2	>2	Total
# Mn atoms	0-5	4253	924	113	14	5304
	6-10	22912	5484	639	61	29096
	11-15	18412	4614	576	52	23654
	>15	4201	1084	165	12	5462
	Total	49778	12106	1493	139	63516

**Table 4.4** Contingency table for blocks of atoms containing 100 Al atoms in the 16.0 at.-%-Mn specimen. The chi-squared statistic for experimental deviation from randomness is 26 and the corresponding value at the 0.001% significance level is 23.

		# Ga atoms			
		0	1	$\geq 2$	Total
# Mn atoms	0-11	789	65	16	870
	12-16	3640	431	47	4118
	17-21	5400	716	76	6192
	>21	4521	646	79	5246
Total		14350	1858	218	16426

Given that Ga partitions to the amorphous phase, and that Mn and Ga are statistically co-segregated, we conclude that albeit subtle, Mn preferentially occupies the amorphous regions in the dual-phase sample as well. To further verify this point, we now employ Ga atoms as chemical markers for the amorphous phase and directly probe the Mn content in the two phases. Using the 1.5 x 1.5 x 1.5 nm composition blocks described earlier, blocks of atoms that contain more than 1.74 at.-% Ga are considered Ga-enriched (this level being two standard deviations, 1.40%, from the mean Ga content, 0.34%). Thus, the average Mn content in these Ga-enriched regions corresponds to that of the amorphous phase. The solute content of the crystalline phase is obtained from the blocks of atoms that lie in the center regions of the domains that are relatively free of Ga. The average Mn contents in these regions are 10.1 at.-% and 8.0 at.-%, respectively.

The relatively subtle enrichment of only ~2 at.-%-Mn in the amorphous phase is very reasonable in light of our statistical analyses in the previous section, which concluded that any segregation was sufficiently subtle as to be transparent to conventional statistical methods. However, we may return to the results of Figure 4.5(b) to verify the small extent of Mn segregation in the dual phase sample. Although the data in Figure 4.5(b) is close to a binomial distribution, the fit is not perfect, and the subtle segregation of Mn to the amorphous phase could account for this. To incorporate the effects of Mn preferentially partitioning into the amorphous phase, we modify equation (4-1) by assuming that the composition distribution in each phase follows a binomial distribution about its own unique average composition. Thus, the corresponding

composition distribution for an alloy that contains an  $\alpha$  and  $\beta$  phase, with volume fractions  $f_\alpha$  and  $f_\beta$ , is given by:

$$P(c) = \frac{f_\alpha}{\sigma_\alpha \sqrt{2\pi}} \exp\left(-\frac{(c - c_{0,\alpha})^2}{2\sigma_\alpha^2}\right) + \frac{f_\beta}{\sigma_\beta \sqrt{2\pi}} \exp\left(-\frac{(c - c_{0,\beta})^2}{2\sigma_\beta^2}\right), \quad (4-2)$$

under the constraints that  $f_\alpha + f_\beta = 1$  and  $f_\alpha \cdot c_{0,\alpha} + f_\beta \cdot c_{0,\beta} = c_0$ . Without prior knowledge on the volume fraction or composition of either of the two phases, two adjustable parameters remain:  $f_\alpha$  or  $f_\beta$  and  $c_{0,\alpha}$  or  $c_{0,\beta}$ .

Using  $\alpha$  to denote the amorphous phase and  $\beta$  the crystalline phase, a least-squares fit of equation (4-2) to our experimental data in Figure 4.5(b) is used to determine these parameters. The result of this fit is shown in Figure 4.8 as a thick solid curve (labeled “binomial-binomial”).

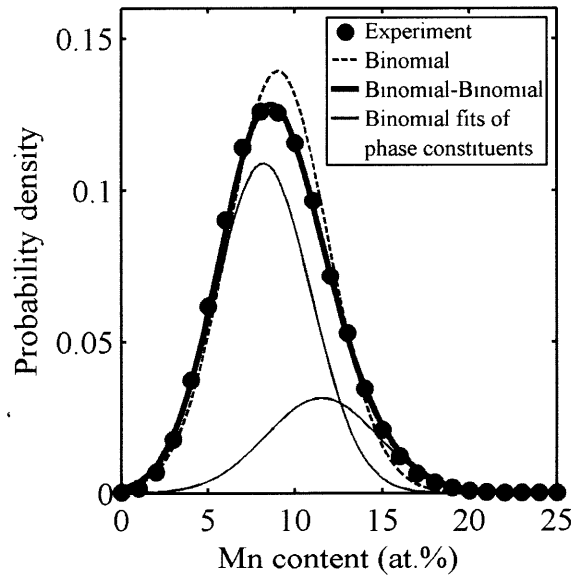


**Figure 4.8** Composition distribution of Mn in the 9.2 at.% Mn sample; the experimental data are the same as those shown in Figure 4.5(b), as is the expected binomial distribution curve (dashed line). The two-phase binomial-binomial fit is represented by the thick solid line and its individual components are represented by thin solid lines. The coefficient of determination,  $R^2$ , of the binomial-binomial fit is 0.999, much higher than that of the single binomial (0.977).

The parameters that yield the binomial-binomial fit are  $f_\alpha = 0.25$  and  $c_{0,\alpha} = 0.115$ , which leads to  $f_\beta = 0.75$  and  $c_{0,\beta} = 0.082$ . Figure 4.8 shows that modeling the composition distribution with equation (5-2) provides a much better fit to our experimental data than a single binomial distribution, with a coefficient of determination  $R^2 = 0.999$  for both samples 2C and 2D (as compared to  $\sim 0.977$  and  $0.978$ , respectively, for a single binomial distribution). The Mn contents in the amorphous and crystalline phases obtained from

this indirect method (11.5 and 8.0 at.%) are also in reasonable agreement with those obtained from directly measuring the Mn contents in the Ga-enriched and Ga-depleted regions (10.1 and 8.0 at.%) – Both methods show that the local Mn enrichment is between about 2 and 3 at.%. Finally, the phase fractions returned by fitting two binomial curves (25% amorphous) match well with our estimate from TEM observations (~33% amorphous).

We may also use the Ga markers to shed new light on the composition profile in Figure 4.3(b), from which we observed that the standard criterion used to define solute enrichment (i.e. two standard deviations) exceeded the actual extent of solute enrichment, and the characteristic wavelength for Mn enrichment could not be identified. In Figure 4.9, we revisit the same Mn composition profile (Figure 4.9(b)), but now we use the corresponding Ga composition profile (Figure 4.9(a)) as a criterion to identify the shaded bands.

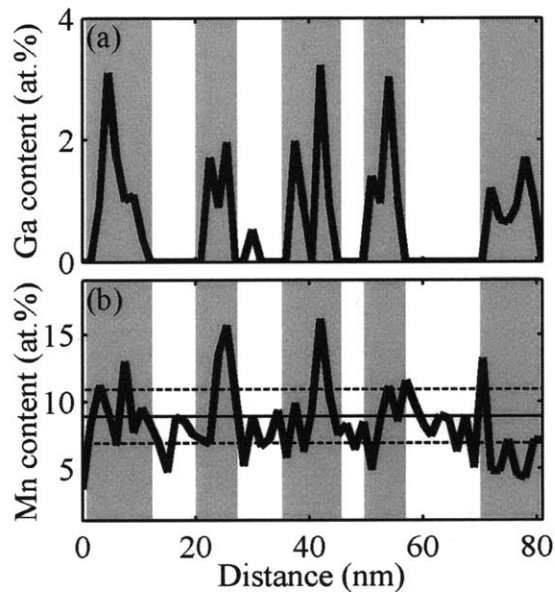


**Figure 4.9** Composition profile of (a) Ga and (b) Mn along the long axis of the 9.2 at.%-Mn specimen (sample 2C). Regions containing Ga are shaded gray. Note that in these regions, the local Mn contents are >2 at.% above the average composition (represented by the upper dashed line).

Although only two of these bands coincide with regions that would be considered formally “Mn-enriched” according to the  $2\sigma$  criterion (see Figure 4.3(b)), we now observe that all of the bands are associated with local rises in Mn content that exceed the average solute content by more than ~2 at.% (this value is represented by the upper dashed line in Figure 4.9(a)). Thus, the co-segregation of Mn and Ga permits a more

nuanced view of these composition profiles. The Mn-enriched regions identified in this way and shaded gray in Figure 4.9, are separated by a periodic distance of about 15 to 20 nm, consistent with the autocorrelation peak at 20 nm and the average crystal size observed in TEM.

All of the characterization data in this section are mutually consistent, and suggest that our dual phase sample is roughly comprised one-third of an amorphous phase, which is slightly enriched in Mn by a factor of about 1.4. The use of Ga as a marker for the amorphous phase permits this conclusion to be drawn with considerable certainty, whereas without the use of the markers no conclusions about the phases, their distribution or compositions, could be drawn.

#### ***4.5. Conclusions***

One of the greatest challenges in using atom probe tomography to analyze nanostructured alloys involves identifying different microstructural features, such as grains, grain boundaries and different phases, from chemical signatures alone. In this work, we employ APT to study the solute distributions in nanostructured Al-Mn alloys, where the solute exhibits only a slight tendency to partition into the amorphous phase. We examine four unique compositions that comprise different amounts of crystalline and amorphous phases. Standard data analysis techniques show that Mn is uniformly distributed in the fully crystalline and amorphous specimens. Additionally, even for a specimen known to be dual-phase (amorphous plus FCC nanocrystals), these techniques provided no convincing evidence of Mn partitioning between the phases.

Phase contrast in these samples was enhanced by examining the distribution of Ga, introduced as an artifact from sample preparation by FIB machining of the APT specimens. Whereas the Ga distributions observed in the single phase specimens (either FCC or amorphous) are uniform, the amorphous phase incorporates much more Ga than does the crystalline phase. Because of this, the dual phase specimen shows a large phase contrast in the distribution of Ga atoms, which are markers for the amorphous phase. In this sample, the Ga-enriched regions form a network that surrounds regions with characteristic dimensions that are consistent with the average grain size. Direct measurements of Mn contents in the Ga-enriched and Ga-poor regions reveal a slight

segregation tendency of Mn to the amorphous phase (10.1 vs. 8.0 at.-%-Mn, respectively). An indirect method, which involves modeling the Mn composition distribution in each phase with a unique binomial distribution and fitting the resulting binomial-binomial distribution to the experimental results, is also employed. The Mn contents in the amorphous and crystalline phases are determined to be 11.5 and 8.0 at.%, respectively. The good agreement in results obtained from both methods confirms that Mn segregates subtly (by ~2 at.%) to the amorphous phase and further validates the use of Ga ions as chemical markers for the amorphous phase.

## 5. Conclusions

This thesis seeks to tailor the nanostructures of electrodeposited lightweight alloys to achieve high hardness and toughness. To this end, this thesis research involves (a) electrodeposition of nanostructured lightweight Al-Mn alloys at ambient temperature, (b) tailoring the structures of Al-Mn alloys to improve their mechanical properties, as well as (c) developing a method to characterize dual-phase nanostructured alloys with atomic-level resolution.

Using Al-Mn as a model system that exhibits a wide range of structures and phases, factors that promote nanostructure formation are investigated through electrodeposition experiments. Al-Mn alloys with Mn content ranging from 0 to 15.8 at.% are prepared by electrodeposition from an ionic liquid at room temperature and their structures are systematically analyzed. For alloys with Mn content up to 7.5 at.%, increasing Mn additions leads to a decrease in grain size of microcrystalline FCC Al(Mn). Between 8.2 and 12.3 at.% Mn, an amorphous phase appears, accompanied by a dramatic reduction in the size of the coexisting FCC crystallites to the ~2-50 nm level. At higher Mn contents, the structure is apparently entirely amorphous. For the first time, we show that these apparently “amorphous” electrodeposits contain pre-existing nano-quasicrystalline nuclei. Coupled to prior reports on the direct deposition of quasicrystals at 325°C, our results indicate that low temperature favors nanostructuring down to the amorphous limit. Even though the nanostructured and amorphous alloys exhibit high hardness above 3 GPa, their ductility falls below 5%, likely because of grain sizes that are less than ~10 nm, the appearance of a brittle amorphous phase, as well as inhomogeneous phase distribution.

Based on the experimental results, which indicate that electrode kinetics govern the structure of electrodeposited Al-Mn alloys, a reverse-pulse current waveform is used to synthesize Al-Mn alloys for the first time. Reverse-pulsing is found to promote nanocrystalline grain sizes in the single phase FCC alloys, alter the grain size distribution of the dual-phase alloys (such that a low fraction of grains are less than 10 nm in diameter), as well as homogenize the phase distribution of the dual-phase alloys. Consequently, a combination of high hardness (>3GPa) and toughness (>5% elongation)



is achieved in lightweight Al-Mn alloys. The deformation mechanisms of the nanocrystalline alloys include dislocation pinning and accumulation, as well as grain coalescence. In the amorphous alloys, simultaneous operation of multiple shear bands likely induces some degree of malleability.

The homogeneous phase distribution in the reverse-pulsed alloys, coupled to the weak partitioning tendency of Mn into the different phases, renders traditional techniques, such as STEM and EDX in the TEM, inadequate for probing solute distribution in the RP alloys. To this end, a method to enhance phase contrast in atom probe tomography is developed. Standard APT data analysis techniques show that Mn distributes uniformly in single phase (nanocrystalline or amorphous) specimens, and despite some slight deviations from randomness, standard methods reveal no convincing evidence of Mn segregation in dual-phase samples either. However, implanted Ga ions deposited during sample preparation by focused ion-beam milling are found to act as chemical markers that preferentially occupy the amorphous phase. This additional information permits more robust identification of the phases and measurement of their compositions. Our results indicate weak partitioning tendency of Mn into the amorphous phase in these alloys. Thus, our work shows that the use of chemical markers can enhance the capability of APT as an avenue for probing the structures of nanostructured and amorphous alloys with subtle composition inhomogeneities

In closing, this thesis research presents the first systematic structural characterization and property measurement of Al-Mn alloys electrodeposited at ambient temperature. A new method of using chemical markers to enhance phase contrast in APT is also developed. The major highlight of this thesis is our ability to tailor the nanostructure of Al-Mn alloys to achieve an unprecedented combination of high hardness and toughness in these lightweight alloys. We are optimistic that the use of chemical markers will extend the capability of APT for nanostructure characterization and that the hard and tough Al-Mn alloys synthesized in this work will have useful practical applications.

## 6. Directions for Further Research

This thesis represents significant improvements in our ability to synthesize, tailor and characterize the structures of electrodeposited lightweight alloys. Future research will most definitely help expand on the knowledge gained here and open the doors to useful practical applications of these alloys. More specifically, the following issues can be further explored:

- In chapter 2, grain size refinement in the microcrystalline regime is attributed to nucleation kinetics at the electrode, based on linear sweep voltammetry results obtained for other molten salts. To better control grain size in the single phase regime, future work can investigate the electrochemical effects of adding manganese chloride to the chloroaluminate ionic liquid.
- The existence of nano-quasicrystalline nuclei in the amorphous 15.8 at.%-Mn alloy is proved indirectly from calorimetric measurements in chapter 2. It would be of great scientific interest to directly identify these clusters of atoms from APT experiments. In fact, such experiments can be carried out on amorphous alloys with different Mn contents to establish possible relationships between solute content and the density of pre-existing nano-quasicrystalline nuclei. The existence of such nuclei may affect the toughness of Al-Mn alloys, thus establishing such relationships may be of practical importance.
- In chapters 2 and 3, the effects of temperature have not been explored. More specifically, results from chapter 3 indicate that structural homogeneity enhances the toughness of the deposits. By extension, high temperature electrodeposition experiments should also result in more uniform structures that exhibit desirable mechanical properties. Future experiments can be performed to verify this hypothesis.
- The use of reverse-pulsing to improve the ductility of Al-Mn alloys is illustrated in chapter 3 for a specific waveform. Variations in pulse durations, pulse current densities, shape of the current waveform, etc. are likely to influence the alloy's structure and property as well. Experiments that seek to identify the set of

experimental variables that optimize the mechanical properties of the alloys are in order.

- Results in chapters 2 and 3 indicate that reverse-pulsing enhances the malleability of the amorphous alloys. It is well-known that the ductility of amorphous materials is very sensitive to vacancy content and chemical ordering. Thus, future research can employ small angle x-ray and neutron scattering to obtain information about the pair distribution functions in these alloys, so as to better comprehend the effects of reverse-pulsing on the structure of amorphous alloys, as well as identify local structures that enhance malleability.
- That reverse-pulsing dramatically improves the properties of Al-Mn alloys hints of potential benefits in extending this technique to other lightweight alloys, such as Mg and Ti.

## **Appendix A. Kinetic Monte Carlo simulations of nanocrystalline film deposition<sup>4</sup>**

### ***A.1. Introduction***

Various deposition techniques, such as chemical and physical vapor deposition, molecular beam epitaxy, electrochemical deposition and reactive sputtering, have been successfully employed to produce nanostructured films. While extensive experimental works [36, 41, 192-195] have been carried out to investigate the effects of processing conditions on such properties as film porosity, surface roughness and grain size, the growth mechanisms of nanostructured films are, as yet, incompletely understood on a microscopic level.

A variety of computer simulations have also been used to study polycrystalline film growth. Continuum models have been proposed for the evolution of grain microstructure, surface roughness and texture during film growth [196, 197], and involve evaluation of the equations of motion for grain boundaries. Such models can incorporate various driving forces, including grain boundary curvature and anisotropic grain boundary energy. However, these models do not explicitly consider other defects formed during film growth, such as vacancies and voids [198, 199], and it is not straightforward to incorporate nucleation of new grains—a process that must occur during nanostructured film growth [200]. On the other hand, discrete models based on molecular dynamics have not only been employed to simulate kinetic processes such as diffusion and grain boundary migration [201], but also to simulate vacancy entrapment and void formation during the film growth process [202, 203]. For example, Smith and co-workers explored the mechanism of void formation during film growth [202], as well as interactions between voids and grain boundaries in bi-crystals [203]. The major drawback of molecular dynamics pertains to the small length and time scales it can access, which, in the above studies limited the deposited film thickness to at most 100 monolayers. Kinetic

---

<sup>4</sup> The content of this chapter has been published in ref. [85]

roughening and subsequent grain nucleation during film growth thus cannot be adequately captured via molecular dynamics methods.

By excluding details of atomic vibrations and using a rigid lattice, discrete models that are based on the kinetic Monte Carlo (kMC) algorithm [204] are less computationally expensive and have been used to simulate film growth up to  $10^4$  monolayers thick and beyond [205-209]. Various kMC models have been employed to study how the growth interface roughens during film deposition [205-214]. Among these models, the most realistic ones incorporate vacancy and void formation but only consider the growth of a single crystal [206-209]. One approach to extend this method to the growth of polycrystalline films is to use multiple lattices to represent different grain orientations. However, this approach is computationally expensive and has not been successful at simulating film growth over a reasonable time scale [215-218]. Bruschi and co-workers used a quasi-continuous coordinate system, such that the simulated film was represented by a two-dimensional array of square cells with the exact positions of the atoms within each cell represented by a continuous x-y coordinate system [215]. While this method allowed different grain orientations to be represented, the simulated films were at most one monolayer thick. Using similar concepts as Bruschi et al., Rubio et al. restricted the positions within each cell to those commensurate with ten possible sublattices [217]. However, their simulated films were less than 50 monolayers thick. Huang and Zhou proposed a memory-efficient method to map multiple lattices onto a single lattice, but even so, their simulated films were less than 100 monolayers thick [216]. Thus, these methods also pose problems for the simulation of nanocrystalline film growth, during which the frequent nucleation of new grains must occur.

A more viable approach to simulate polycrystalline film growth over longer time scales is to incorporate some features of the Q-state Potts model proposed by Srolovitz and co-workers [219, 220]. This method essentially involves prescribing a spin number to each atom that is added to a fixed lattice during deposition. This spin number represents which grain the atom belongs to; nearest-neighbor atoms that possess the same spin number belong to the same grain. Using this approach, the kMC algorithm has been employed by several authors to study polycrystalline film growth; they explored the effects of substrate temperature, deposition rate and incident angle of deposition flux, on

grain morphology and crystallographic orientation of deposited films [221-227]. However, these models suffer from several limitations, such as the unrealistic imposition of an infinite energy barrier for diffusion across grain boundaries [223, 224, 226], deposition times that span less than 100 monolayers [221-227] and restrictions on the number of grains by forbidding new grains to nucleate during the film growth process [221-227]. Additionally, these works either qualitatively treat or completely ignore kinetic roughening and void formation. Even though kinetic roughening, vacancy entrapment, grain nucleation and grain evolution all occur during nanostructured film growth, to our knowledge, there is no model that incorporates all these phenomena over an appreciable thickness.

The purpose of this study is to take some steps towards addressing the issues outlined above in a kMC model of nanocrystalline film growth. We do not aim to simulate any specific deposition process, nor a specific material; our main objective here is to develop a reasonable schematic model that permits study of the basic mechanisms that lead to nanostructure formation during film growth. It is hoped that with improved understanding of the factors that control grain size in nanocrystalline deposits in general, future modeling efforts may focus more effectively on details specific to a given material and process. The model used here includes diffusion, permits voids and vacancies to form, and also allows new grains to nucleate and grow during the film growth process; it can access film thicknesses that comprise many nano-scale grains through the thickness. Thus, the interplay between kinetic roughening, void formation and grain evolution can be analyzed.

## ***A.2. Model***

KMC simulations are performed in (1+1) dimension using a close-packed (hexagonal) lattice as the simulation grid. Each lattice site can either be unoccupied, or occupied by a single atom that is also assigned a grain number corresponding to its grain identity. In the initial configuration, the substrate comprises a row of  $L$  atoms of the same grain number, which are locked into position and unable to change their grain numbers. Figure A.1 shows a schematic of a growing film, where growth occurs in the  $y$

direction. Periodic boundary conditions are imposed in the  $x$ -direction, which is parallel to the substrate.

The simulation involves three basic types of events:

- (i) deposition: a new atom is added onto the lattice,
- (ii) diffusion: a single atom hops to an adjacent vacant lattice site while retaining its grain number, and
- (iii) grain boundary switching: a grain boundary atom switches its grain number without changing its location.

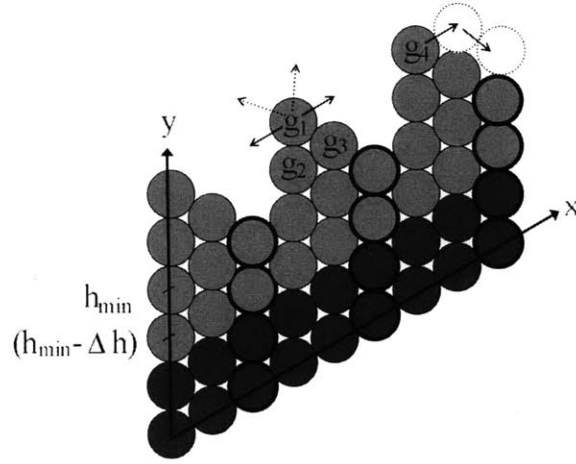


**Figure A.1** A schematic diagram of the close-packed lattice and coordinate system used to simulate film growth. Deposition occurs in  $-y$  direction. Light grey atoms belong to the process zone; dark grey atoms belong to the bulk. Atoms in the lowest columns are outlined in bold. The atom labeled ' $g_1$ ' is allowed to hop in directions indicated by solid arrows; dashed arrows represent forbidden hops. Atom ' $g_1$ ' can also switch its grain number to  $g_2$  or  $g_3$ . Interlayer transport of atom  $g_4$  occurs if it carries out two successive jumps, as indicated by the solid arrows. The first jump results in a net loss of one bond and brings the atom to an activated state.

Atoms are deposited onto the surface of the growing film along the close-packed direction denoted ' $y$ ' in Figure A.1, using a random solid-on-solid deposition rule [228]. Each new atom is assigned a unique grain number, so that every atom can form the nucleus of a new grain. These deposition events occur at a fixed interval of real time, so as to simulate a constant deposition rate. By defining the height of each column,  $h$ , as the ' $y$ ' value of its topmost occupied site, each deposition event causes the height of the chosen lattice column to increase by one unit. Therefore,  $h(x,t)$  is a discrete function that describes the growing surface at time,  $t$ .

Between deposition events, the kMC algorithm is used to implement diffusion and grain boundary switching events [229, 230]. During diffusion, each atom can hop to a

vacant nearest neighbor lattice site while retaining its grain number. However, hops that lead to desorption are not allowed, i.e. an atom must retain at least one nearest neighbor atom after the jump. As an illustration, in Figure A.1, the atom with grain number  $g_1$  can only hop to two of the four vacant sites, because if it were to perform the hops indicated by dashed arrows, it would not have any nearest neighbor atoms around it after the hop. The rate of a diffusion event, where an atom changes from state  $i$  to state  $f$ , is given by  $r_{i \rightarrow f} = k_0 \exp(-\Delta E^{diff} / k_B T)$ , where  $k_B$  is Boltzmann's constant,  $T$  is absolute temperature,  $k_0 = k_B T / h'$  is the vibration frequency of an atom,  $h'$  is Planck's constant and  $\Delta E^{diff}$  is the activation energy for the corresponding change in state of the atom during diffusion. The activation energy is assigned as  $\Delta E^{diff} = E_{barrier}^{diff} + (E_f - E_i) / 2$ , where  $E_{barrier}^{diff}$  is the energy barrier for diffusion (defined to be positive),  $E_i$  and  $E_f$  are the binding energies at the initial and final states respectively (defined to be negative) [229]. The binding energy of an atom is a function of its local environment and is assumed pair wise-additive and limited to nearest-neighbor interactions. For an atom that is surrounded by  $n_s$  nearest neighbors with the same grain number as itself, and  $n_d$  nearest neighbors with different grain numbers, the binding energy,  $E$ , of that atom is given by  $E = n_s E_s + n_d E_d$ , where  $E_s$  and  $E_d$  represent the bond energies between two atoms that have the same and different grain numbers respectively. We define the difference between  $E_s$  and  $E_d$  as the grain boundary energy per bond, i.e.  $E_{gb} = E_d - E_s$ . Thus, an atom that traverses a grain boundary experiences an additional energy penalty that is proportional to  $E_{gb}$ .

Grain boundary switching involves a grain boundary atom changing its grain number to that of one of its nearest neighbors, while remaining in the same location on the lattice. For example, atom  $g_1$  in Figure A.1 may change its grain number to  $g_2$  or  $g_3$ . The rate of a grain boundary switching event is given by  $r_{i \rightarrow f} = k_0 \exp(-\Delta E^{switch} / k_B T)$ , where  $\Delta E^{switch}$  is the activation energy for the corresponding change in state of the grain boundary atom. The activation energy is assigned  $\Delta E^{switch} = E_{barrier}^{switch} + (E_f - E_i) / 2$ , where  $E_{barrier}^{switch}$  is the energy barrier for grain boundary switching (defined to be positive). In our



model, we assign the same value to  $E_{barrier}^{diff}$  and  $E_{barrier}^{switch}$ . Herein, we will use  $\Delta E$  and  $E_{barrier}$  to denote the activation energy and energy barrier for both diffusion and grain boundary switching.

In experimental film growth settings, there is often an orders-of-magnitude difference in surface vs. bulk atomic kinetic rates, especially for energetic deposition processes, such as those involving pulsed lasers, plasmas, or ion beams, as well as in sputter deposition and electrochemical deposition. In these cases there is enhanced kinetic activity in the upper layers of the film (perhaps spanning some dozens of monolayers) [231-237]; the enhanced kinetics are sometimes due to the naturally lower activation barriers for surface processes, sometimes due to higher local temperatures at the interface, or sometimes due to extrinsic effects, such as from the film/electrolyte interface during electrodeposition. In any case, an important aspect of the present model is the ability to roughly model such situations through the inclusion of a “process zone”, in which the kinetics are allowed to be different from the bulk of the growing film. In this zone, the site-independent energy barrier for diffusion is defined as  $E_{barrier}^{pz}$ , whereas the corresponding parameter in the bulk is represented by  $E_{barrier}^{bulk}$ , where  $E_{barrier}^{bulk} > E_{barrier}^{pz}$ . The process zone is assigned to lie above a prescribed height, which is  $\Delta h$  units below the topmost atom of the lowest lattice column,  $h_{min}$ . In Figure A.1, we show an example to illustrate; the atoms in the lowest lattice columns are circled in bold and all the atoms that lie in the process zone are shaded light grey. Bulk atoms that lie below the process zone are represented by the dark grey atoms. In Figure A.1,  $\Delta h = 1$ . However, in all of the simulations described below,  $\Delta h$  is set at a fixed value of 20.

The kMC algorithm computes a list of all possible diffusion and grain boundary switch events in the process zone and the bulk, and their corresponding rates. For atoms that are surrounded by multiple vacant sites and/or nearest neighbors with different grain numbers, each possible diffusion and/or grain boundary switch is considered as a distinct and separate event; for instance, atom  $g_1$  in Figure A.1 contributes two diffusion and two grain boundary switching events to the list of all possible events. An event is then chosen based on its relative rate. Since all the individual event rates are independent, the residence time for the system is related to the reciprocal of the sum of the rates of all

possible events, and the system time is advanced by this amount after each event. This process of event selection and execution is repeated until the prescribed time interval between deposition events is exhausted, at which point a new atom is deposited and the algorithm continues.

To avoid strong finite-size effects, the system size must be much larger than the effective diffusion length of an atom; we find that for  $L = 500$ , this condition is fulfilled for the conditions employed in this study. For all simulations, the bond energy between atoms with the same grain number is kept at  $E_s = -0.4000$  eV, and the diffusion barrier for surface diffusion in the process zone is  $E_{barrier}^{pz} = 0.5000$  eV. Using the relationship between melting temperature and cohesive energy,  $T_m = E_{coh} / 6$ , where  $E_{coh} = 3E_s$ , we define the normalized temperature as  $T^* = T / T_m$  and the normalized grain boundary energy as  $E_{gb}^* = E_{gb} / E_s$ . The normalized deposition rate,  $D_b^*$ , is given by the ratio of the rate of monolayer coverage,  $D_b$ , and the rate of a characteristic surface diffusion event at  $T^* = 1$ , i.e.  $D_b^* = D_b / [k_B T_m / h \exp(-E_{barrier}^{pz} / k_B T_m)]$ . Simulations are carried out over a range of  $T^*$  between 0.35 and 0.91 and  $D_b^*$  spanning more than two orders of magnitude between  $2.10 \times 10^{-3}$  and 0.84, for a fixed grain boundary energy of  $E_{gb}^* = 0.48$ . The effects of grain boundary energy are studied at  $T^* = 0.43$  and 0.78 with three different values of  $E_{gb}^*$ : 0.48, 0.24 and 0.12.

We have conducted two different sets of simulations in this paper. In the first set, which may more closely represent thermal deposition techniques,  $E_{barrier}^{bulk}$  is assigned a conservative value of 1.0000 eV; while this is twice the activation barrier for diffusion in the process zone, it still permits activity in the bulk. In the second set, which may more closely relate to energetic deposition processes, we take  $E_{barrier}^{bulk} \rightarrow \infty$ ; that is, bulk diffusion is suppressed, and all atomic activity is relegated to the process zone.

## A.2. Steady-state microstructure

All our simulated films exhibit microstructural defects: rough surfaces, bulk vacancies and grain boundaries. In this section, we investigate the time evolution of these defects and confirm the existence of a steady-state film microstructure.

Figure A.2 shows typical time evolution plots of (a) surface step height, (b) surface peak spacing, and (c) vacancy content, expressed in units of average monolayer coverage time (ML). The surface step height is defined as  $G(1, t) = \langle |h(x+1, t) - h(x, t)| \rangle$ , where the average is taken over all  $L$  lattice columns, and the peak spacing refers to the average distance along the  $x$  axis between local height maxima. For each layer of the simulated film, we also calculated its grain dimensions along the  $x$  and  $y$  axes, herein referred to as the grain minor and major, respectively. The results are shown in Figure A.2(d) and (e), respectively. Together, these plots illustrate that after an initial period of transient growth, the defect concentrations in our simulated films exhibit a steady-state regime that is characterized by a steady-state step height, peak spacing, vacancy content and grain dimensions.

Interestingly, the above observations are found to be true whether or not bulk diffusion processes are permitted (i.e., with an activation barrier  $E_{barrier}^{bulk} = 1.000$  eV or with  $E_{barrier}^{bulk} \rightarrow \infty$ ). Figure A.2(f) shows the cumulative distribution of the steady-state grain size (circular equivalent diameter) for both sets of conditions; the results are essentially identical at low to moderate temperatures and only exhibit small differences that are still within measurement scatter at high temperatures. The surface features and vacancy contents are also found to be statistically similar for both sets of simulations. From these results we conclude that nanostructure formation in deposited films (at least under the conditions studied here) is principally controlled by activity in the rapid-kinetic “process zone” near the surface. We shall see in later sections that this is indeed true, and that the surface structure plays a determinant role in governing the bulk film microstructure. These results also suggest that the effects of bulk diffusion are relatively insignificant for the conditions of the present simulations; in what follows, then, we do

not differentiate between the two sets of simulations (with  $E_{barrier}^{bulk} = 1.000$  eV vs.  $E_{barrier}^{bulk} \rightarrow \infty$ ), which give the same results.

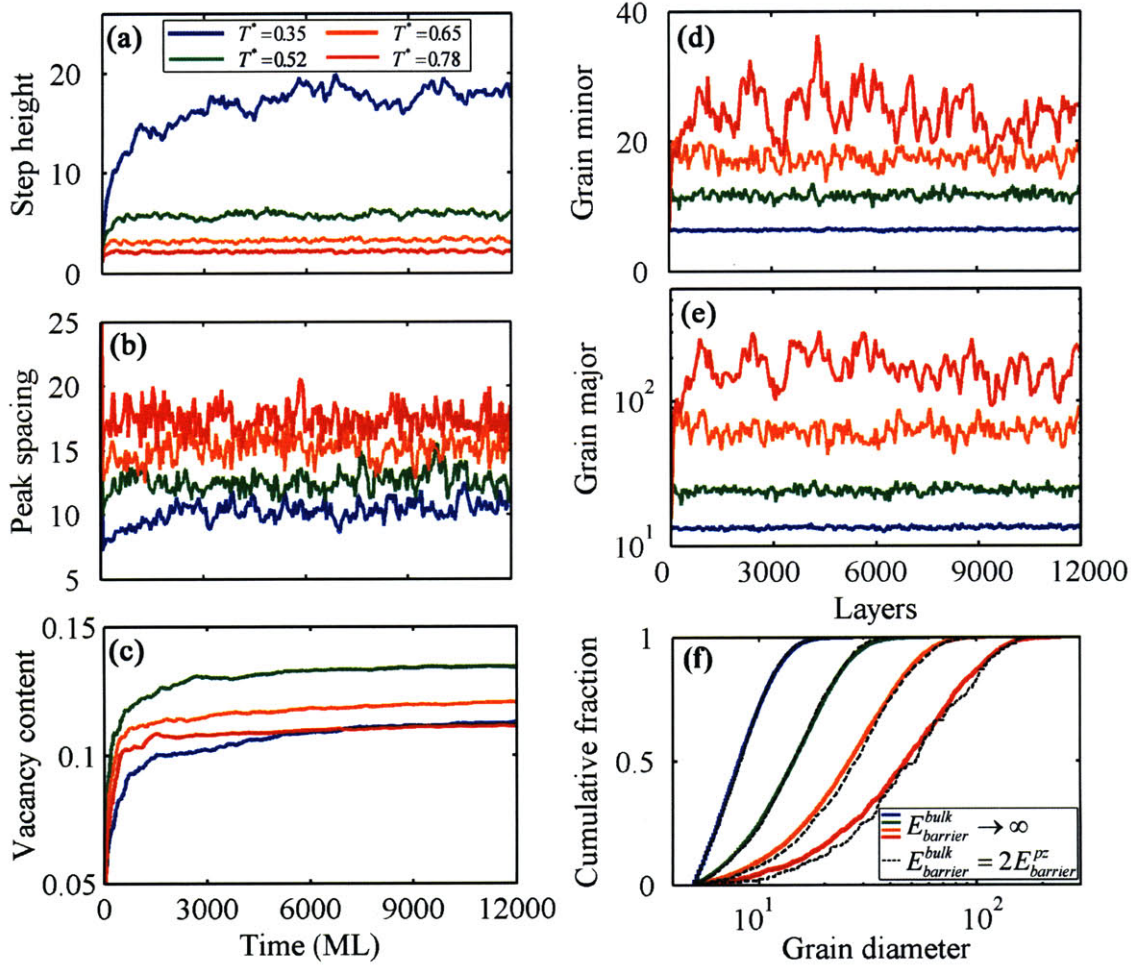


**Figure A.2** Time evolution of (a) surface step height, (b) surface peak spacing and (c) vacancy content of films deposited at a rate of 0.252 when diffusion is restricted to the process zone. Average dimensions of the grains found in each layer of these films are shown in (d) and (e). Cumulative grain size distribution plots are shown in (f), where the dashed lines represent results obtained when bulk diffusion is permitted.

These results in parts (a)-(c) of Figure A.2 are in good agreement with the work of Schimschak and Krug, where a surface diffusion model was used and the simulated films also exhibited steady-state step heights and vacancy contents [208]; the present results further confirm that the grain structure reaches a steady-state on roughly the same timescale as these other features of the microstructure. Typical steady-state microstructures of our simulated films are shown in Figures A.3 and A.4.



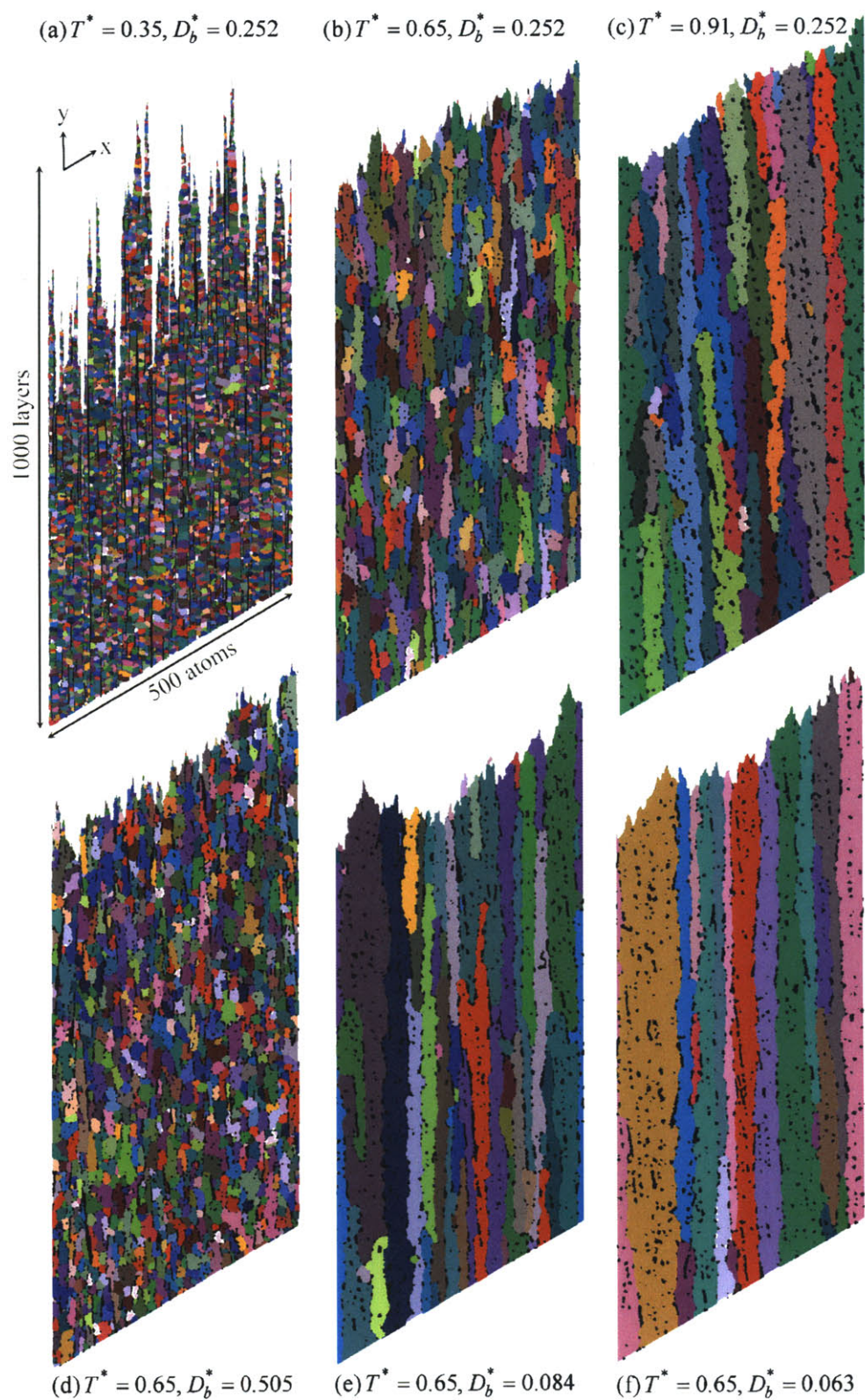


**Figure A.3** Microstructures of deposited films with fixed grain boundary energy of 0.48. Images (a)-(c) show films deposited at different temperatures at a fixed deposition rate of 0.252. Images (d)-(e) illustrate films grown at different deposition rates at a constant temperature of 0.65. Only the top 1000 layers are shown.

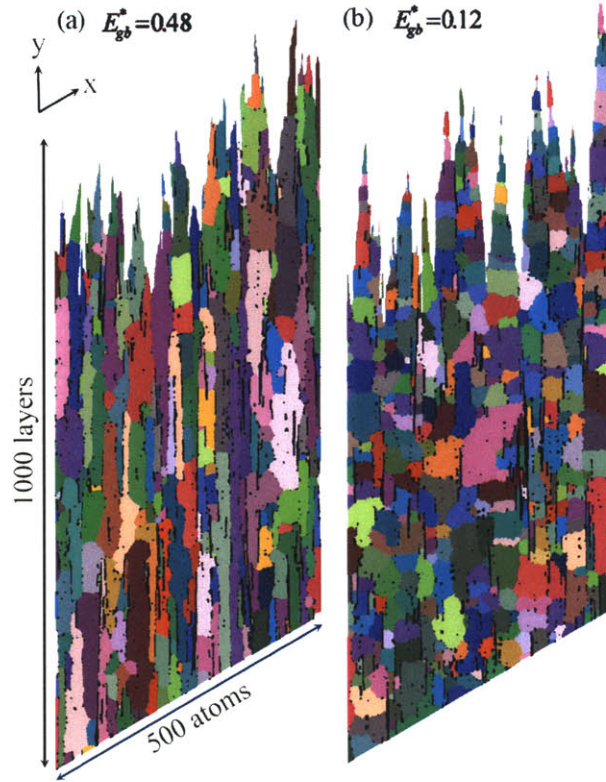


**Figure A.4** Microstructures of films with different grain boundary energies; these films are deposited at a temperature of 0.43 and deposition rate of 0.025. Only the top 1000 layers are shown.

Approximately 1000 monolayers are shown in these figures, where the lattice sites are color-coded according to their grain numbers and vacancies that are trapped in the bulk are colored black. Figures A.3(a)-(c) show the effects of temperature, Figures A.3(d)-(f) illustrate the effects of deposition rate, and Figures A.4(a)-(b) highlight the effects of grain boundary energies. From Figures A.2-A.4 it is clear that deposition conditions dramatically impact the steady-state film microstructure; a more quantitative treatment is presented in what follows. Because of the complex intertwined relationships among the different types of defects (surface morphology, vacancies and grain boundaries), we begin by systematically investigating factors controlling surface morphology and vacancy content. As we shall see later, both of these factors in turn affect the grain structure.



### A.3. Surface morphology

Figure A.5 summarizes the effects of deposition conditions on the steady state step height,  $G(1,t)$ . While the effect of deposition rate is quite minimal (a decade change in rate yields a change in step height on the order of one atom), temperature has a determinant role on the steady-state step height (doubling temperature yields an order-of-magnitude decrease in step height). Figure A.5 also suggests that under most deposition conditions, grain boundary energy does not significantly affect step height, except at high deposition rates and low temperatures, where lower grain boundary energy results in a higher step height.

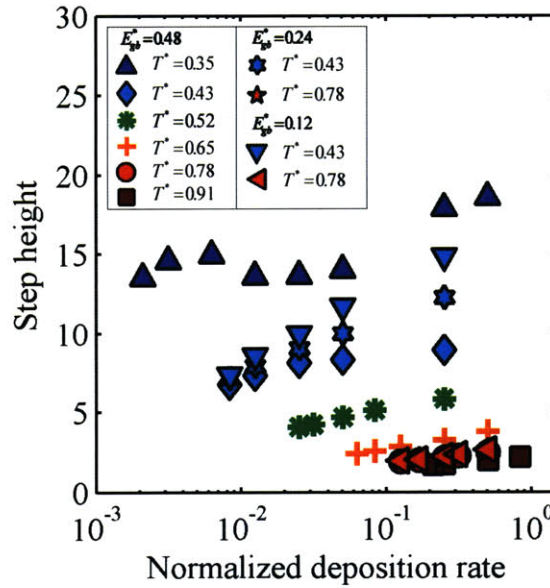


**Figure A.5** Steady-state step height vs. deposition rate of films deposited at different temperatures and grain boundary energies.

The above results can be rationalized through comparison with the work of Schimschak and Krug, who developed a model to investigate surface roughening during epitaxial growth [208]. They employed a square lattice and their model incorporated random deposition and isotropic surface diffusion. Surface diffusion was restricted to singly-coordinated atoms and the number of diffusion trials per mobile surface atom was explicitly fixed for each simulation. If a selected singly-bonded surface atom had a vacant nearest neighbor site, the atom would hop to that empty site with unit probability. However, if it did not have any vacant nearest neighbor but had a vacant next-nearest

neighbor, the atom would hop to that empty site with probability  $\exp(-E_{step})$ , where  $E_{step}$  denotes the Schwoebel-type step-edge energy barrier. The authors observed that as they increased the number of diffusion trials per surface atom from 200 to 800, which translates into a four-fold decrease in deposition rate, the steady-state step height decreased from about 0.90 to 0.56. This observation is broadly in line with ours, where decreasing the deposition rate by an order of magnitude causes the step height to decrease by about 1.

Even though our model does not explicitly incorporate the Schwoebel-type step-edge barrier, the effects of decreasing  $E_{step}$  on step height in Schimschak and Krug's study are qualitatively and quantitatively similar to those of increasing temperature in our study. Figures A.2 and A.3 (a)-(c) show that as temperature increases, the surface morphologies of our films transition from tall pointed peaks to shorter, more rounded ones; quantitatively, this translates into a decrease in steady state step height from  $\sim 16$  to  $\sim 2$ . In Schimschak and Krug's study, as  $E_{step}$  decreased from 3 to 0, a similar morphological transition was observed and the step heights decreased from  $\sim 10$  to  $\sim 1$ . Schimschak and Krug suggested that such differences in surface morphologies could be attributed to the effects of the step-edge barrier in restricting interlayer diffusion and preventing the formation of overhangs, thus causing pointed peaks to dominate the surface morphology as  $E_{step}$  increased.

In the present model, the basic process of interlayer transport is illustrated by the atom labeled  $g_4$  in Figure A.1. Unlike the square-lattice model of Schimschak and Krug [208], on our hexagonal lattice interlayer transport does not require a next-nearest neighbor hop. Rather, atom  $g_4$  traverses a step through two successive jumps, where the first involves a net loss of one bond and results in an overhang formation. To a good approximation, the entire two-step process of interlayer transport may be considered as an activated event with a barrier corresponding to the lost energy of the broken bond. Thus, relative to an average diffusion event that involves no energy bias, its probability is  $\exp(-E_{bond}/2k_B T)$ , where  $E_{bond}$  is the average bond energy; we may thus approximate  $E_{step}^{eff} = E_{bond}/2k_B T$  as the effective Schwoebel-type step-edge barrier in our model.



Using  $E_{bond} = -0.4000 \text{ eV}$ , the bulk bond energy used in our simulations, we computed  $E_{step}^{eff}$  at different temperatures. These results, together with the range of steady-state step height values obtained at each temperature, are presented in Figure A.6. Also shown in Figure A.6 are the results obtained by Schimschak and Krug [208], which are consistent with ours; this supports our interpretation that a Schwoebel-type step-edge barrier implicitly operates in our model. Therefore, the trend observed in Figure A.5 where step height increases as temperature decreases, can be attributed to the corresponding increase in  $E_{step}^{eff}$ , which restricts overhang formation and interlayer transport. The relatively weak dependence of surface step height upon deposition rate (Figure. A.5) also then follows, since its effect on the rate of interlayer transport is through the linear pre-exponential attempt frequency, as compared to the exponential effect of temperature. Grain boundary energy affects step height by altering  $E_{bond}$ , where lower grain boundary energy results in higher  $E_{bond}$ ; this effect becomes dominant at low temperature and when the fraction of grain boundary bonds is high (i.e. high deposition rates).

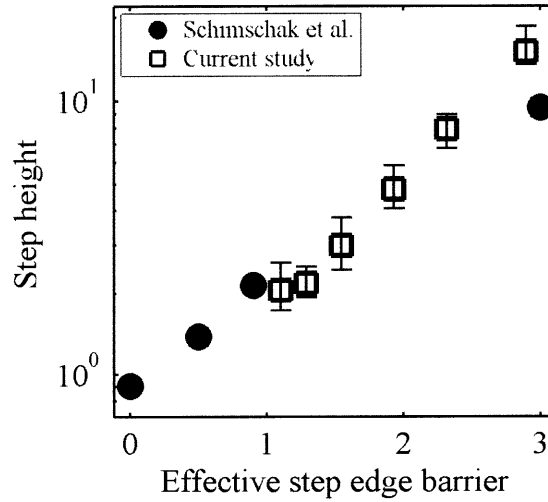


**Figure A.6** Steady state step height vs. effective Schwoebel-type step edge barrier of films deposited at different temperatures. Also shown are data obtained from ref. [208].

Figure A.7 summarizes the effects of deposition conditions on peak spacing: peak spacing increases when deposition rate decreases, temperature increases and grain boundary energy decreases. Across the range of temperatures and grain boundary energies examined, decreasing deposition rate by an order of magnitude causes the peak

spacing to approximately double. At a constant normalized deposition rate of 0.252, increasing the temperature from 0.35 to 0.91 causes the peak spacing to double from ~10 to ~20. Since decreasing deposition rate and increasing temperature allow more diffusion events to occur, Figure A.7 suggests that peak spacing is primarily diffusion-controlled, and may be indicative of the characteristic diffusion length of the atoms during the initial stages of film growth, as postulated by Schimschak and Krug [208]. Figure A.7 also presents an interesting relationship between grain boundary energy and peak spacing, where decreasing  $E_{gb}^*$  from 0.48 to 0.12 causes the peak spacing to increase subtly but consistently; this effect is stronger at low temperatures, where the maximum increase in peak spacing is about 30%.

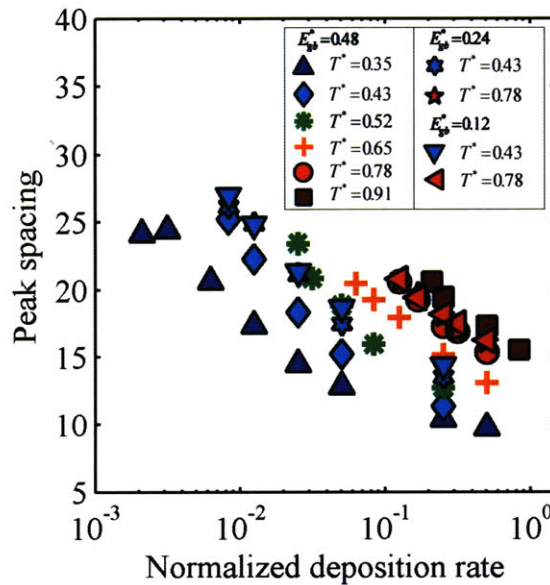


**Figure A.7** Steady-state peak spacing vs. deposition rate of films deposited at different temperatures and grain boundary energies.

#### **A.4. Bulk nanostructure of the deposits**

The bulk features of the deposited films, well below the process zone, involve vacancies (and agglomerations thereof) and grain structures. We discuss these features, their original genesis in the process zone, as well as their inter-relations, in the following.

#### A.4.1. Vacancy incorporation

Figure A.8 summarizes the effects of deposition conditions on the steady state vacancy content. Except at  $T^* = 0.35$ , vacancy content increases predictably and quickly as deposition rate increases. Diffusion has a dual role in vacancy generation and annihilation. In the limiting case where there is negligible diffusion (i.e. high deposition rate), the film is expected to exhibit zero vacancy content since deposition does not create vacancies. In the other extreme scenario, infinite diffusion also results in extremely low bulk porosity, because excess (non-equilibrium) vacancies would tend to be healed by diffusion. In the present simulations, the situation is intermediate; with limited diffusion, overhang and void formation occurs via non-volume-conserving diffusion events, and only a fraction of these vacancies are healed by volume-conserving diffusion events [208]. Thus, the resulting vacancy content depends on the competing effects between these two types of diffusion events. For most of the conditions employed in this study, increasing deposition rate decreases the ratio of volume-conserving to non-volume-conserving diffusion events, thus causing the vacancy content to increase. The anomalous inflection observed at  $T^* = 0.35$  is attributed to the relatively low rate of defect-forming diffusion events at very high deposition rate.

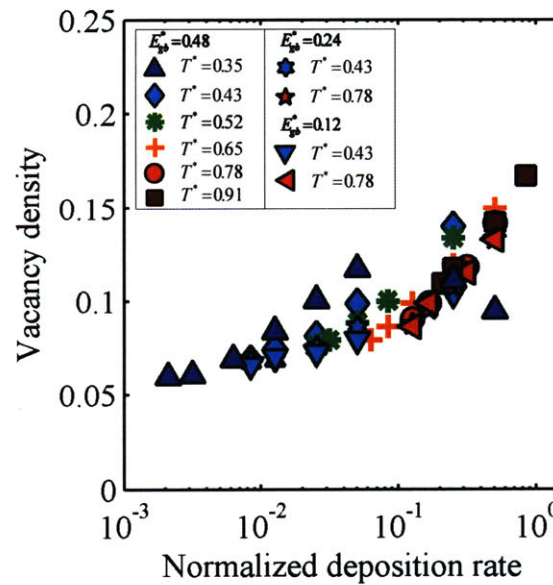


Figure A.8 Steady state vacancy density vs. deposition rate of films deposited at different temperatures and grain boundary energies.

That non-volume conserving diffusion events lead to formation of overhangs and voids implies that void morphology is intimately related to the surface profile of the growing film. Figures A.3 and A.4 qualitatively show that films that exhibit steep step heights also exhibit elongated voids (c.f. Figure A.3(a) and A.4), whereas films with smoother surfaces contain voids that are more equiaxed (c.f. Figure A.3(c)). Despite the close relationship between surface morphology and void structures, they exhibit quite different dependencies on deposition conditions. Whereas the surface step height is essentially independent of deposition rate and dependent only on temperature (Figure A.5), vacancy content is dependent primarily upon rate (Figure A.8). As we will see in the following section, vacancy content has important implications for the evolution of the grain structure.

#### ***A.4.2. Grain nucleation mechanism***

The above analyses on surface morphology and vacancy content are broadly in line with prior surface diffusion deposition models that do not incorporate grain structure. Of more interest in this study is the fact that the grain structure that evolves in deposited films is directly related to the surface morphology and vacancy content, since new grains form on the surface and their growth in the bulk is affected by vacancies. This can be quickly appreciated by examining supplementary movies 1-2 [85] and Figures A.9-A.10. These figures highlight a principal finding of our work: the nucleation of new grains during deposition occurs essentially exclusively atop surface peaks.

A typical example showing the birth and growth of a new grain is denoted by a blue ellipse in Figure A.9(a); this nucleus continues to grow in the vertical direction (cf. Figures A.9(b)-(e)) until its further growth is inhibited by the nucleation of a new grain above it (cf. Figure A.9(f)). The red ellipses in Figures A.9(c)-(e) illustrate another example of vertical grain growth being interrupted by subsequent grain nucleation events on a surface peak (cf. Figure A.9(e)). Additionally, the red ellipses in Figures A.9(f)-(h) illustrate a typical example of grain growth in the lateral direction, which appears limited by peak separation. In other words, grains initially develop independently of one another on separate peaks, and become lateral neighbors by growing into mutual contact.



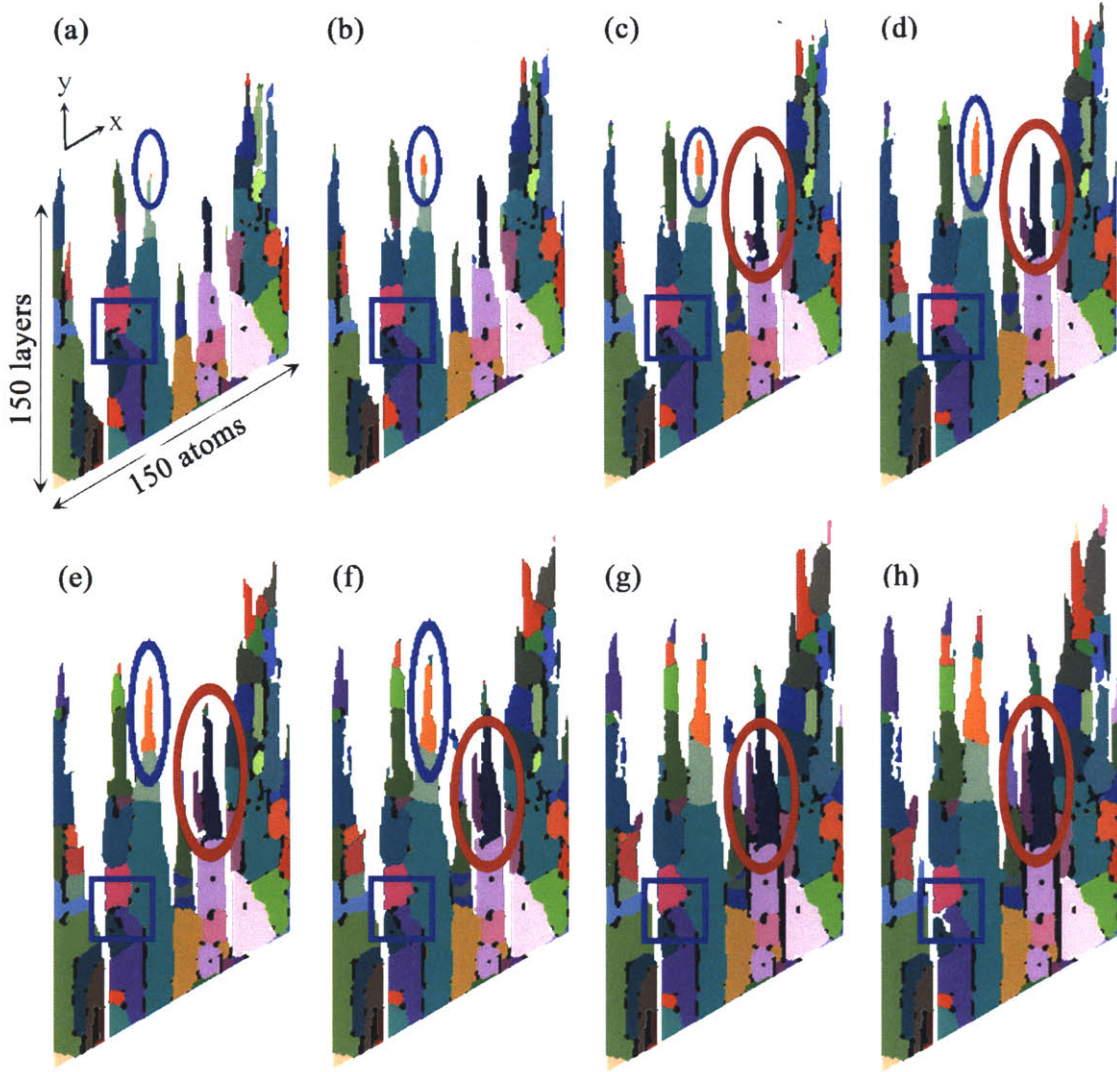


Figure A.9 Snapshots of the film growth process at  $T^* = 0.43$ ,  $D_b^* = 0.051$  and  $E_{gb}^* = 0.48$ ; these images are taken at a time interval of 10 ML. Notice that grains nucleate preferentially on surface peaks (see solid blue ellipses in (a)-(f) and red ellipses in (c)-(e)). Grain growth in lateral direction appears limited by peak spacing (see red ellipses in (e)-(h)). Regions enclosed in blue boxes in (a)-(h) illustrate grain boundary migration until the grain boundaries are pinned by voids.

Within the bulk, grains continue to change their size and shape in more subtle ways. Generally, we observe some grain boundary motion shortly after grains impinge, but grain boundary migration is usually arrested soon after, once the grain boundaries encounter voids and become pinned; an example of this is illustrated by the regions enclosed in the blue boxes in Figures A.9(a)-(h)). This stagnation of grain boundary migration happens very early in the life of a grain, usually when it is still located within

the process zone (as for the example in Figure A.9). Of course, once the grains enter the bulk region, the kinetics of structure evolution is further slowed.

The images in Figure A.9 are also complemented by those in Figure A.10, which show many of the same features, but for a higher deposition temperature with a correspondingly smoother surface. The same basic mechanisms are observed here: grains nucleate on surface peaks; their height (grain major) is principally governed by the likelihood that a new grain forms atop them, while their width (grain minor) is governed by the spacing of peaks and lateral pinning by strings of vacancies and voids. In what follows, we present a quantitative analysis of the factors governing grain evolution, separately examining the minor and major axes of the grain structure.

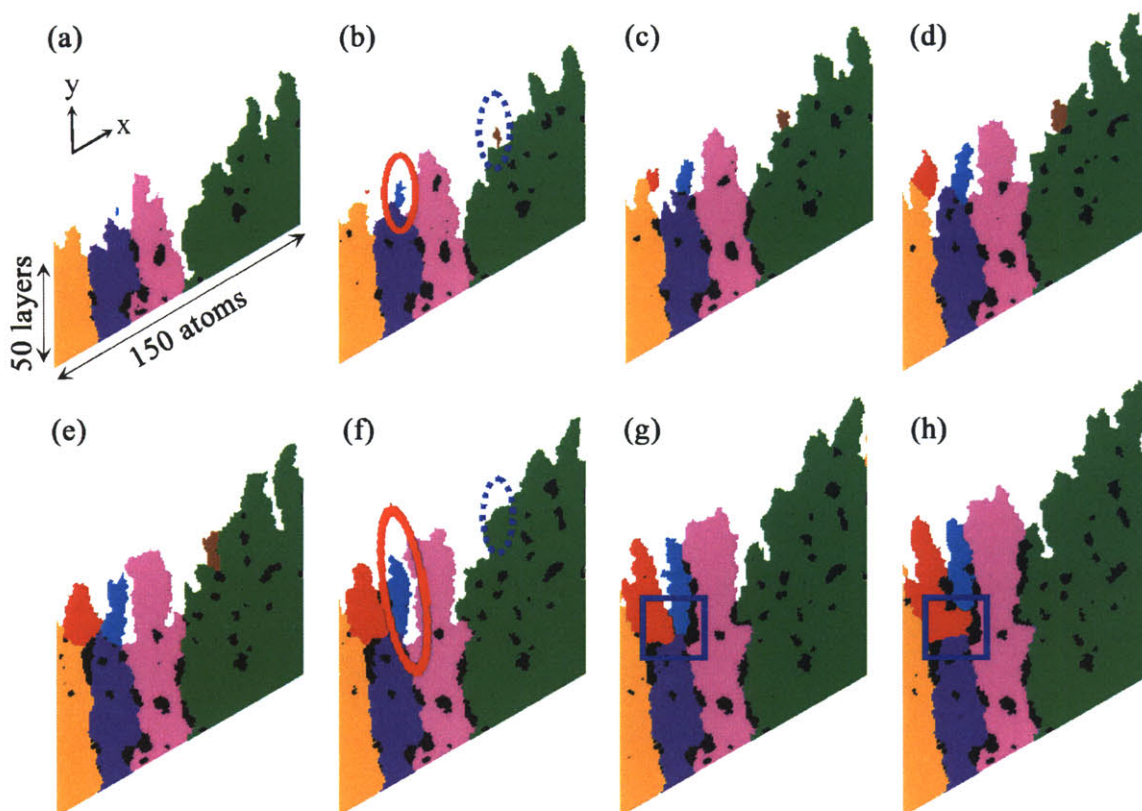


Figure A.10 Snapshots of the film growth process at  $T^* = 0.78$ ,  $D_b^* = 0.126$  and  $E_{gb}^* = 0.48$ ; these images are taken at a time interval of 10 ML. The solid red ellipse in (b) shows a nucleus that eventually grows into a grain; this nucleus forms a triple point with nearby grains in (d). The dashed blue ellipse in (b) shows a nucleus that is eventually eliminated in (f). Regions enclosed in blue boxes in (g)-(h) illustrate grain boundary migration until the grain boundaries are pinned by voids.



#### A.4.3. Factors controlling grain dimensions

Figures A.11(a) and (b) show that increasing temperature and decreasing deposition rate cause both grain minor and major to increase; such trends are generally consistent with experimental observations [238-248]. One plausible explanation for these trends is that increasing temperature and decreasing deposition rate correspond to more time-at-temperature, promoting more grain boundary migration. However, Figures A.11(a) and (b) also show that decreasing grain boundary energy has an opposite effect on grain major and minor dimensions, despite the fact that this change lowers the driving force for grain growth, reduces grain boundary migration, and should simultaneously reduce both grain dimensions. Thus, consistent with the qualitative results shown in Figure A.9, Figure A.11 presents quantitative evidence that grain minor and major are principally governed by different factors, and that grain minor is not primarily controlled by the rate of grain boundary migration, which is the case for conventional grain growth.

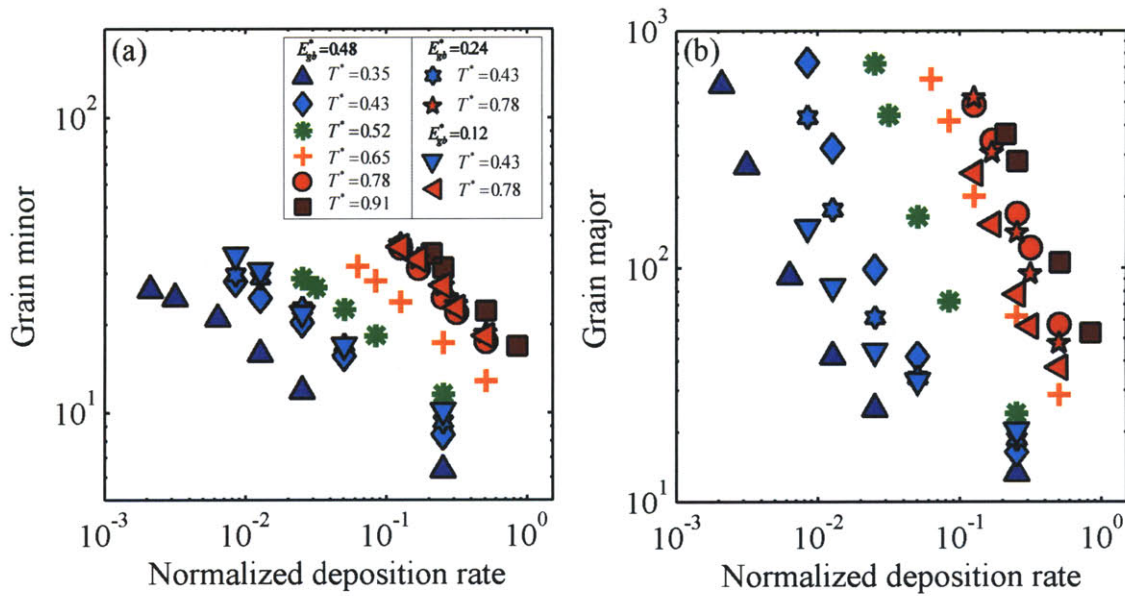
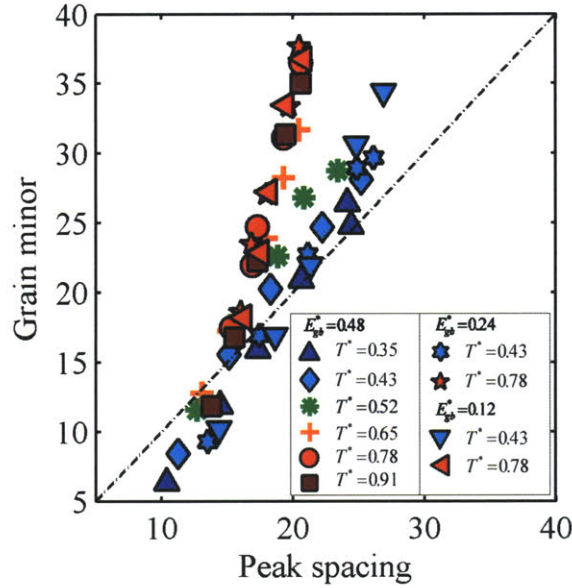


Figure A.11 Average (a) grain minor and (b) grain major vs. deposition rate of films deposited at different temperatures and grain boundary energies.

Instead, the trends on grain minor may be understood by revisiting the implications of supplementary movies 1-2 and Figures A.9-A.10: because new grains nucleate principally on top of surface peaks, there is a consistent correspondence between valley positions and grain boundary regions, as can also be appreciated from Figures A.3

and A.4. That grain minor is intimately related to surface morphology is borne out in Figure A.12, which shows grain minor plotted against mean peak spacing for the simulated films. An approximate linear relationship is consistently observed for each series of simulations (although the slope is a function of temperature). Figure A.12 also helps to explain why grain minor increases as grain boundary energy decreases (as this causes an increase in the peak spacing).



**Figure A.12 Relationship between peak spacing and grain minor of films deposited under various conditions. The dashed line represents a 1:1 relationship.**

Grain major, on the other hand, appears to be primarily dictated by the rate of grain nucleation atop the surface grains. Because each freshly deposited atom is randomly assigned a grain number, each deposition event constitutes an opportunity to nucleate a new grain. That new grains tend to nucleate on peaks is intuitively reasonable, since freshly-deposited atoms are less likely to switch their grain numbers and join a pre-existing grain if they are poorly coordinated by atoms of the pre-existing grain. Such atoms can then form nuclei for new grain formation. Consider the case where an existing grain with grain number  $g_1$  is located at a surface peak. When a freshly-deposited atom of grain number  $g_2$  lands on top of the peak, a  $g_1$ - $g_2$  grain boundary bond is formed. The driving force for the new atom to switch its grain number from  $g_2$  to  $g_1$  depends on the grain boundary energy, and the activation energy for such a switch event is given by  $\Delta E = E_{barrier}^{pz} - E_{gb} / 2$ . If this switch event occurs, the new atom is assimilated into



grain  $g_1$  and no grain nucleation occurs. Even though such a switch event is always thermodynamically favorable, it can be kinetically avoided depending upon the deposition rate. More specifically, if another new atom of grain number  $g_3$  is added on top of the atom of grain number  $g_2$ , the topmost atom may join grain  $g_2$ . When this happens, the  $g_2$  atom that is in contact with grain  $g_1$  has a  $g_2$ - $g_2$  bond, in addition to the  $g_1$ - $g_2$  grain boundary bond. Because a switch event that converts the  $g_1$ - $g_2$  grain boundary bond to a  $g_1$ - $g_1$  bond would occur at the expense of converting the  $g_2$ - $g_2$  bond into a  $g_1$ - $g_2$  grain boundary bond, there is no net change in the number of grain boundary bonds for such a switch event. Thus, the activation energy for grain boundary switching of the two-atom grain nucleus is  $\Delta E = E_{barrier}^{pz}$ , which is higher than that of the one-atom grain nucleus. Therefore, a grain nucleus of two atoms is significantly less likely to be assimilated into pre-existing grains than a one-atom nucleus.

Thus, we view the nucleation of new grains as a kinetic competition between switching events that assimilate freshly-deposited atoms into the existing grain structure (with a rate proportional to  $k_0 \exp(-(E_{barrier}^{pz} - E_{gb}/2)/k_B T)$ ), and the local clustering of new atoms into incipient grain nuclei (with a rate governed by the addition of new atoms, and thus proportional to  $\dot{D}_b$ , the rate of monolayer coverage). Assuming that the grain major is primarily governed by the rate at which new grains nucleate on top of pre-existing grains and neglecting the effects of subsequent grain boundary migration on the grain major, this grain nucleation model suggests that the grain major is related to the normalized switch rate, which we define as  $[k_0 \exp(-(E_{barrier}^{pz} - E_{gb}/2)/k_B T)]/\dot{D}_b$ . Figure A.13 shows the average grain major as a function of the normalized switch rate for our simulations. That the data collapses reasonably well onto a single curve supports our view of grain major being limited by the nucleation rate for new grains on the top of surface peaks.

The data collapse in Figure A.13 is especially good at lower normalized temperatures, between 0.35 and 0.52, where we also observe that the relationship between grain minor and peak spacing is close to a 1:1 correspondence (cf. Figure A.12). In this low temperature regime, each surface grain is clearly defined by a peak (cf. Figures A.3(a) and A.4). Recall from Figure A.5 that this is also the temperature range

where films exhibit steep step heights greater than  $\sim 4\text{-}5$  atomic distances. Because the peaks are tall and separated, grains on each peak are isolated from those on neighboring peaks and thus, they evolve independently and peak spacing corresponds to the grain width. It is likely also significant that in this case, the grains within each peak form into a bamboo structure with grain boundaries normal to the growth direction. Such a structure is stable against coarsening (low boundary curvature), and therefore promotes the retention of a nanoscale structure.

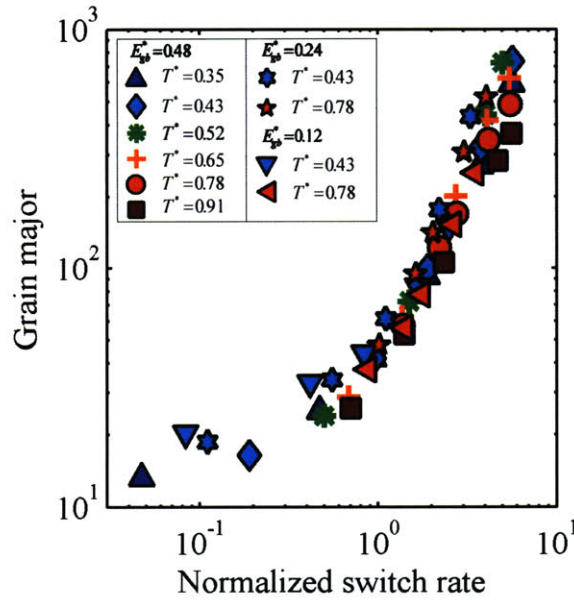


**Figure A.13 Relationship between grain major and normalized switch rate of films deposited under various conditions.**

At higher normalized temperatures above 0.52, the grain minor often exceeds the peak spacing (cf. Figure A.12) and the data collapse in Figure A.13 is less convincing, with a temperature dependence appearing to spread the data points. This is because at these temperatures, the surface exhibits a smoother and more nodular structure, instead of tall pointed peaks (cf. Figures A.3 and A.10). Because of the gentler step height and peak slope, the peaks communicate more readily with one another and do not evolve independently as they do at lower temperatures. Consequently, some grain widths span multiple peaks, as seen in Figures A.3(e), (f) and A.10. Despite the different surface morphology, grains are still found to nucleate in the same basic way, i.e., nucleation events still occur preferentially on surface peaks. However, supplementary movie 2 and Figure A.10 show that in these cases there is an additional factor that affects the stability

of these grain nuclei. Specifically, nuclei located on peaks nearer the lateral edge of a grain, i.e., in close proximity to adjacent grains, are more stable against elimination than those that form in the center of a pre-existing grain. Compare, for example, the nucleus enclosed in the solid red ellipse with the one enclosed in dashed blue in Figure A.10(b). This additional stability of such edge-nuclei arises because shortly after they form atop a first grain, film growth brings them into lateral contact with a second grain, forming a triple junction. This stabilizes the nucleus by setting up a local kinetic competition; a nucleus connected to only one grain experiences switch events at a higher rate than when it is abutted by two. Therefore, as temperature increases and the surface becomes composed of smaller and gentler peaks that are spanned by individual grains, more nuclei survive through this additional mechanism, and the grain major decreases for the same normalized switch rates, as shown in Figure A.13.

#### ***A.4.4. Vacancy-grain boundary interactions***

Upon closer inspection, supplementary movies 1-2 and Figures A.9-A.10 (see for example regions enclosed in blue boxes in Figure A.9(a)-(h) and Figure A.10(g)-(h)) also show that vacancies and voids retard grain boundary migration; grain boundaries that are not decorated with voids migrate freely until they encounter some, after which their motion becomes impeded. These observations suggest that because of grain boundary pinning, high vacancy and void contents (i.e. high deposition rates) favor small grains. They also suggest that the state of vacancy incorporation in grain boundaries (or the grain boundary free volume) is principally a dynamical feature of the microstructure. We may verify this by examining the segregation state of the vacancies to grain boundaries.

Defining the vacancy segregation energy as the difference in formation energy of the vacancy at the grain boundary and in the bulk, we obtain positive segregation energies for all grain boundary energies employed in this study. From an energetic standpoint, we thus expect vacancy segregation to be favored in all of our simulations, with higher segregation tendencies as grain boundary energy increases; of course temperature would tend to randomize the vacancy distribution and therefore decrease the segregation tendency. To assess such trends, we use the Gibbsian interfacial excess, defined as  $\left[ N_v^{gb} / N^{gb} - \left( N_v^{bulk} / N^{gb} \right) \left( N^{gb} / N^{bulk} \right) \right]$ , where  $N_v^{gb}$  and  $N_v^{bulk}$  are the number of

vacancies in the grain boundary and grain interior regions, and  $N^{gb}$  and  $N^{bulk}$  are the total number of sites in the grain boundary and grain interior regions, respectively. Although we do not plot the results here, we find that in general the interfacial vacancy excess is a weak function of deposition rate, and increases as temperature and grain boundary energy increase. That interfacial excess increases as grain boundary energy increases is in line with the energetic arguments laid out above. However, the effects of temperature on interfacial excess defy energetic predictions. Such a discrepancy must be attributed to kinetics, and is likely related to the more rapid grain boundary migration at higher temperatures which leads to more interceptions of voids by boundaries.

#### A.4.5. Grain size vs. shape

As a final point, Figure A.14 summarizes an overarching finding of our work, which concurs with experimental findings [239, 249, 250]: as the average grain size (i.e., average circular-equivalent grain diameter) decreases, so does its aspect ratio.

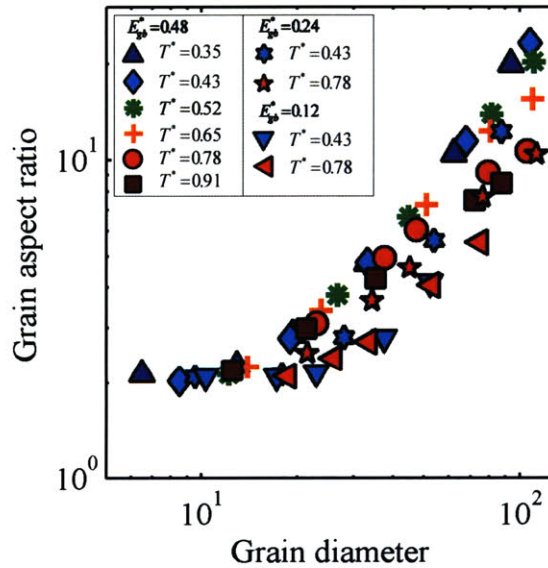


**Figure A.14** Relationship between grain aspect ratio and grain diameter of films deposited under various conditions.

All other things being equal, we find that promoting finer grains through, e.g., more rapid deposition or lower deposition temperature, also promotes more equiaxed structures. Our analysis provides a straightforward explanation of this common observation. The grain minor is largely governed by the surface structure and specifically

the separation of the peaks, both of which are only slightly affected by deposition conditions (e.g., increasing the deposition rate by an order of magnitude reduces the peak spacing by only  $\sim 5$  atomic units (cf. Figure A.7)). On the other hand, the grain major exhibits a much stronger dependence on deposition variables since they directly affect the grain nucleation rate (an order of magnitude increase in deposition rate increases the grain major by almost two orders of magnitude (cf. Figure A.13)). Therefore, changes in the deposition condition that promote finer grains are more strongly manifested in the grain major; grain size and aspect ratio are thus dynamically linked, and nano-scale grains tend to be more equiaxed.

## ***A.5. Conclusions***

We employ a full diffusion kinetic Monte Carlo model to simulate nanocrystalline film deposition. We find, in line with prior simulation works of film deposition, that the surface structure (step height and peak spacing), as well as the vacancy content, achieve a steady-state condition after an initial growth transient. What is more, these features of the film change with temperature and deposition rate in ways consistent with prior models. However, the present work also evaluates the evolution of the grain structure and its dependence on deposition conditions, by associating individual atoms with specific grains and permitting atoms to switch their grain allegiance based on a kinetic law that incorporates a grain boundary energy penalty. Broadly, our conclusions in regard to the grain structure of deposited nanocrystalline films are as follows:

- Like the surface structure and vacancy content, the grain structure of the growing film exhibits a steady-state condition, in which the grain dimensions and aspect ratio remain approximately constant.
- The grain structure of the film is essentially governed by the steady-state surface morphology, because new grain nucleation occurs exclusively on surface peaks. Thus, bulk nanocrystalline deposits are favored by the presence of nanoscale roughness at the growth surface.
- Nucleation of new grains is viewed as a kinetic competition between the clustering of a few atoms into a new grain at the surface peaks on the one hand, and their incorporation into the grain beneath on the other. When freshly-

deposited atoms cluster with one another rather than join the pre-existing grains of the film below, a new grain can nucleate and form; this condition is facilitated by the low coordination of atoms at surface peaks. At higher temperatures, the surface peaks are small and closely spaced; in this case grain nucleation is facilitated when a nucleus comes into contact with another adjacent grain, forming a triple junction.

- As a result of the nucleation mechanism being relegated to surface peaks, the grain minor dimension (in the plane of the film) is primarily dictated by surface peak spacing, which in turn is reduced at low temperatures and high deposition rates. The grain major dimension (in the growth direction) is related to the probability of nucleating new grains on top of pre-existing ones, with finer grains being formed at low temperatures, high deposition rates and low grain boundary energies. Because vacancies and voids kinetically pin grain boundaries, high vacancy (or free volume) content, which is obtained at high deposition rate, also favors nano-grains.

- Because surface roughening and tighter peak spacing are less easily induced by deposition conditions than grain nucleation events, as grains shrink, they transition from columnar, to elongated, and eventually to equiaxed.

These results provide some initial insight on the kinetic mechanisms by which the grain structure of deposited films may be tuned, and generally support empirical observations common in the experimental literature.

## Appendix B. Effects of current pulses on the ductility of electrodeposited Al alloys<sup>5</sup>

With an eye to alter the grain size and phase distribution of electrodeposited Al-Mn alloys, a variety of current waveforms is employed to alter surface kinetics at the electrode. The current waveforms comprise two unique pulses, as shown in Figures 1.4(b)-(d), where the pulse parameters of the first pulse were kept the same for all waveforms. The current density of the first pulse,  $i_1$ , was assigned the same value as the cathodic current density used during our DC experiments in chapter 2, i.e.  $i_1=6 \text{ mA/cm}^2$ . Since the characteristic length-scale of the domain-network structures observed in the dual-phase DC alloys was postulated to be controlled by the characteristic diffusion length of a surface adatom, the pulse duration was chosen to be  $1/10^{\text{th}}$  the time required for monolayer coverage, in order to reduce the extent of phase segregation, i.e.  $t_1=20 \text{ ms}$ . In the following sections, we present guided bend test results on Al-Mn alloys that were electrodeposited using the waveforms illustrated in Figures 1.4(b)-(d). The bend tests were carried out according to the guidelines described in ASTM E290-97a (2004) and section 2.1. We also show preliminary results on Al-Mn-Ti alloys that were electrodeposited in a different electrolytic solution at a different temperature.

### ***B.1. Effects of pulse current density, $i_2$***

To investigate the effects of varying the current density  $i_2$  on alloy composition, we used waveforms “A”, “B”, “C”, “D”, “E” and “F” to electrodeposit Al-Mn alloys from electrolytic baths containing the same amounts of  $\text{MnCl}_2$ . Table B.1 summarizes the pulse parameters of these six waveforms.

Guided bend tests were carried out on alloys containing about 8 at.% Mn produced by the six waveforms shown in Table B.1; images of the strained surfaces are presented in Figure B.1. Images on the left column correspond to alloys that were strained to ~37%; images on the right column correspond to alloys with an applied tensile

---

<sup>5</sup> Much of the content of this Appendix has been submitted in a patent application [129]

strain of ~13%. Images on the same row belong to alloys that were produced by the same current waveform. The current density  $i_2$  decreases from positive to negative from the topmost to bottommost row. Table B.2 summarizes our observations.

**Table B.1 Pulse parameters of waveforms used to investigate the effects of  $i_2$ .**

Waveform	Pulse current density (mA/cm <sup>2</sup> )		Pulse duration (ms)		Temperature (°C)
	$i_1$	$i_2$	$t_1$	$t_2$	
“A”	6	6	20	20	25
“B”	6	3	20	20	25
“C”	6	1	20	20	25
“D”	6	0	20	20	25
“E”	6	-3	20	20	25
“F”	6	-3.75	20	20	25

Figure B.1 and Table B.2 show that decreasing the magnitude of  $i_2$  causes the ductility of the alloys to increase; whereas the “A” alloys cracked across the sample widths, those produced by most other waveforms did not. For positive values of  $i_2$  (i.e. waveforms “A”, “B” and “C”), decreasing the magnitude of the positive pulse current causes the ductility to increase; whereas the “A” and “B” alloys cracked across the sample width when strained to ~37% and ~13%, cracks did not propagate through the widths of the “C” alloys. Interestingly, for the “D”, “E” and “F” alloys, as  $i_2$  becomes more negative, the ductility of the alloy decreases. When the alloys were strained to ~37%, alloys that were produced by waveform “F”, where  $i_2 = -3.75$  mA/cm<sup>2</sup>, exhibited cracks that were relatively long and wide (~300  $\mu$ m by ~20  $\mu$ m); whereas alloys produced by waveform “D”, where  $i_2 = 0$  mA/cm<sup>2</sup>, showed the smallest cracks (~40  $\mu$ m by ~10  $\mu$ m). When the alloys were strained to ~13%, the “F” alloy exhibited a single crack, whose dimensions are larger than that observed on the “E” alloy. The “D” alloy did not exhibit cracks when the applied strain was ~13%.



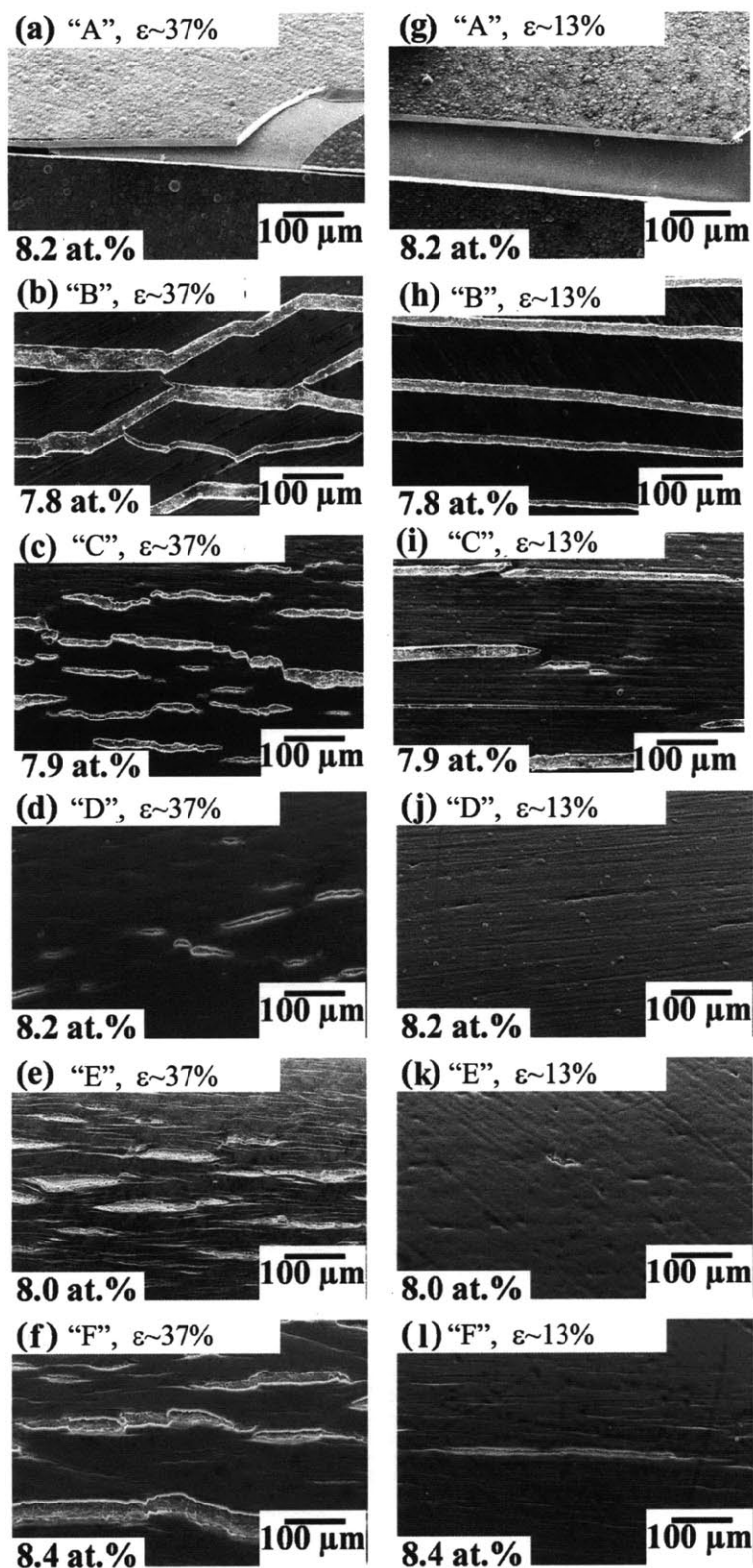


Figure B.1 SEM images of bent surfaces of ~8 at.% Mn alloys produced by different waveforms. Images on the left column correspond to samples that were strained to ~37%. Images on the right correspond to samples that were bent strained to ~13% true strain.  $i_2$  decreases from +6 mA/cm<sup>2</sup> to -3.75 mA/cm<sup>2</sup> from the topmost to bottommost row.

**Table B.2 Dimensions of cracks observed on strained surfaces of alloys containing ~8 at.% Mn after guided bend test, where applied tensile strains are ~37% and ~13%.**

True strain	Waveform	$i_2$ (mA/cm <sup>2</sup> )	Crack length (μm)	Crack width (μm)
~37%	“A”	6	Across whole sample	40-150
	“B”	3	Across whole sample	50
	“C”	1	150	25
	“D”	0	40	10
	“E”	-3	120	13
	“F”	-3.75	300	20
~13%	“A”	6	Across whole sample	100
	“B”	3	Across whole sample	40
	“C”	1	50-300	20
	“D”	0	x	x
	“E”	-3	30	5
	“F”	-3.75	200	5

## ***B.2. Effects of pulse duration, $t_2$***

To investigate the effects of varying the pulse duration  $t_2$  on alloy composition, we used waveforms “A”, “G”, “H” and “E” to electrodeposit alloys from electrolytic baths containing the same amounts of MnCl<sub>2</sub>. Table 5.3 summarizes the pulse parameters for these four waveforms.

**Table B.3 Pulse parameters of waveforms used to investigate the effects of  $t_2$ .**

Waveform	Pulse current density (mA/cm <sup>2</sup> )		Pulse duration (ms)		Temperature (°C)
	$i_1$	$i_2$	$t_1$	$t_2$	
“A”	6	6	20	20	25
“G”	6	-3	20	5	25
“H”	6	-3	20	10	25
“E”	6	-3	20	20	25

Guided bend tests were carried out on alloys containing about 8 at.% Mn produced by the “A”, “G”, “H” and “E” waveforms; images of the strained surfaces are presented in Figure B.2. Images on the left column correspond to alloys that were strained to ~37%; images on the right column correspond to alloys with an applied true strain of ~13%. Images on the same row belong to alloys that were produced by the same

current waveform. The pulse duration  $t_2$  increases from the topmost to bottommost row. Table B.4 summarizes our observations.

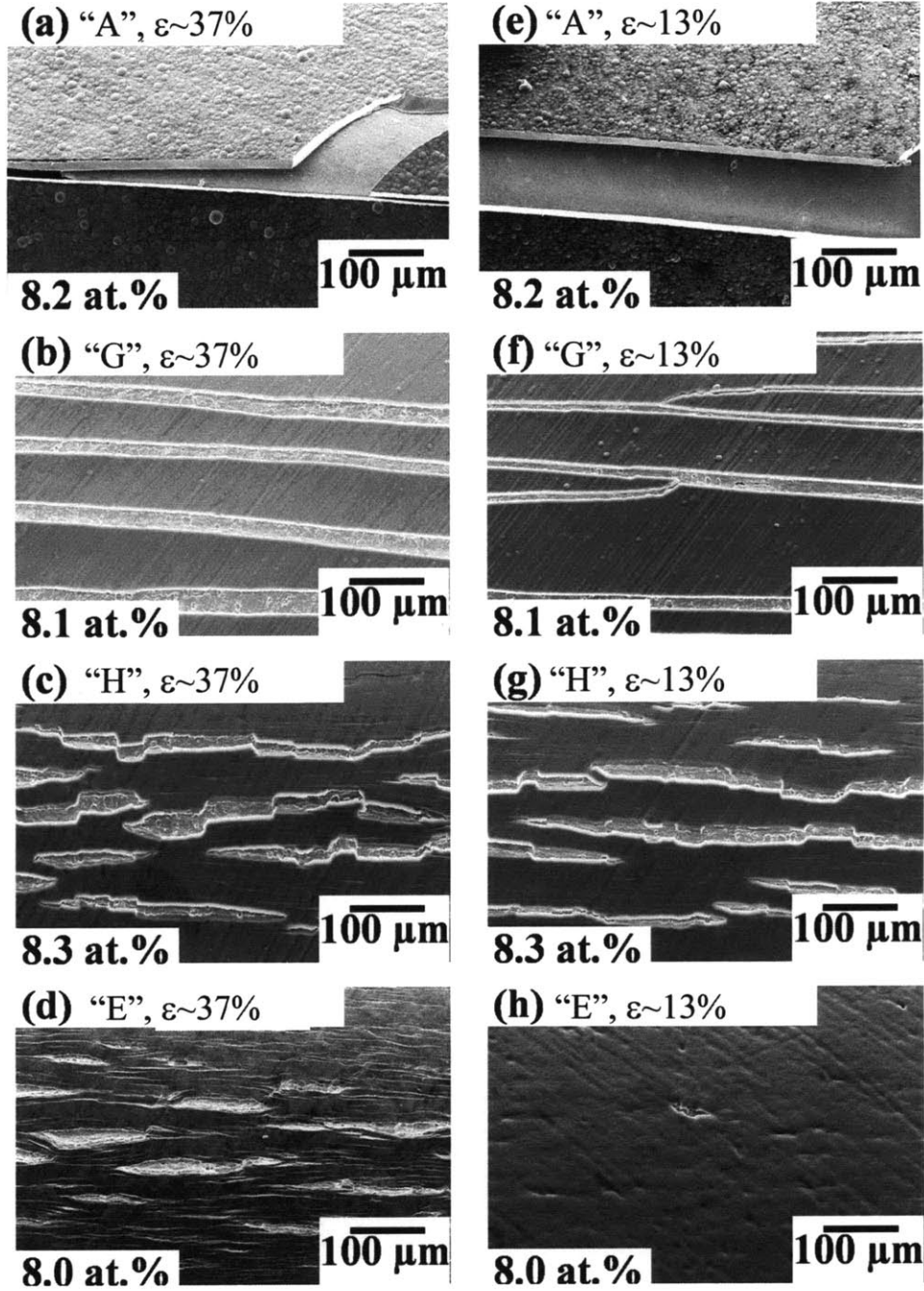


Figure B.2 SEM images of bent surfaces of ~8 at.% Mn alloys produced by waveforms with different  $t_2$ . Images (a)-(d) correspond to samples that were strained to ~37%. Images (e)-(h) correspond to samples that were subject to a tensile strain of ~13%. The pulse duration  $t_2$  increases from 0 to 20 ms from the topmost to bottommost row.

**Table B.4 Dimensions of cracks observed on strained surfaces of alloys containing ~8 at.% Mn after guided bend test, where applied tensile strains are ~37% and ~13%.**

True strain	Waveform	$t_2$ (ms)	Crack length ( $\mu\text{m}$ )	Crack width ( $\mu\text{m}$ )
~37%	“A”	0	Across whole sample	40-150
	“G”	5	Across whole sample	25
	“H”	10	300	20
	“E”	20	120	13
~13%	“A”	0	Across whole sample	100
	“G”	5	Across whole sample	20
	“H”	10	200	25
	“E”	20	30	5

Figure B.2 and Table B.4 show that for the same pulse current density  $i_2$  (i.e.  $-3 \text{ mA/cm}^2$ ), increasing the pulse duration  $t_2$  causes the ductility of the alloys to increase. Both the “A” and “G” alloys ( $t_2 = 0$  and  $5 \text{ ms}$ , respectively) exhibit cracks that propagate across the sample width when the applied tensile strains were ~37% and ~13%. On the other hand, the “H” and “E” alloys did not crack across the entire width of the sample when bent. As  $t_2$  increases from  $10 \text{ ms}$  (waveform “H”) to  $20 \text{ ms}$  (waveform “E”), both the crack length and width decrease.

### ***B.3. Ternary alloy electrodeposited at non-ambient temperature***

Al-Mn-Ti alloys were electrodeposited using the electrolytic bath composition shown in Table B.5. A silicone oil bath was used to maintain the temperature of the electrolyte at  $80^\circ\text{C}$  during the electrodeposition experiments.

**Table B.5 Composition of electrolytic bath used to electrodeposit Al-Mn-Ti alloys.**

Chemical compound	Composition (mols/L)
Aluminum chloride, anhydrous ( $\text{AlCl}_3$ )	6.54
1-ethyl-3-methylimidazolium chloride ([EmIm]Cl)	2.57
Manganese chloride, anhydrous ( $\text{MnCl}_2$ )	0.08
Titanium chloride, anhydrous ( $\text{TiCl}_2$ )	0.04

Two types of waveforms were used to electrodeposit Al-Mn-Ti, namely waveform “I” and “J”. Waveform “I” is direct current, while “J” is a reverse pulse

current waveform. Table B.6 summarizes the pulse parameters of these waveforms, along with the alloy compositions.

**Table B.6 Pulse parameters of waveforms used to electrodeposit Al-Mn-Ti alloys.**

Waveform	Pulse current density (mA/cm <sup>2</sup> )		Pulse duration (ms)		Temperature (°C)	Alloy composition (at. %)	
	$i_1$	$i_2$	$t_1$	$t_2$		Mn	Ti
“T”	6	6	20	20	80	7.1±0.2	1.1±0.1
“J”	6	-0.5	20	20	80	5.9±0.2	2.6±0.1

Table B.6 suggests that the anodic pulse decreases the Mn content of the electrodeposited alloys, but increases the Ti content. The total solute content for the “T” and “J” alloys are 8.2 and 8.5 at.% respectively. Figure B.3 assembles images of the strained surfaces of these Al-Mn-Ti alloys after the guided bent-test. Images on the left column correspond to bend tests where the applied strain was ~37%, while images on the right column correspond to bend tests where the applied strain was ~8%. Images on the top row belong to alloys produced by waveform “T”; while images on the bottom row belong to alloys produced by waveform “J”. Table B.7 summarizes our observations.

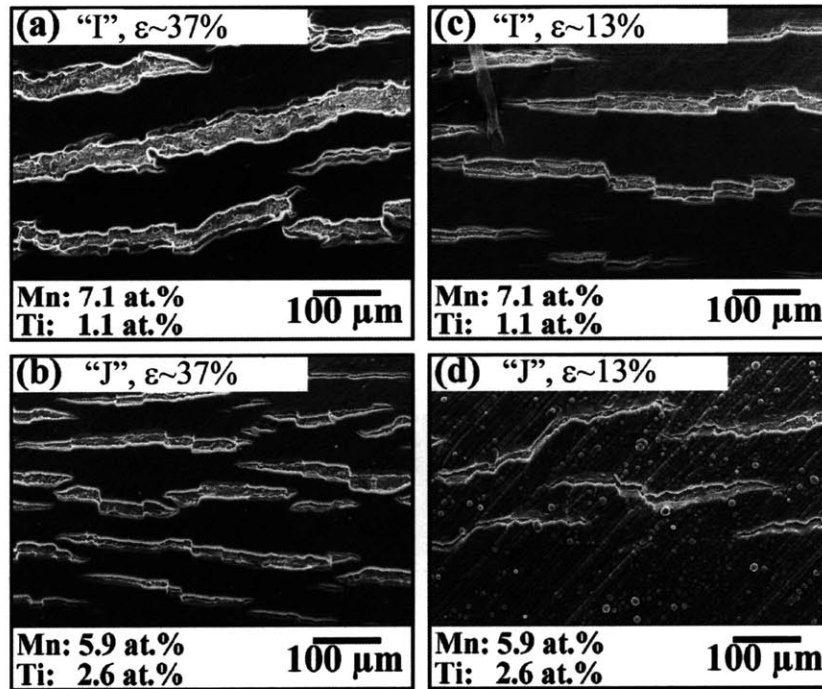


**Figure B.3 SEM images of bent surfaces of Al-Mn-Ti alloys produced by different waveforms. Samples were strained to ~37% in images (a)-(b); and ~8% in images (c)-(d)).**

**Table B.7 Dimensions of cracks observed on strained surfaces of Al-Mn-Ti alloys containing ~8 at.% solute after guided bend test, where applied tensile strains are ~37% and ~8%.**

True strain	Waveform	Crack length ( $\mu\text{m}$ )	Crack width ( $\mu\text{m}$ )
~37%	“T”	300	20
	“J”	150	10
~8%	“T”	200	10
	“J”	200	5

Figure B.3 and Table B.7 show that the application of an anodic pulse improves the ductility of Al-Mn-Ti alloys. The alloy produced by the waveform “T” exhibited cracks that were longer and wider than those found on the alloy produced by waveform “J”. This example illustrates that the application of an anodic pulse can potentially improve the ductility of other Al-based alloys that are electrodeposited at non-ambient temperatures as well.

#### ***B.4. Conclusions***

In this study, waveforms that comprise cathodic, “off-time” and/or anodic pulses are found to improve the ductility of electrodeposited films, as compared to those produced by direct-current waveforms. Of all the waveforms employed, waveforms “D” and “E”, which respectively comprise an “off-time” and anodic pulse, are found to be the most effective at improving film ductility.

Our results indicate that pulse current density and duration dramatically impact film ductility. Clearly, there are many other combinations of pulse parameters that have not been explored in this thesis research. More extensive experiments can be carried out to find a waveform that simultaneously optimizes both hardness and toughness in electrodeposited Al alloys.

## References

- [1] Inoue A. Amorphous, nanoquasicrystalline and nanocrystalline alloys in Al-based systems. *Progress in Materials Science* 1998;43:365.
- [2] Youssef KM, Scattergood RO, Murty KL, Koch CC. Nanocrystalline Al-Mg alloy with ultrahigh strength and good ductility. *Scripta Materialia* 2006;54:251.
- [3] Liddicoat PV, Liao XZ, Ringer SP. Novel Grain Boundary Solute Architecture In a Nanostructured Ultra-High Strength 7075 Aluminium Alloy. *Light Metals Technology* 2009;618-619:543.
- [4] Baucio M, editor *ASM Metals Reference Book*, Third Edition: ASM International, 1993.
- [5] Zhu YT, Langdon TG. The fundamentals of nanostructured materials processed by severe plastic deformation. *JOM* 2004;56:58.
- [6] Ma E. Eight routes to improve the tensile ductility of bulk nanostructured metals and alloys. *Jom* 2006;58:49.
- [7] Schiotz J, Di Tolla FD, Jacobsen KW. Softening of nanocrystalline metals at very small grain sizes. *Nature* 1998;391:561.
- [8] Nieh TG, Wadsworth J. Hall-petch relation in nanocrystalline solids. *Scripta Metallurgica et Materialia* 1991;25:955.
- [9] Detor AJ, Schuh CA. Tailoring and patterning the grain size of nanocrystalline alloys. *Acta Materialia* 2007;55:371.
- [10] Wu BYC, Ferreira PJ, Schuh CA. Nanostructured Ni-Co alloys with tailorable grain size and twin density. *Metallurgical and Materials Transactions a-Physical Metallurgy and Materials Science* 2005;36A:1927.
- [11] Krill CE, Birringer R. Investigations of grain-boundary structure and stability in nanocrystalline Pd. *Metastable, Mechanically Alloyed and Nanocrystalline Materials*, Pts 1 and 2 1996;225:263.
- [12] Krill CE, Ehrhardt H, Birringer R. Thermodynamic stabilization of nanocrystallinity. *Zeitschrift Fur Metallkunde* 2005;96:1134.
- [13] Liu F, Kirchheim R. Grain boundary saturation and grain growth. *Scripta Materialia* 2004;51:521.
- [14] Weissmuller J, Krauss W, Haubold T, Birringer R, Gleiter H. Atomic structure and thermal stability of nanostructured Y-Fe alloys. *Nanostructured Materials* 1992;1:439.
- [15] Liu F, Kirchheim R. Nano-scale grain growth inhibited by reducing grain boundary energy through solute segregation. *Journal of Crystal Growth* 2004;264:385.
- [16] Kirchheim R. Grain coarsening inhibited by solute segregation. *Acta Materialia* 2002;50:413.
- [17] Farber B, Cadel E, Menand A, Schmitz G, Kirchheim R. Phosphorus segregation in nanocrystalline Ni-3.6 at.% P alloy investigated with the tomographic atom probe (TAP). *Acta Materialia* 2000;48:789.
- [18] Hentschel T, Isheim D, Kirchheim R, Muller F, Kreye H. Nanocrystalline Ni-3.6 at.% P and its transformation sequence studied by atom-probe field-ion microscopy. *Acta Materialia* 2000;48:933.
- [19] Detor AJ, Miller MK, Schuh CA. Solute distribution in nanocrystalline Ni-W alloys examined through atom probe tomography. *Philosophical Magazine* 2006;86:4459.
- [20] Detor AJ, Miller MK, Schuh CA. Measuring grain-boundary segregation in nanocrystalline alloys: direct validation of statistical techniques using atom probe tomography. *Philosophical Magazine Letters* 2007;87:581.

- [21] Longworth HP, Thompson CV. Abnormal Grain-Growth in Aluminum-Alloy Thin-Films. *Journal of Applied Physics* 1991;69:3929.
- [22] Beck PA, Kremer JC, Demer LJ, Holzworth ML. Grain growth in high-purity aluminum and in aluminum-magnesium alloy. 1947. p.23.
- [23] Calvet J, Renon C. Discontinuous grain growth in Al-Cu alloys  
Croissance discontinue des cristaux dans les alliages aluminium-cuivre. *Memoires Scientifiques de la Revue de Metallurgie* 1960;57:345.
- [24] Gangulee A, D'Heurle FM. Anomalous large grains in alloyed aluminum thin films I. Secondary grain growth in aluminum-copper films. *Thin Solid Films* 1972;12:399.
- [25] Gangulee A, D'Heurle FM. Anomalous large grains in alloyed aluminum thin films II. Electromigration and diffusion in thin films with very large grains. *Thin Solid Films* 1973;16:227.
- [26] Gholamipour R, Beitollahi A, Marghussian VK, Ohkubo T. Cu effects on coercivity and microstructural features in nanocrystalline Nd-Fe-Co-B annealed melt-spun ribbons. *Physica B: Condensed Matter* 2007;398:51.
- [27] Gholamipour R, Beitollahi A, Ohkubo T, Marghussian VK, Hono K. Microstructural studies and micromagnetic analysis of nanocrystalline NdFeCoMB (M = Ga, Ge) melt-spun ribbon. *Metallurgical and Materials Transactions A (Physical Metallurgy and Materials Science)* 2006;37A:1581.
- [28] Gloriant T, Danoix F, Lefebvre W, Greer AL. Nanocrystallized Al<sub>92</sub>Sm<sub>8</sub> amorphous alloy investigated by high-resolution microscopy and 3D atom-probe analysis. *Advanced Engineering Materials* 2007;9:151.
- [29] Hono K. Nanoscale microstructural analysis of metallic materials by atom probe field ion microscopy. *Progress in Materials Science* 2002;47:621.
- [30] Hono K, Hiraga K, Wang Q, Inoue A, Sakurai T. The microstructure evolution of a Fe<sub>73.5</sub>Si<sub>13.5</sub>B<sub>9</sub>Nb<sub>3</sub>Cu<sub>1</sub> nanocrystalline soft magnetic material. *Acta Metallurgica et Materialia* 1992;40:2137.
- [31] Warren PJ, Thuvander M, Abraham M, Lane H, Cerezo A, Smith GDW. 3-D atom probe studies of some nanostructured materials. *Materials Science Forum* 2000;343:II/.
- [32] Zhang Y, Hono K, Inoue A, Makino A, Sakurai T. Nanocrystalline structural evolution in Fe<sub>90</sub>Zr<sub>7</sub>B<sub>3</sub> soft magnetic material. *Acta Materialia* 1996;44:1497.
- [33] Nagahama D, Ohkubo T, Mukai T, Hono K. Characterization of nanocrystal dispersed Cu<sub>60</sub>Zr<sub>30</sub>Ti<sub>10</sub> metallic glass. *Materials Transactions* 2005;46:1264.
- [34] Ohkubo T, Nagahama D, Mukai T, Hono K. Stress-strain behaviors of Ti-based bulk metallic glass and their nanostructures. *Journal of Materials Research* 2007;22:1406.
- [35] Sasaki TT, Ohkubo T, Hono K. Microstructure and mechanical properties of bulk nanocrystalline Al-Fe alloy processed by mechanical alloying and spark plasma sintering. *Acta Materialia* 2009;57:3529.
- [36] Gleiter H. Nanocrystalline materials. *Progress in Materials Science* 1989;33:223.
- [37] Laslouni W, Taibi K, Dahmoun D, Azzaz M. Structure and properties of nanocrystalline Cu<sub>70</sub>Fe<sub>18</sub>Co<sub>12</sub> obtained by mechanical alloying. *Journal of Non-Crystalline Solids* 2007;353:2090.
- [38] Sunol JJ, Gonzalez A, Bonastre J, Clavaguera-Mora MT, Arcondo B. Synthesis and characterization of nanocrystalline FeNiZrB developed by mechanical alloying. *Journal of Alloys and Compounds* 2007;434:415.
- [39] Hellstern E, Fecht HJ, Fu Z, Johnson WL. Structural and thermodynamic properties of heavily mechanically deformed Ru and AlRu. *Journal of Applied Physics* 1989;65:305.
- [40] Hahn H. Gas phase synthesis of nanocrystalline materials. *Nanostructured Materials* 1997;9:3.



- [41] Stueber M, Holleck H, Leiste H, Seemann K, Ulrich S, Ziebert C. Concepts for the design of advanced nanoscale PVD multilayer protective thin films. *Journal of Alloys and Compounds* 2009;483:321.
- [42] Hahn H, Averback RS. The production of nanocrystalline powders by magnetron sputtering. *Journal of Applied Physics* 1990;67:1113.
- [43] Sriraman KR, Raman SGS, Seshadri SK. Corrosion behaviour of electrodeposited nanocrystalline Ni-W and Ni-Fe-W alloys. *Materials Science and Engineering a-Structural Materials Properties Microstructure and Processing* 2007;460:39.
- [44] Wu BYC, Ferreira PJ, Schuh CA, Nieh TG. Nanostructured Ni-Co alloys with tailorable grain size and twin density. *Metallurgical and Materials Transactions a-Physical Metallurgy and Materials Science* 2005;36A:1927.
- [45] Ebrahimi F, Bourne GR, Kelly MS, Matthews TE. Mechanical properties of nanocrystalline nickel produced by electrodeposition. *Nanostructured Materials* 1999;11:343.
- [46] Ebrahimi F, Kong D, Matthews TE, Zhai Q. Processing of metallic nanostructures by electrodeposition techniques. In: Srivastan TS, Khor KA, editors. *Processing and fabrication of advanced materials VII*. Warrendale (PA) TMS Publication, 1998. p.509.
- [47] Erb U. Electrodeposited nanocrystals: Synthesis, properties and industrial applications. *Nanostructured Materials* 1995;6:533.
- [48] Natter H, Hempelmann R. Tailor-made nanomaterials designed by electrochemical methods. *Electrochimica Acta* 2003;49:51.
- [49] Boylan K, Ostrander D, Erb U, Palumbo G, Aust KT. In-situ tem study of the thermal stability of nanocrystalline Ni-P. *Scripta metallurgica et materialia* 1991;25:2711.
- [50] Natter H, Schmelzer M, Hempelmann R. Nanocrystalline nickel and nickel-copper alloys: synthesis, characterization, and thermal stability. *Journal of Materials Research* 1998;13:1186.
- [51] Robertson A, Erb U, Palumbo G. Practical applications for electrodeposited nanocrystalline materials. *Nanostructured Materials* 1999;12:1035.
- [52] Talin AA, Marquis EA, Goods SH, Kelly JJ, Miller MK. Thermal stability of Ni-Mn electrodeposits. *Acta Materialia* 2006;54:1935.
- [53] Detor AJ, Schuh CA. Microstructural evolution during the heat treatment of nanocrystalline alloys. *Journal of Materials Research* 2007;22:3233.
- [54] El Abedin SZ, Moustafa EM, Hempelmann R, Natter H, Endres F. Additive free electrodeposition of nanocrystalline aluminium in a water and air stable ionic liquid. *Electrochemistry Communications* 2005;7:1111.
- [55] El Abedin SZ, Moustafa EM, Hempelmann R, Natter H, Endres F. Electrodeposition of nano- and microcrystalline aluminium in three different air and water stable ionic liquids. *Chemphyschem* 2006;7:1535.
- [56] Endres F. Ionic fluids for metal deposition. *Nachrichten Aus Der Chemie* 2007;55:507.
- [57] Endres F, Bukowski M, Hempelmann R, Natter H. Electrodeposition of nanocrystalline metals and alloys from ionic liquids. *Angewandte Chemie-International Edition* 2003;42:3428.
- [58] Moustafa EM, El Abedin SZ, Shkurankov A, Zschippang E, Saad AY, Bund A, Endres F. Electrodeposition of Al in 1-butyl-1-methylpyrrolidinium bis(trifluoromethylsulfonyl)amide and 1-ethyl-3-methylimidazolium bis(trifluoromethylsulfonyl)amide ionic liquids: In situ STM and EQCM studies. *Journal of Physical Chemistry B* 2007;111:4693.
- [59] Natter H, Bukowski M, Hempelmann R, El Abedin SZ, Moustafa EM, Endres F. Electrochemical deposition of nanostructured metals and alloys from ionic liquids. *Zeitschrift Fur Physikalische Chemie-International Journal of Research in Physical Chemistry & Chemical Physics* 2006;220:1275.
- [60] Grushko B, Stafford GR. Formation of the Al-Mn Icosahedral Phase by Electrodeposition. *Scripta Metallurgica* 1989;23:1043.

- [61] Grushko B, Stafford GR. Structural Study of Electrodeposited Aluminum-Manganese Alloys. *Metallurgical Transactions a-Physical Metallurgy and Materials Science* 1989;20:1351.
- [62] Grushko B, Stafford GR. A Structural Study of a Metastable Bcc Phase in Al-Mn Alloys Electrodeposited from Molten-Salts. *Scripta Metallurgica* 1989;23:557.
- [63] Pitner WR, Hussey CL, Stafford GR. Electrodeposition of nickel-aluminum alloys from the aluminum chloride-1-methyl-3-ethylimidazolium chloride room temperature molten salt. *Journal of the Electrochemical Society* 1996;143:130.
- [64] Stafford GR. The Electrodeposition of an Aluminum-Manganese Metallic-Glass from Molten-Salts. *Journal of the Electrochemical Society* 1989;136:635.
- [65] Stafford GR. The Electrodeposition of Al<sub>3</sub>Ti from Chloroaluminate Electrolytes. *Journal of the Electrochemical Society* 1994;141:945.
- [66] Egami T, Waseda Y. Atomic size effect on the formability of metallic glasses. *Journal of Non-Crystalline Solids* 1984;64:113.
- [67] Miracle DB, Sanders WS, Senkov ON. The influence of efficient atomic packing on the constitution of metallic glasses. *Philosophical Magazine* 2003;83:2409.
- [68] Shechtman D, Blech I, Gratias D, Cahn JW. Metallic Phase with Long-Range Orientational Order and No Translational Symmetry. *Physical Review Letters* 1984;53:1951.
- [69] Stafford GR, Hussey CL. Electrodeposition of Transition Metal-Aluminum Alloys from Chloroaluminate Molten Salts. In: Alkire RC, Kolb DM, editors. *Advances in Electrochemical Science and Engineering*, Volume 7. 2001. p.275.
- [70] Grushko B, Stafford GR. Effect of Mn Content on the Microstructure of Al-Mn Alloys Electrodeposited at 150C. *Israel Journal of Technology* 1988;24:523.
- [71] Grushko B, Stafford GR. Formation of the Al-Mn icosahedral phase by electrodeposition. *Scripta Metallurgica* 1989;23:1043.
- [72] Grushko B, Stafford GR. A CsCl-type phase in electrodeposited Al---Mn alloys. *Scripta Metallurgica et Materialia* 1994;31:1711.
- [73] Grushko B, Stafford GR. Phase Formation in Electrodeposited and Thermally Annealed Al-Mn Alloys. *Metallurgical Transactions a-Physical Metallurgy and Materials Science* 1990;21:2869.
- [74] Stafford GR, Grushko B, Mcmichael RD. The Electrodeposition of Al-Mn Ferromagnetic Phase from Molten-Salt Electrolyte. *Journal of Alloys and Compounds* 1993;200:107.
- [75] Uchida J, Tsuda T, Yamamoto Y, Seto H, Abe M, Shibuya A. Electroplating of Amorphous Aluminum Manganese Alloy from Molten-Salts. *Isij International* 1993;33:1029.
- [76] Read HJ, Shores DA. Structural Characteristics of Some Electrodeposited Aluminum-Manganese Alloys. *Electrochemical Technology* 1966;4:526.
- [77] Takayama T, Seto H, Uchida J, Hinotani S. Local-Structure and Concentration in Al-Mn Alloy Electrodeposits. *Journal of Applied Electrochemistry* 1994;24:131.
- [78] Li JC, Nan SH, Jiang Q. Study of the electrodeposition of Al-Mn amorphous alloys from molten salts. *Surface and Coatings Technology* 1998;106:135.
- [79] Moffat TP, Stafford GR, Hall DE. Pitting Corrosion of Electrodeposited Aluminum-Manganese Alloys. *Journal of the Electrochemical Society* 1993;140:2779.
- [80] Wagner CNJ, Light TB, Halder NC, Lukens WE. Structure of a Vapor-Quenched AgCu Alloy. *Journal of Applied Physics* 1968;39:3690.
- [81] Bendersky LA, Ridder SD. Nucleation behavior of Al-Mn icosahedral phase. *Journal of Materials Research* 1986;1:405.
- [82] Chen LC, Spaepen F. Calorimetric Evidence for the Microquasicrystalline Structure of Amorphous Al-Transition Metal-Alloys. *Nature* 1988;336:366.
- [83] Chen LC, Spaepen F. Analysis of Calorimetric Measurements of Grain-Growth. *Journal of Applied Physics* 1991;69:679.

- [84] Chen LC, Spaepen F, Robertson JL, Moss SC, Hiraga K. A Structural and Calorimetric Study of the Transformations in Sputtered Al-Mn and Al-Mn-Si Films. *Journal of Materials Research* 1990;5:1871.
- [85] Ruan S, Schuh CA. Kinetic Monte Carlo simulations of nanocrystalline film deposition. *Journal of Applied Physics*;107:073512.
- [86] Casella IG. Pulsed electrodeposition of palladium thin-film from alkaline solutions containing Pd(II)-cyanide complexes: An electrochemical and XPS investigation. *Journal of the Electrochemical Society* 2008;155:D723.
- [87] Fujiwara T, Igasaki Y. The effects of pulsing the current in galvanostatic electrodeposition technique on the composition and surface morphology of In-Se films. *Journal of Crystal Growth* 1997;178:321.
- [88] Giro F, Bedner K, Dhum C, Hoffmann JE, Heussler SP, Jian L, Kirsch U, Moser HO, Saumer M. Pulsed electrodeposition of high aspect-ratio NiFe assemblies and its influence on spatial alloy composition. *Microsystem Technologies-Micro-and Nanosystems-Information Storage and Processing Systems* 2008;14:1111.
- [89] Kalaniary MR, Gabe DR, Goodenough MR. Unipolar and bipolar pulsed current electrodeposition for PCB production. *Journal of Applied Electrochemistry* 1993;23:231.
- [90] Kim DJ, Roh YM, Seo MH, Kim JS. Effects of the peak current density and duty cycle on material properties of pulse-plated Ni-P-Fe electrodeposits. *Surface and Coatings Technology* 2005;192:88.
- [91] Lee J, Farhangfar S, Lee J, Cagnon L, Scholz R, Gosele U, Nielsch K. Tuning the crystallinity of thermoelectric Bi<sub>2</sub>Te<sub>3</sub> nanowire arrays grown by pulsed electrodeposition. *Nanotechnology* 2008;19.
- [92] Lucatero S, Fowle WH, Podlaha EJ. Electrodeposited Au/FeAu Nanowires with Controlled Porosity. *Electrochemical and Solid State Letters* 2009;12:D96.
- [93] Mishra AC, Thakur AK, Srinivas V. Effect of deposition parameters on microstructure of electrodeposited nickel thin films. *Journal of Materials Science* 2009;44:3520.
- [94] Nakanishi T, Ozaki M, Nam HS, Yokoshima T, Osaka T. Pulsed electrodeposition of nanocrystalline CoNiFe soft magnetic thin films. *Journal of the Electrochemical Society* 2001;148:C627.
- [95] Natter H, Schmelzer M, Hempelmann R. Nanocrystalline nickel and nickel-copper alloys: Synthesis, characterization, and thermal stability. *Journal of Materials Research* 1998;13:1186.
- [96] Nikolova L, Ignatova K, Stefanova S. Effect of pulsating electrolysis parameters on the morphology and structure of Pd-Ag powder. *Journal of Applied Electrochemistry* 1996;26:1059.
- [97] Saravanan G, Mohan S. Pulsed electrodeposition of microcrystalline chromium from trivalent Cr-DMF bath. *Journal of Applied Electrochemistry* 2009;39:1393.
- [98] Wong KP, Chan KC, Yue TM. A study of surface finishing in pulse current electroforming of nickel by utilizing different shaped waveforms. *Surface and Coatings Technology* 1999;115:132.
- [99] Ruan S, Schuh CA. Mesoscale structure and segregation in electrodeposited nanocrystalline alloys. *Scripta Materialia* 2008;59:1218.
- [100] Fei JY, Wilcox GD. Electrodeposition of Zn-Co alloys with pulse containing reverse current. *Electrochimica Acta* 2005;50:2693.
- [101] Zhu Q, Hussey CL. Galvanostatic pulse plating of Cu-Al alloy in a room-temperature chloroaluminate molten salt - Rotating ring-disk electrode studies. *Journal of the Electrochemical Society* 2001;148:C395.
- [102] Fei J-Y, Wilcox GD. Electrodeposition of Zn-Co alloys with pulse containing reverse current. *Electrochimica Acta* 2005;50:2693.
- [103] Ruan SY, Schuh CA. Electrodeposited Al-Mn alloys with microcrystalline, nanocrystalline, amorphous and nano-quasicrystalline structures. *Acta Materialia* 2009;57:3810.

- [104] Mamantov G, Popov AI. Chemistry of Nonaqueous Solutions :Current Progress: VCH, 1994.
- [105] Zhang Z, Zhou F, Lavernia EJ. On the analysis of grain size in bulk nanocrystalline materials via X-ray diffraction. Metallurgical and Materials Transactions a-Physical Metallurgy and Materials Science 2003;34A:1349.
- [106] Oliver WC, Pharr GM. An Improved Technique for Determining Hardness and Elastic-Modulus Using Load and Displacement Sensing Indentation Experiments. Journal of Materials Research 1992;7:1564.
- [107] Thompson CV. Structure evolution during processing of polycrystalline films. Annual Review of Materials Science 2000;30:159.
- [108] Bastos A, Zaefferer S, Raabe D, Schuh C. Characterization of the microstructure and texture of nanostructured electrodeposited NiCo using electron backscatter diffraction (EBSD). Acta Materialia 2006;54:2451.
- [109] Schaefer RJ, Bendersky LA, Shechtman D, Boettinger WJ, Biancaniello FS. Icosahedral and Decagonal Phase Formation in Al-Mn Alloys. Metallurgical Transactions a-Physical Metallurgy and Materials Science 1986;17:2117.
- [110] Powder Diffraction File. The International Centre for Diffraction Data, 2006.
- [111] Bancel PA, Heiney PA, Stephens PW, Goldman AI, Horn PM. Structure of rapidly quenched Al-Mn. Physical Review Letters 1985;54:2422.
- [112] Kontio A, Coppens P. New Study of the Structure of MnAl<sub>6</sub>. Acta Crystallographica Section B-Structural Science 1981;37:433.
- [113] McAlister AJ, Murray JL. Al-Mn (Aluminum-Manganese). In: Massalski TB, editor. Binary Alloy Phase Diagrams, II Ed. , vol. 1. 1990. p.171.
- [114] Greer AL. Crystallization Kinetics of Fe<sub>80</sub>B<sub>20</sub> Glass. Acta Metallurgica 1982;30:171.
- [115] Battezzati L, Garrone E. On the Approximation of the Free-Energy of Undercooled Glass-Forming Metallic Melts. Zeitschrift Fur Metallkunde 1984;75:305.
- [116] Weissmuller J. Alloy Thermodynamics in Nanostructures. Journal of Materials Research 1994;9:4.
- [117] Koch CC, White CL, Padgett RA, Liu CT. Boron segregation at grain boundaries in rapidly solidified Ni<sub>3</sub>Al. Scripta Metallurgica 1985;19:963.
- [118] Hayashi T. International Symposium on Molten Salt Chemistry and Technology. The Electrochemical Society of Japan, 1983. p.53.
- [119] Glasstone S. Electrode potentials and the form of electrodeposited metals. Transactions of the Faraday Society 1935;31:1232.
- [120] Bockris J, Razumny G. Fundamental aspects of electrocrystallization. Plenum Press, NY, 1967. p.27.
- [121] Moti E, Shariat MH, Bahrololoom ME. Influence of cathodic overpotential on grain size in nanocrystalline nickel deposition on rotating cylinder electrodes. Journal of Applied Electrochemistry 2008;38:605.
- [122] Liu CL, Cohen JM, Adams JB, Voter AF. EAM study of surface self-diffusion of single adatoms of fcc metals Ni, Cu, Al, Ag, Au, Pd, and Pt. Surface Science 1991;253:334.
- [123] Inoue A, Ohtera K, Kita K, Masumoto T. New Amorphous-Alloys with Good Ductility in Al-Ce-Nb, Al-Ce-Fe, Al-Ce-Co, Al-Ce-Ni, Al-Ce-Cu Systems. Japanese Journal of Applied Physics Part 2-Letters 1988;27:L1796.
- [124] Inoue A, Bizen Y, Kimura HM, Masumoto T, Sakamoto M. Compositional range, thermal stability, hardness and electrical resistivity of amorphous alloys in Al-Si (or Ge)-transition metal systems. Journal of Materials Science 1988;23:3640.
- [125] Zhong ZC, Jiang XY, Greer AL. Nanocrystallization in Al-based amorphous alloys. Philosophical Magazine B-Physics of Condensed Matter Statistical Mechanics Electronic Optical and Magnetic Properties 1997;76:505.

- [126] Kim YH, Inoue A, Masumoto T. Ultrahigh Tensile Strengths of Al<sub>88</sub>Y<sub>2</sub>Ni<sub>9</sub>Mn<sub>1</sub> or Al<sub>88</sub>Y<sub>2</sub>Ni<sub>9</sub>Fe<sub>1</sub> Amorphous-Alloys Containing Finely Dispersed Fcc-Al Particles. *Materials Transactions Jim* 1990;31:747.
- [127] Gloriant T. Microhardness and abrasive wear resistance of metallic glasses and nanostructured composite materials. *Journal of Non-Crystalline Solids* 2003;316:96.
- [128] Lund AC, Schuh CA. Critical length scales for the deformation of amorphous metals containing nanocrystals. *Philosophical Magazine Letters* 2007;87:603.
- [129] Ruan S, Schuh CA. Electrodeposited alloys and methods of making same using power pulses. U.S. Patent Application No. 12/579,062, filed Oct 14, 2009.
- [130] Chin GY, Hosford WF, Backofen WA. Ductile Fracture of Aluminum. *Transactions of the Metallurgical Society of Aime* 1964;230:437.
- [131] French I, Weinrich P. The effects of hydrostatic pressure on the mechanism of tensile fracture of aluminum. *Metallurgical and Materials Transactions A* 1975;6:1165.
- [132] Takasugi T, Watanabe S, Hanada S. The Temperature and Orientation Dependence of Tensile Deformation and Fracture in Nial Single-Crystals. *Materials Science and Engineering a-Structural Materials Properties Microstructure and Processing* 1992;149:183.
- [133] Weinrich PF, French IE. The influence of hydrostatic pressure on the fracture mechanisms of sheet tensile specimens of copper and brass. *Acta Metallurgica* 1976;24:317.
- [134] Adeva P, Caruana G, Ruano OA, Torralba M. Microstructure and high temperature mechanical properties of tin. *Materials Science and Engineering A* 1995;194:17.
- [135] Allen NP, Hopkins BE, McLennan JE. The Tensile Properties of Single Crystals of High-Purity Iron at Temperatures from 100 to -253-Degrees-C. *Proceedings of the Royal Society of London Series a-Mathematical and Physical Sciences* 1956;234:221.
- [136] French IE, Weinrich PF. The influence of hydrostatic pressure on the tensile deformation and fracture of copper. *Metallurgical Transactions A (Physical Metallurgy and Materials Science)* 1975;6:785.
- [137] Kim S-K, Bang J-G, Kim D-H, Lim I-S, Yang Y-S, Song K-W, Kim D-S. Hoop strength and ductility evaluation of irradiated fuel cladding. *Nuclear Engineering and Design* 2009;239:254.
- [138] Yao JH, Wang JQ, Li Y. Ductile Fe--Nb--B bulk metallic glass with ultrahigh strength. *Applied Physics Letters* 2008;92:251906.
- [139] Xi XK, Zhao DQ, Pan MX, Wang WH, Wu Y, Lewandowski JJ. Fracture of Brittle Metallic Glasses: Brittleness or Plasticity. *Physical Review Letters* 2005;94:125510.
- [140] Inoue A. Stabilization of metallic supercooled liquid and bulk amorphous alloys. *Acta Materialia* 2000;48:279.
- [141] Sergueeva AV, Mara NA, Kuntz JD, Lavernia EJ, Mukherjee AK. Shear band formation and ductility in bulk metallic glass. *Philosophical Magazine* 2005;85:2671.
- [142] Sergueeva AV, Mara NA, Branagan DJ, Mukherjee AK. Strain rate effect on metallic glass ductility. *Scripta Materialia* 2004;50:1303.
- [143] Van Swygenhoven H, Derlet PM. Grain-boundary sliding in nanocrystalline fcc metals. *Physical Review B* 2001;64:224105.
- [144] Shan Z, Stach EA, Wiezorek JMK, Knapp JA, Follstaedt DM, Mao SX. Grain Boundary-Mediated Plasticity in Nanocrystalline Nickel. *Science* 2004;305:654.
- [145] Wang YB, Ho JC, Liao XZ, Li HQ, Ringer SP, Zhu YT. Mechanism of grain growth during severe plastic deformation of a nanocrystalline Ni--Fe alloy. *Applied Physics Letters* 2009;94:011908.
- [146] Legros M, Gianola DS, Hemker KJ. In situ TEM observations of fast grain-boundary motion in stressed nanocrystalline aluminum films. *Acta Materialia* 2008;56:3380.
- [147] Choi P, Da Silva M, Klement U, Al-Kassab T, Kirchheim R. Thermal stability of electrodeposited nanocrystalline Co-1.1at.%P. *Acta Materialia* 2005;53:4473.

- [148] Abe E, Kawamura Y, Hayashi K, Inoue A. Long-period ordered structure in a high-strength nanocrystalline Mg-1 at% Zn-2 at% Y alloy studied by atomic-resolution Z-contrast STEM. *Acta Materialia* 2002;50:3845.
- [149] Detor AJ, Schuh CA. Grain boundary segregation, chemical ordering and stability of nanocrystalline alloys: Atomistic computer simulations in the Ni-W system. *Acta Materialia* 2007;55:4221.
- [150] Chen Y, Zhang T, Zhang W, Ping D, Hono K, Inoue A, Sakurai T. Microstructure feature of bulk glassy Cu<sub>60</sub>Zr<sub>30</sub>Ti<sub>10</sub> alloy in as-cast and annealed states. *Materials Transactions* 2002;43:2647.
- [151] Chen YM, Ohkubo T, Ohta M, Yoshizawa Y, Hono K. Three-dimensional atom probe study of Fe-B-based nanocrystalline soft magnetic materials. *Acta Materialia* 2009;57:4463.
- [152] Hono K, Ping DH. Atom probe studies of nanocrystallization of amorphous alloys. *Materials Characterization* 2000;44:203.
- [153] Hono K, Ping DH, Ohnuma M, Onodera H. Cu clustering and Si partitioning in the early crystallization stage of an Fe<sub>73.5</sub>Si<sub>13.5</sub>B<sub>9</sub>Nb<sub>3</sub>Cu<sub>1</sub> amorphous alloy. *Acta Materialia* 1999;47:997.
- [154] Martin I, Ohkubo T, Ohnuma M, Deconihout B, Hono K. Nanocrystallization of Zr<sub>41.2</sub>Ti<sub>13.8</sub>Cu<sub>12.5</sub>Ni<sub>10.0</sub>Be<sub>22.5</sub> metallic glass. *Acta Materialia* 2004;52:4427.
- [155] Miller MK, Shen TD, Schwarz RB. Atom probe tomography study of the decomposition of a bulk metallic glass. *Intermetallics* 2002;10:1047.
- [156] Murty BS, Ping DH, Hono K, Inoue A. Direct evidence for oxygen stabilization of icosahedral phase during crystallization of Zr<sub>65</sub>Cu<sub>27.5</sub>Al<sub>7.5</sub> metallic glass. *Applied Physics Letters* 2000;76:55.
- [157] Ohnuma M, Hono K, Onodera H, Pedersen JS, Linderroth S. Cu clustering stage before the crystallization in Fe---Si---B---Nb---Cu amorphous alloys. *Nanostructured Materials* 1999;12:693.
- [158] Ohodnicki Jr PR, Qin YL, Laughlin DE, McHenry ME, Kodzuka M, Ohkubo T, Hono K, Willard MA. Composition and non-equilibrium crystallization in partially devitrified co-rich soft magnetic nanocomposite alloys. *Acta Materialia* 2009;57:87.
- [159] Ping DH, Hono K, Inoue A. Oxygen distribution in Zr<sub>65</sub>Cu<sub>15</sub>Al<sub>10</sub>Pd<sub>10</sub> nanocrystalline alloys. *Materials Science Forum* 1999;307:31.
- [160] Radiguet B, Blavette D, Wanderka N, Banhart J, Sahoo KL. Segregation-controlled nanocrystallization in an Al-Ni-La metallic glass. *Applied Physics Letters* 2008;92.
- [161] You CY, Ohkubo T, Takahashi YK, Hono K. Boron segregation in crystallized MgO/amorphous- Co<sub>40</sub> Fe<sub>40</sub> B<sub>20</sub> thin films. *Journal of Applied Physics* 2008;104.
- [162] Zhang Y, Czubayko U, Wanderka N, Zhu F, Wollenberger H. Effect of gold addition on the nanostructure of amorphous Fe-Zr-B alloy. *Journal of Materials Research* 2000;15:1271.
- [163] Zhang Y, Hono K, Inoue A, Sakurai T. APFIM studies of nanocrystalline microstructural evolution in Fe-Zr-B(-Cu) amorphous alloys. *Materials Science and Engineering A* 1996;A217-21:407.
- [164] Zhang Y, Wanderka N, Czubayko U, Zhu F, Wollenberger H. Nucleation behavior of -Fe in amorphous Fe-7Zr-5B-1Au alloy. *Materials Science Forum* 2000;343:I/.
- [165] Zhang Y, Warren PJ, Cerezo A. Effect of Cu addition on nanocrystallisation of Al-Ni-Sm amorphous alloy. *Materials Science and Engineering A* 2002;327:109.
- [166] Miller M, Cerezo, A. and Hetherington, MG. *Atom Probe Field Ion Microscopy*: Clarendon Press , Oxford, 1996.
- [167] Miller M. *Atom Probe Tomography: Analysis at the Atomic Level* Kluwer Academic/Plenum Press , New York, 2000.
- [168] Miller MK, Burke MG. Atom probe field-ion microscopy: 30 years of atomic-level analysis. *Materials Characterization* 2000;44:1.

- [169] Gopalan R, Xiong XY, Ohkubo T, Hono K. Nanoscale microstructure and magnetic properties of melt-spun Sm(Co 0.725Fe0.1Cu0.12Zr0.04B 0.015)7.4 ribbons. *Journal of Magnetism and Magnetic Materials* 2005;295:7.
- [170] Wu YQ, Tang W, Miller MK, Anderson IE, McCallum RW, Dennis KW, Kramer MJ. Microanalytical characterization of multi-rare-earth nanocrystalline magnets by transmission electron microscopy and atom probe tomography. *Journal of Applied Physics* 2006;99.
- [171] Ohsaki S, Hono K, Hidaka H, Takaki S. Characterization of nanocrystalline ferrite produced by mechanical milling of pearlitic steel. *Scripta Materialia* 2005;52:271.
- [172] Hentschel T, Isheim D, Kirchheim R, Müller F, Kreye H. Nanocrystalline Ni-3.6 at.% P and its transformation sequence studied by atom-probe field-ion microscopy. *Acta Materialia* 2000;48:933.
- [173] Hirata A, Hirotsu Y, Matsubara E, Ohkubo T, Hono K. Mechanism of nanocrystalline microstructure formation in amorphous Fe-Nb-B alloys. *Physical Review B (Condensed Matter and Materials Physics)* 2006;74:184204.
- [174] Hono K. Overview No. 133: Atom probe microanalysis and nanoscale microstructures in metallic materials. *Acta Materialia* 1999;47:3127.
- [175] Chen MW, Sakai A, Inoue A, Wang XM, Watanabe Y, Sakurai T. Partitioning behavior of Al in a nanocrystalline FeZrBAl soft magnetic alloy. *Journal of Applied Physics* 2000;87:439.
- [176] Chen MW, Sakai A, Wang XM, Inoue A, Sakurai T. Distribution of Nb and Co in an -Fe/Nd2Fe14B-type nanocomposite. *Journal of Applied Physics* 2000;88:6928.
- [177] Hono K, Zhang Y, Tsai AP, Inoue A, Sakurai T. Solute partitioning in partially crystallized Al-Ni-Ce(-Cu) metallic glasses. *Scripta metallurgica et materialia* 1995;32:191.
- [178] Kimoto Y, Giga A, Ohkubo T, Takigawa Y, Hono K, Higashi K. Ni-W amorphous/nanocrystalline duplex composite produced by electrodeposition. *Materials Transactions* 2007;48:996.
- [179] Lefebvre W, Morin-Grognet S, Danoix F. Role of Niobium in the nanocrystallization of a Fe73.5Si13.5B9Nb3Cu alloy. *Journal of Magnetism and Magnetic Materials* 2006;301:343.
- [180] Murty BS, Ping DH, Hono K, Kimura H, Inoue A. Microstructure of Rapidly Solidified High Strength Al94V 4Fe2 Alloy. *Materials Transactions* 2003;44:1993.
- [181] Ping DH, Hono K, Inoue A. Microstructural characterization of a rapidly solidified ultrahigh strength Al94.5Cr3Co1.5Ce1 alloy. *Metallurgical and Materials Transactions A (Physical Metallurgy and Materials Science)* 2000;31A:607.
- [182] Ping DH, Hono K, Kawamura Y, Inoue A. Local chemistry of a nanocrystalline high-strength Mg97Y2Zn1 alloy. *Philosophical Magazine Letters* 2002;82:543.
- [183] Wu YQ, Ping DH, Hono K, Hamano M, Inoue A. Microstructural characterization of an -Fe/Nd2Fe14B nanocomposite magnet with a remaining amorphous phase. *Journal of Applied Physics* 2000;87:8658.
- [184] Thompson K, Lawrence D, Larson DJ, Olson JD, Kelly TF, Gorman B. In situ site-specific specimen preparation for atom probe tomography. *Ultramicroscopy* 2007;107:131.
- [185] Miller MK, Smith GD, Cerezo A, Hetherington MG, Cerezo A. *Atom Probe Field Ion Microscopy* Oxford University Press, 1996.
- [186] Cowan G. *Statistical Data Analysis*: Oxford University Press, 1998.
- [187] Ludwig W, Pereiro-Lopez E, Bellet D. In situ investigation of liquid Ga penetration in Al bicrystal grain boundaries: grain boundary wetting or liquid metal embrittlement? *Acta Materialia* 2005;53:151.
- [188] Pereiro-López E, Ludwig W, Bellet D. Discontinuous penetration of liquid Ga into grain boundaries of Al polycrystals. *Acta Materialia* 2004;52:321.
- [189] Hugo RC, Hoagland RG. In-Situ TEM Observation of Aluminum Embrittlement by Liquid Gallium. *Scripta Materialia* 1998;38:523.
- [190] Hugo RC, Hoagland RG. Gallium penetration of aluminum: in-situ TEM observations at the penetration front. *Scripta Materialia* 1999;41:1341.

- [191] Thomson DI, Heine V, Payne MC, Marzari N, Finnis MW. Insight into gallium behavior in aluminum grain boundaries from calculation on  $[\Sigma]=11$  (113) boundary. *Acta Materialia* 2000;48:3623.
- [192] Butler JE, Sumant AV. The CVD of nanodiamond materials. *Chemical Vapor Deposition* 2008;14:145.
- [193] Gurrappa I, Binder L. Electrodeposition of nanostructured coatings and their characterization—a review. *Science and Technology of Advanced Materials* 2008;9:043001.
- [194] Tjong SC, Chen H. Nanocrystalline materials and coatings. *Materials Science and Engineering: R: Reports* 2004;45:1.
- [195] Xiao F, Hangarter C, Yoo B, Rheem Y, Lee K-H, Myung NV. Recent progress in electrodeposition of thermoelectric thin films and nanostructures. *Electrochimica Acta* 2008;53:8103.
- [196] Paritosh, Srolovitz DJ, Battaile CC, Li X, Butler JE. Simulation of faceted film growth in two-dimensions: Microstructure, morphology and texture. *Acta Materialia* 1999;47:2269.
- [197] Smereka P, Li XQ, Russo G, Srolovitz DJ. Simulation of faceted film growth in three dimensions: microstructure, morphology and texture. *Acta Materialia* 2005;53:1191.
- [198] Perovic DD, Weatherly GC, Noel JP, Houghton DC. Electron-Microscopy Study of Microvoid Generation in Molecular-Beam Epitaxy-Grown Silicon. *Journal of Vacuum Science & Technology B* 1991;9:2034.
- [199] Perovic DD, Weatherly GC, Simpson PJ, Schultz PJ, Jackman TE, Aers GC, Noel JP, Houghton DC. Microvoid Formation in Low-Temperature Molecular-Beam-Epitaxy-Grown Silicon. *Physical Review B* 1991;43:14257.
- [200] Mohammadreza Baghbanan UEGP. Towards the application of nanocrystalline metals in MEMS. *physica status solidi (a)* 2006;203:1259.
- [201] Dong L, Srolovitz DJ. Texture development mechanisms in ion beam assisted deposition. *Journal of Applied Physics* 1998;84:5261.
- [202] Smith RW, Srolovitz DJ. Void formation during film growth: A molecular dynamics simulation study. *Journal of Applied Physics* 1996;79:1448.
- [203] Smith RW, Ying F, Srolovitz DJ. Growth and Texture of Polycrystalline Thin Films. *Materials Research Society Symposium Proceedings*, vol. 403: Materials Research Society, 1996. p.39.
- [204] Battaile CC, Srolovitz DJ. Kinetic Monte Carlo simulation of chemical vapor deposition. *Annual Review of Materials Science* 2002;32:297.
- [205] Kotrla M, Smilauer P. Nonuniversality in models of epitaxial growth. *Physical Review B* 1996;53:13777.
- [206] Yan H. Kinetic Growth with Surface-Diffusion - the Scaling Aspect. *Physical Review Letters* 1992;68:3048.
- [207] Dassarma S, Lanczycki CJ, Ghaisas SV, Kim JM. Defect Formation and Crossover-Behavior in the Dynamic Scaling Properties of Molecular-Beam Epitaxy. *Physical Review B* 1994;49:10693.
- [208] Schimschak M, Krug J. Bulk Defects and Surface Roughening in Epitaxial-Growth. *Physical Review B* 1995;52:8550.
- [209] Lanczycki CJ, Jejjala V, DasSarma S. Far from equilibrium nonconserved growth under a surface diffusion bias. *Physical Review E* 1996;54:4755.
- [210] Krug J, Plischke M, Siegert M. Surface-Diffusion Currents and the Universality Classes of Growth. *Physical Review Letters* 1993;70:3271.
- [211] Siegert M, Plischke M. Solid-on-Solid Models of Molecular-Beam Epitaxy. *Physical Review E* 1994;50:917.
- [212] Krug J. Origins of scale invariance in growth processes. *Advances in Physics* 1997;46:139.



- [213] Zhang P, Zheng X, Wu S, He D. A computer simulation of nucleation and growth of thin films. *Computational Materials Science* 2004;30:331.
- [214] Gilmer GH, Huang H, de la Rubia TD, Dalla Torre J, Baumann F. Lattice Monte Carlo models of thin film deposition. *Thin Solid Films* 2000;365:189.
- [215] Bruschi P, Nannini A, Pieri F. Monte Carlo simulation of polycrystalline thin film deposition. *Physical Review B* 2001;63.
- [216] Huang H, Zhou LG. Atomistic simulator of polycrystalline thin film deposition in three dimensions. *Journal of Computer-Aided Materials Design* 2004;11:59.
- [217] Rubio JE, Jaraiz M, Martin-Bragado I, Hernandez-Mangas JM, Barbolla J, Gilmer GH. Atomistic Monte Carlo simulations of three-dimensional polycrystalline thin films. *Journal of Applied Physics* 2003;94:163.
- [218] Huang H, Gilmer GH. Texture competition during thin film deposition - effects of grain boundary migration. *Computational Materials Science* 2002;23:190.
- [219] Srolovitz DJ. Grain-Growth Phenomena in Films - a Monte-Carlo Approach. *Journal of Vacuum Science & Technology a-Vacuum Surfaces and Films* 1986;4:2925.
- [220] Srolovitz DJ, Mazor A, Bukiet BG. Analytical and Numerical Modeling of Columnar Evolution in Thin-Films. *Journal of Vacuum Science & Technology a-Vacuum Surfaces and Films* 1988;6:2371.
- [221] Smith RW. A kinetic Monte Carlo simulation of fiber texture formation during thin-film deposition. *Journal of Applied Physics* 1997;81:1196.
- [222] Huang HC, Gilmer GH, de la Rubia TD. An atomistic simulator for thin film deposition in three dimensions. *Journal of Applied Physics* 1998;84:3636.
- [223] Levine SW, Clancy P. A simple model for the growth of polycrystalline Si using the kinetic Monte Carlo simulation. *Modelling and Simulation in Materials Science and Engineering* 2000;8:751.
- [224] Wang L, Clancy P. Kinetic Monte Carlo simulation of the growth of polycrystalline Cu films. *Surface Science* 2001;473:25.
- [225] Sobchenko IV, Gusak AM, Tu KN. 3D Monte-Carlo model of deposition and grain growth in thin films. *Diffusion and Defect Data. Pt A Defect and Diffusion Forum* 2005;237-240:1281.
- [226] Tan X, Zhou YC, Zheng XJ. Pulsed-laser deposition of polycrystalline Ni films: A three-dimensional kinetic Monte Carlo simulation. *Surface Science* 2005;588:175.
- [227] Huang YY, Zhou YC, Pan Y. Simulation of kinetically limited growth of electrodeposited polycrystalline Ni films. *Physica E: Low-dimensional Systems and Nanostructures* 2009;41:1673.
- [228] Wang W, Cerdeira HA. Kinetic Growth of Random-Like and Ballistic-Like Deposition Models. *Physical Review E* 1993;47:3357.
- [229] Kang HC, Weinberg WH. Dynamic Monte Carlo with a proper energy barrier: Surface diffusion and two-dimensional domain ordering. *The Journal of Chemical Physics* 1989;90:2824.
- [230] Voter AF. Classically exact overlayer dynamics: Diffusion of rhodium clusters on Rh(100). *Physical Review B* 1986;34:6819.
- [231] Evans DM, Wilman H. Crystal growth and orientation in deposits condensed from the vapour. *Acta Crystallographica* 1952;5:731.
- [232] Murbach HP, Wilman H. The Origin of Stress in Metal Layers Condensed from the Vapour in High Vacuum. *Proceedings of the Physical Society. Section B* 1953;66:905.
- [233] Rossmagel SM, Robinson RS, Kaufman HR. Impact enhanced surface diffusion during impurity induced sputter cone formation. *Surface Science* 1982;123:89.
- [234] Dennis JK, Such TE. Nickel and chromium plating. Materials Park (OH): ASM International, 1993.
- [235] Menéndez JL, Caro P, Cebollada A. Epitaxy, strain and morphology of low Ar pressure sputtered Pt thin films. *Journal of Crystal Growth* 1998;192:164.

- [236] Willmott PR. Deposition of complex multielemental thin films. *Progress in Surface Science* 2004;76:163.
- [237] Chowdhury A, Mukhopadhyay S, Ray S. Structural and transport properties of nanocrystalline silicon thin films prepared at 54.24 MHz plasma excitation frequency. *Journal of Crystal Growth* 2007;304:352.
- [238] Bai P, McDonald JF, Lu TM. Cu Deposition on Rough Ceramic Substrate - Physical Structure, Microstructure, and Resistivity. *Journal of Materials Research* 1991;6:289.
- [239] Grovenor CRM, Hentzell HTG, Smith DA. The development of grain structure during growth of metallic films. *Acta Metallurgica* 1984;32:773.
- [240] Yoshikawa N, Kikuchi A. Grain growth and texture of chemical-vapour-deposited refractory metal and ceramics. *Grain Growth in Polycrystalline Materials II*, Pts 1 and 2 1996;204-:509.
- [241] Savaloni H, Player MA. Influence of deposition conditions and of substrate on the structure of uhv deposited erbium films. *Vacuum* 1995;46:167.
- [242] Lin TJ, O'Keefe TJ, James WJ. Structure and properties of metallic Sn--Zn alloy films prepared by plasma-enhanced metalorganic chemical vapor deposition. *Thin Solid Films* 1989;177:271.
- [243] El Khakani MA, Le Drogoff B, Chaker M. Effect of the deposition temperature on the properties of iridium thin films grown by means of pulsed laser deposition. *Journal of Materials Research* 1999;14:3241.
- [244] Mitra R, Hoffman RA, Madan A, Weertman JR. Effect of process variables on the structure, residual stress, and hardness of sputtered nanocrystalline nickel films. *Journal of Materials Research* 2001;16:1010.
- [245] Lee SH, So MG. Effects of deposition temperature and pressure of the surface roughness and the grain size of polycrystalline Si<sub>1-x</sub>Gex films. *Journal of Materials Science* 2000;35:4789.
- [246] Quartarone E, Mustarelli P, Grandi S, Marabelli F, Bontempi E. Effects of the deposition parameters on the growth of ultrathin and thin SiO<sub>2</sub> films. *Journal of Vacuum Science & Technology A: Vacuum, Surfaces, and Films* 2007;25:485.
- [247] Park JK, Kim JH, Park SI, Lee HM, Oh DY. Evolution of grain structure of as-deposited Cr thin films with deposition temperature. *Scripta Materialia* 2003;48:1161.
- [248] Jalili H, Heinig NF, Leung KT. Formation of nanocrystalline films of Sr<sub>2</sub>FeMoO<sub>6</sub> on Si(100) by pulsed laser deposition: Observation of preferential oriented growth. *Journal of Applied Physics* 2009;105:034305.
- [249] Albu-Yaron A, Frank A, Hodes G, Noufi R. Cross-sectional transmission electron microscopy of thin film polycrystalline semiconductors by conventional microtomy. *Thin Solid Films* 1993;227:18.
- [250] Merchant HD, Liu WC, Giannuzzi LA, Morris JG. Grain structure of thin electrodeposited and rolled copper foils. *Materials Characterization* 2004;53:335.